EF-hand protein Ca^{2+} buffers regulate Ca^{2+} influx and exocytosis in sensory hair cells

Tina Pangršič[a,b,1,2,3], Mantas Gabrielaitis[a,c,d,2], Susann Michanski[a,b], Beat Schwaller[e], Fred Wolf[b,c,d], Nicola Strenzke[b,f,g,3], and Tobias Moser[a,b,d,3]

[a]Institute for Auditory Neuroscience and InnerEarLab, University Medical Center Göttingen, 37099 Göttingen, Germany; [b]Collaborative Research Center 889, University of Göttingen, 37099 Göttingen, Germany; [c]Theoretical Neurophysics Group, Max Planck Institute for Dynamics and Self-Organization, 37077 Göttingen, Germany; [d]Bernstein Center for Computational Neuroscience, Göttingen University, 37077 Göttingen, Germany; [e]Unit of Anatomy, Department of Medicine, University of Fribourg, 1700 Fribourg, Switzerland; [f]Auditory Systems Physiology Group, InnerEarLab, Department of Otolaryngology, University Medical Center Göttingen, 37099 Göttingen, Germany; and [g]Eaton Peabody Laboratory, Massachusetts Eye and Ear Infirmary, Harvard University, Boston, MA 02114

EF-hand Ca^{2+}-binding proteins are thought to shape the spatiotemporal properties of cellular Ca^{2+} signaling and are prominently expressed in sensory hair cells in the ear. Here, we combined genetic disruption of parvalbumin-α, calbindin-D28k, and calretinin in mice with patch-clamp recording, in vivo physiology, and mathematical modeling to study their role in Ca^{2+} signaling, exocytosis, and sound encoding at the synapses of inner hair cells (IHCs). IHCs lacking all three proteins showed excessive exocytosis during prolonged depolarizations, despite enhanced Ca^{2+}-dependent inactivation of their Ca^{2+} current. Exocytosis of readily releasable vesicles remained unchanged, in accordance with the estimated tight spatial coupling of Ca^{2+} channels and release sites (effective "coupling distance" of 17 nm). Substitution experiments with synthetic Ca^{2+} chelators indicated the presence of endogenous Ca^{2+} buffers equivalent to 1 mM synthetic Ca^{2+}-binding sites, approximately half of them with kinetics as fast as 1,2-Bis(2-aminophenoxy)ethane-N,N,N′,N′-tetraacetic acid (BAPTA). Synaptic sound encoding was largely unaltered, suggesting that excess exocytosis occurs extrasynaptically. We conclude that EF-hand Ca^{2+} buffers regulate presynaptic IHC function for metabolically efficient sound coding.

calcium buffers | exocytosis | calcium current | synapse | hair cell

Intracellular Ca^{2+} signaling regulates a multitude of cellular processes. In sensory hair cells, Ca^{2+} is crucial for electrical frequency tuning, afferent synaptic transmission, and efferent modulation (reviewed in ref. 1). To separate these signaling pathways and maintain high temporal fidelity of neurotransmission, Ca^{2+} signals must be temporally limited and spatially confined to the site of action. Cells typically achieve this by localizing Ca^{2+} entry and by rapidly removing free Ca^{2+} ions via binding to cytosolic "buffers" and finally Ca^{2+} extrusion (2–4). Of the various EF-hand Ca^{2+}-binding proteins, some seem to function primarily as Ca^{2+}-dependent signaling proteins (e.g., calmodulin and Ca^{2+}-binding proteins 1–8, CaBP1–8), whereas others [parvalbumin-α (PVα), calbindin-D28k (CB), and calretinin (CR)] are thought to mainly serve as mobile Ca^{2+} buffers.

Hair cells of various species strongly express the Ca^{2+}-binding proteins PV, CB, and, in some cases, CR. This possibly reflects the need for buffers with different biophysical properties to functionally isolate different Ca^{2+} signaling mechanisms, which are spatially not well separated in these compact epithelial cells. Ca^{2+}-binding proteins are particularly abundant in frog and chicken hair cells, which contain millimolar concentrations of parvalbumin-3 (5) as well as of CR (6, 7). An immune-EM study in rats indicated hundreds of micromolar of proteinaceous Ca^{2+}-binding sites in inner hair cells (IHCs) (8). A patch-clamp study in gerbil IHCs reported endogenous buffers equivalent to approximately 0.4 mM 1,2-Bis(2-aminophenoxy)ethane-N,N,N′,N′-tetraacetic acid (BAPTA) (9). Genetic deletion of the EF-hand Ca^{2+}-binding proteins PVα, CB, and CR in mice has facilitated the analysis of their function (10–13; reviewed in ref. 14), but the combined deletion of these proteins remains to be studied. IHCs provide an experimentally well-accessible presynaptic preparation that uses all three. Here, we studied IHC function and hearing in mice lacking the three buffers [triple buffer KO (TKO); $Pv^{-/-}Cb^{-/-}Cr^{-/-}$]. By using perforated and ruptured-patch recordings, we analyzed voltage-gated Ca^{2+} currents and exocytosis of $Pv^{-/-}Cb^{-/-}Cr^{-/-}$ IHCs, in which we also substituted the deleted endogenous buffers with the synthetic Ca^{2+} chelators EGTA or BAPTA. Auditory systems function was probed by measuring otoacoustic emissions and auditory brainstem responses (ABRs) as well as by recordings from single spiral ganglion neurons (SGNs). We performed mathematical modeling to estimate concentrations of the endogenous mobile Ca^{2+} buffers and to better understand how these proteins control exocytosis at IHC synapses. We conclude that the endogenous buffer capacity of IHCs is well approximated by 1 mM synthetic Ca^{2+}-binding sites with different kinetics. A tight spatial coupling between Ca^{2+} channels and sensors of exocytosis (Ca^{2+} channel-exocytosis coupling) precludes interference of PVα, CB, and CR with fusion of the readily releasable pool of vesicles (RRP). Instead, we suggest that these buffers jointly regulate IHC presynaptic function by restricting neurotransmitter release to active zones (AZs).

Significance

Ca^{2+} ions serve as a key cellular signal and are tightly controlled. One mechanism to limit free Ca^{2+} ions is buffering by Ca^{2+}-binding proteins, which are strongly expressed in sensory hair cells of the ear. Here we studied how genetic disruption of the Ca^{2+}-binding proteins parvalbumin-α, calbindin-D28k, and calretinin affects exocytosis and sound encoding at the synapses of mouse inner hair cells (IHCs) and spiral ganglion neurons (SGNs). Mutant IHCs showed increased exocytosis, but the sound-evoked spiking activity in SGNs was unaltered. Together with mathematical modeling, this finding indicates that a large fraction of exocytosis in mutant IHCs occurred outside synapses. We conclude that Ca^{2+}-binding proteins shape presynaptic Ca^{2+} signals to restrict exocytosis to active zones, thus enabling metabolically efficient sound encoding.

Results

IHCs of Hearing Mice Express PVα, CB, and CR. Hair cells in various species show specific expression patterns of the EF-hand Ca^{2+}-binding proteins PVα, parvalbumin-β (PVβ) (oncomodulin), CB, and CR (5, 7, 8, 15), hereafter termed "mobile Ca^{2+} buffers" so as not to ignore the presence of other Ca^{2+} buffers such as ATP. We performed immunohistochemistry on apical organs of Corti of hearing C57BL/6 mice [postnatal day (P) 14–26] to characterize the expression of mobile Ca^{2+} buffers in mouse cochlear hair cells (Fig. 1). In agreement with results obtained in rats (8), we found mature mouse IHCs to express PVα, CB, and CR (Fig. 1 *A–C*), but not PVβ, which was strongly expressed in outer hair cells (OHCs) (Fig. 1*D*). Parallel immunostaining of organs of Corti from age-matched $Pv^{-/-}Cb^{-/-}Cr^{-/-}$ mice confirmed the absence of these three mobile Ca^{2+} buffers from all tissues (Fig. 1 *E–G*) but the persistent expression of PVβ in OHCs (Fig. 1*H*).

Disruption of PVα, CB, and CR Increases the Amplitude and Inactivation of Ca^{2+} Current and Enhances Exocytosis in IHCs. Next, we studied the presynaptic function of $Pv^{-/-}Cb^{-/-}Cr^{-/-}$ IHCs by patch-clamp recordings of Ca^{2+} currents and exocytosis. We first examined the amplitude, voltage dependence, activation, and inactivation of the IHC Ca^{2+} current that is largely mediated by $Ca_V1.3$ channels (16–18). We used perforated-patch recordings to not interfere with the endogenous Ca^{2+} buffering. We found a 20% increase of the initial Ca^{2+} current, whereas its voltage-dependence was unchanged (Fig. 2*A*). Ca^{2+}-current kinetics were analyzed at the potential eliciting the peak Ca^{2+} current (on average at −17 mV). The activation time constants were comparable between $Pv^{-/-}Cb^{-/-}Cr^{-/-}$ and WT ($Pv^{+/+}Cb^{+/+}Cr^{+/+}$) IHCs (Fig. 2*B*). However, we observed a significant increase of Ca^{2+}-current inactivation (nonnormalized currents; Fig. 2*C*). Inactivation was first assessed by analyzing the ratio of the current amplitude at the end of a 100-ms-long depolarization and the initial current amplitude. This ratio was smaller in $Pv^{-/-}Cb^{-/-}Cr^{-/-}$ than in $Pv^{+/+}Cb^{+/+}Cr^{+/+}$ IHCs (mean ± SEM, 0.71 ± 0.02 vs. 0.79 ± 0.01; $P =$
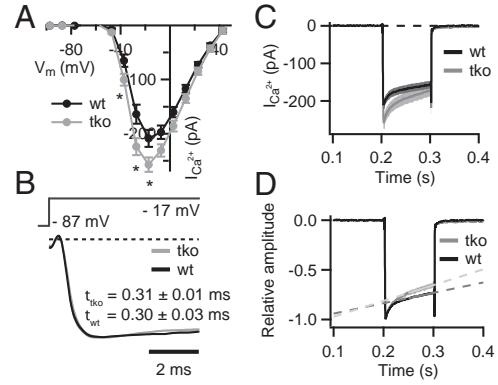
Fig. 2. Disruption of PVα, CB, and CR enhances Ca^{2+}-current amplitude and inactivation. (*A*) Current–voltage relationship of the voltage-gated Ca^{2+} current in TKO (gray, $n = 20$) and WT (black, $n = 23$) IHCs from 2–3-wk-old mice. Note the slightly larger Ca^{2+} currents in the TKO IHCs (*$P = 0.01$–0.03, Student t test). (*B*) Normalized average Ca^{2+} currents in response to 10–100-ms depolarizations to the peak Ca^{2+}-current potential on an expanded time scale demonstrate that the kinetics of the activation were not different among TKO and WT IHCs ($P = 0.13$, Wilcoxon rank-sum test). Data were fitted with $I(t) = I_0 + I_{max} \times (1 - e^{-t/\tau})^p$, whereby the power (*p*) was fixed to 2 in most cases. (*C* and *D*) Absolute (*C*) and normalized (*D*) Ca^{2+} currents in response to 100-ms depolarizations to the peak Ca^{2+} current potential. A stronger Ca^{2+}-current inactivation was observed in the TKO IHCs. Slopes of the linear fits (1/s) are 1.0 ± 0.1 and 1.6 ± 0.2 for the Ca^{2+} currents in WT ($n = 16$) and TKO ($n = 14$) IHCs, respectively ($P = 0.02$, Student t test).
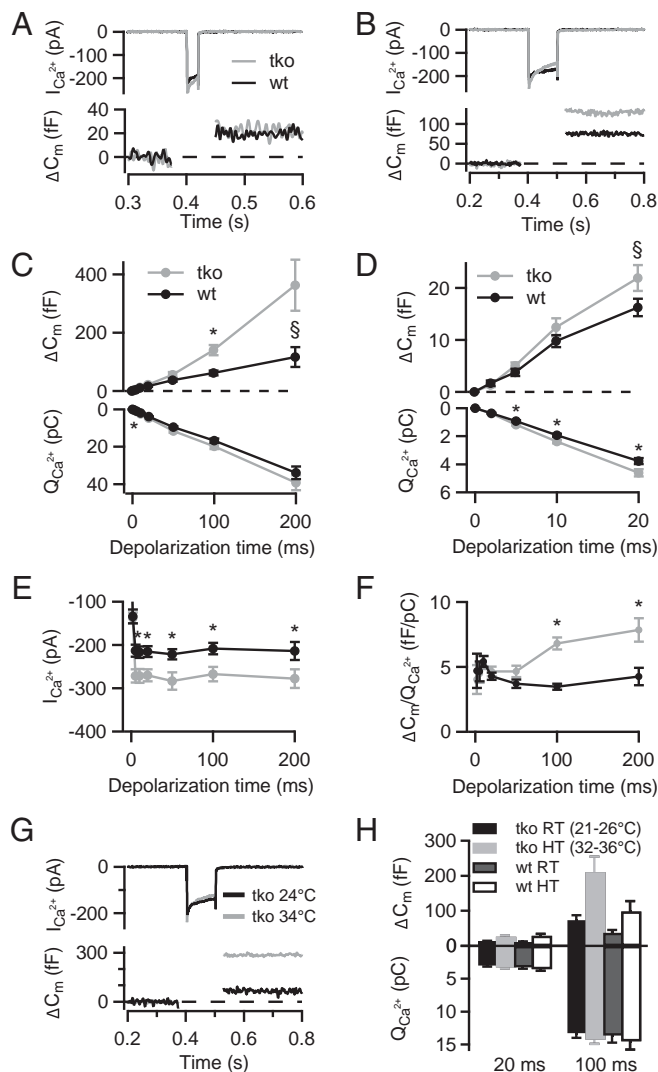
0.01, Wilcoxon rank-sum test). As a second measure of the Ca^{2+}-current inactivation, we fitted a linear function to the last 50 ms of the normalized Ca^{2+} currents. Its steeper slope for $Pv^{-/-}Cb^{-/-}Cr^{-/-}$ IHCs corroborated the notion of a more pronounced inactivation (Fig. 2*D*).

To address potential mechanisms underlying the increased Ca^{2+}-current amplitude, we evaluated the number and morphological appearance of the ribbon synapses in IHCs after hearing onset (P15–P18). The presynaptic ribbon protein Ribeye/CtBP2 and the postsynaptic glutamate receptor GluA 2/3 were visualized by confocal microscopy of immunolabeled organs of Corti (19). We found comparable numbers of ribbons (12.5 ± 0.9 and 13.9 ± 0.5; *SI Appendix*, Fig. S1), glutamate receptor clusters (12.5 ± 0.8 and 13.4 ± 1.1), as well as ribbon synapses (12.0 ± 0.9 and 12.6 ± 0.9 in six WT and five TKO organs of Corti, respectively). This argues against a potential up-regulation of synapse number as a cause for the increased Ca^{2+} current. It also rules out an excitotoxic degradation of synapses that one might have expected from potentially enhanced glutamate release in the absence of the three Ca^{2+} buffers.

We then studied depolarization-induced exocytosis by using membrane capacitance (C_m) measurements, first in perforated-patch experiments and second in ruptured-patch recordings from $Pv^{-/-}Cb^{-/-}Cr^{-/-}$ IHCs with varying concentrations of BAPTA or EGTA in the pipette solution. To probe for potential effects of Ca^{2+}-buffer deficiency on exocytosis, cells were depolarized for different durations and C_m was measured before and after depolarization (Fig. 3). Interestingly, exocytosis upon short stimuli was not significantly altered (Fig. 3 *C* and *D*), a finding that can, according to our mathematical model, best be explained by tight Ca^{2+} channel–exocytosis coupling (as detailed later). However, we found more exocytosis in the $Pv^{-/-}Cb^{-/-}Cr^{-/-}$ IHCs for longer stimuli ($P < 0.05$ for $\Delta C_{m,100ms}$; Fig. 3*C*; figure legends provide *P* values of other ΔC_m measurements) despite comparable Ca^{2+}-charge transfer. The ΔC_m amplitude was more variable for 200-ms depolarizations, but the higher efficiency of Ca^{2+} influx to drive sustained exocytosis in $Pv^{-/-}Cb^{-/-}Cr^{-/-}$ IHCs can readily be appreciated from the ratio of exocytic increments over
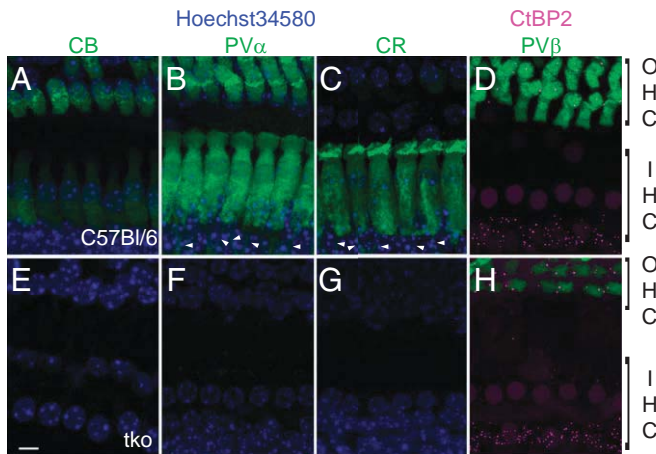
Fig. 1. IHCs of hearing mice express the EF-hand Ca^{2+}-binding proteins PVα, CB, and CR. (*A–H*) Maximum projections of confocal stacks from whole-mount explants of the apical coils of P14–P26 organs of Corti of WT (*Top*) and $Pv^{-/-}Cb^{-/-}Cr^{-/-}$ (TKO; *Bottom*) mice immunolabeled for calbindin-D28k (CB; *A* and *E*), parvalbumin-α (PVα; *B* and *F*), calretinin (CR; *C* and *G*), and parvalbumin-β (PVβ; *D* and *H*, all in green). An antibody against CtBP2 was used as a marker of presynaptic ribbons and cell nuclei (magenta, *D* and *H*). In all other panels, cell nuclei were stained with Hoechst 34580 (blue). IHC bodies of WT but not TKO organs of Corti are homogeneously stained for three Ca^{2+} buffers, CB, PVα, and CR. OHCs additionally contain PVβ, not present in IHCs and not targeted for deletion in the TKO mice. PVα and CR show immuno-reactivity also in the afferent fibers (arrowheads). (Scale bar: 5 μm.)
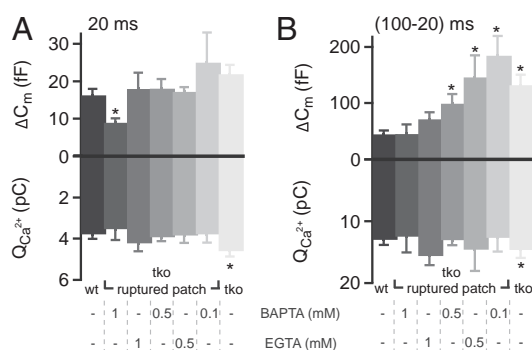
significantly larger in $Pv^{-/-}Cb^{-/-}Cr^{-/-}$ IHCs as a result of stronger Ca^{2+}-current inactivation (Fig. 3C, Lower). Sustained exocytosis tended to be enhanced for $Pv^{-/-}Cb^{-/-}Cr^{-/-}$ IHCs also in near physiological conditions (>32 °C, 2 mM extracellular $[Ca^{2+}]$), indicating that this likely also occurs in vivo (Fig. 3 G and H). We conclude that the mobile Ca^{2+} buffers PVα, CB, and CR contribute to the regulation of presynaptic Ca^{2+} influx and exocytosis.

To approximate the concentration and binding kinetics of the mobile Ca^{2+} buffers of IHCs, we studied the effects of substituting endogenous Ca^{2+} buffers by BAPTA ("fast binding": association rate constant $k_{on} = 4 \times 10^8$ $M^{-1} \cdot s^{-1}$; see ref. 20) or EGTA ("slow binding": $k_{on} = 4.5 \times 10^6$ or 10^7 $M^{-1} \cdot s^{-1}$; see refs. 20, 21) on RRP exocytosis (probed by 20-ms depolarizations) (22) and sustained exocytosis (approximated by the difference between the responses to 100- and 20-ms depolarizations). Synthetic buffers were loaded into $Pv^{-/-}Cb^{-/-}Cr^{-/-}$ IHCs to restore the exocytic responses of $Pv^{+/+}Cb^{+/+}Cr^{+/+}$ IHCs in their native buffering conditions (Fig. 4). We found that 1 mM EGTA or BAPTA reduced sustained exocytosis in $Pv^{-/-}Cb^{-/-}Cr^{-/-}$ IHCs to levels comparable to $Pv^{+/+}Cb^{+/+}Cr^{+/+}$ IHCs recorded in perforated-patch recordings (Fig. 4B). BAPTA (1 mM) best matched to the exocytic responses of $Pv^{+/+}Cb^{+/+}Cr^{+/+}$ IHC for prolonged depolarizations, but significantly diminished RRP exocytosis (Fig. 4A). Lower concentrations of fast or slow Ca^{2+} buffer, on the contrary, left RRP exocytosis unchanged, but could not reinstate the sustained exocytic response as seen in $Pv^{+/+}Cb^{+/+}Cr^{+/+}$ IHCs. From these experiments, we conclude that the endogenous concentration of mobile buffers in IHCs is equivalent to ~1 mM synthetic Ca^{2+}-binding sites, half of them with kinetics as fast as BAPTA. Of note, none of the tested concentrations of EGTA or BAPTA was able to accurately restore the exocytic responses as observed in $Pv^{+/+}Cb^{+/+}Cr^{+/+}$ IHCs.

The Absence of PVα, CB, and CR Has Little Impact on Hearing. We first tested cochlear amplification by measuring distortion product otoacoustic emissions (DPOAEs), which were found to be intact in $Pv^{-/-}Cb^{-/-}Cr^{-/-}$ mice (Fig. 5 A and B). We then investigated the synchronized neuronal signaling along the auditory pathway by measuring ABRs (Fig. 5 C and D). Over the time course of the project, we encountered variable ABR phenotypes of $Pv^{-/-}Cb^{-/-}$

Fig. 3. Enhanced sustained exocytosis in the absence of PVα, CB, and CR. (A and B) Representative Ca^{2+} currents (Top) and C_m (ΔC_m) responses (Bottom) of TKO (gray) and WT (black) IHCs to (A) 20-ms and (B) 100-ms depolarization to peak Ca^{2+}-current potential, recorded in the perforated-patch configuration. (C) Exocytosis (ΔC_m; Top) and the corresponding Ca^{2+}-current integrals (Q_{Ca}; Bottom) as a function of duration of depolarizations to peak Ca^{2+}-current potential. The C_m increase in response to 100-ms depolarization ($\Delta C_{m,100ms}$) was significantly higher in TKO (gray, n = 24) compared with WT IHCs [black, n = 23; *P = 0.0003, Wilcoxon rank-sum test; §P = 0.06, Wilcoxon rank-sum test (C) and Student t test (D)]. Note larger Q_{Ca} in TKO IHCs at short but not long depolarization (*P = 0.009 for 5 ms and P = 0.02 for 10- and 20-ms depolarization, Student t test). All responses are given as grand averages (calculated from the means of the individual cells) ± SEM. (D) ΔC_m (Top) and Q_{Ca} (Bottom) in response to short depolarizations evoking the exocytosis of the RRP displayed on an expanded time scale. (E) Ca^{2+}-current amplitudes (I_{Ca}) were significantly increased in the TKO IHCs (*P < 0.0004, Student t test). (F) The Ca^{2+} efficiency of exocytosis was higher in the TKO IHCs for long depolarizations (*P = 1.5 × 10^{-10} for 100 ms and P = 0.007 for 200 ms depolarization, Wilcoxon rank-sum test). The extracellular $[Ca^{2+}]$ was 5 mM. (G) Representative Ca^{2+} currents (Top) and ΔC_m (Bottom) of a TKO IHCs recorded at room (black) or close to physiological temperature (gray) with 2 mM extracellular $[Ca^{2+}]$. (H) Average ΔC_m and Q_{Ca} in response to 20- and 100-ms depolarizations recorded at room temperature (RT; black and dark gray) and high temperature (HT; close to physiological temperature, light gray and white) in WT (n = 4) and TKO (n = 5) IHCs. Note a two- to threefold increase in ΔC_m responses upon increase in temperature in the IHCs of both genotypes.

Ca^{2+}-current integrals (Fig. 3F). Despite increased initial Ca^{2+} current, the Ca^{2+} charge transfer for long depolarizations was not

Fig. 4. Functional estimation of the concentration and kinetics of endogenous Ca^{2+}-binding sites in IHCs. (A) ΔC_m and Q_{Ca} in response to depolarization for 20 ms (probing the RRP) in WT and TKO IHCs using perforated-patch (black and light gray) and in KO IHCs using ruptured-patch configuration with different concentrations of the exogenously added synthetic Ca^{2+} chelators BAPTA and EGTA (shades of gray). (B) Difference in the ΔC_m and Q_{Ca} in response to 100 and 20 ms (probing the sustained exocytosis). When testing the sustained component of exocytosis 0.5 mM of either buffer was insufficient in Ca^{2+} buffering. On the contrary, 1 mM BAPTA (but not EGTA) significantly reduced the amount of RRP exocytosis (A). Asterisks denote significant difference vs. WT controls (P < 0.01, Student t test or Wilcoxon rank-sum test). From left to right, n = 18, n = 6, n = 5, n = 12, n = 10, n = 7, and n = 12 IHCs were analyzed.
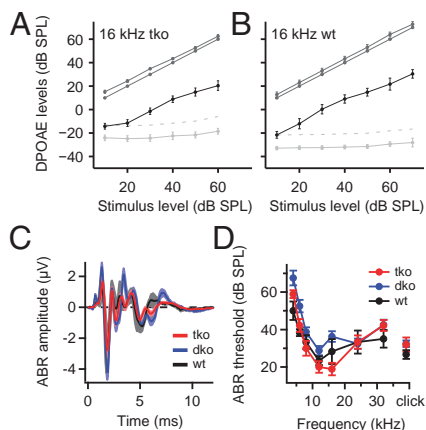
Fig. 5. Cochlear function is preserved in mice lacking the three most prominent EF-hand Ca^{2+} buffers. (*A* and *B*) Input/output functions of otoacoustic emissions (i.e., DPOAEs; black lines) of the TKO (*A*) and WT (*B*) mice at 16 kHz f_2 tone. Solid light gray lines indicate the noise floor; dotted light gray lines indicate 2 SDs above the noise floor. The dark gray lines represent both primary tones. All data represent grand averages over several animals. No significant difference was observed between the WT and TKO mice. (*C*) Average ABR in response to 80 dB clicks in WT (black), $Pv^{-/-}Cb^{-/-}$ (DKO; blue), and TKO (red) mice. (*D*) Analysis of ABR thresholds revealed no significant difference among the three genotypes. All data are given as mean ± SEM.

enlarged around the synapses in the Ca^{2+}-buffer KOs (28), we performed semiquantitative immunohistochemistry in isolated organs of Corti of $Pv^{-/-}Cb^{-/-}$ and C57BL/6 mice. Apical coils of the organs of Corti were stained for the mitochondria by using the marker PNPase (29) and ribbons (CtBP2; Fig. 7 *A* and *B*). Samples of both genotypes were processed identically and in parallel during immunohistochemistry and confocal imaging (Fig. 7*C*). Cumulative PNPase immunofluorescence was analyzed in a total of 1,440 C57BL/6 and 1,260 $Pv^{-/-}Cb^{-/-}$ synapses from four different experiments on cochleae of eight C57BL/6 and $Pv^{-/-}Cb^{-/-}$ mice. In none of the experiments did we observe a significantly increased presynaptic PNPase immunofluorescence in IHCs of $Pv^{-/-}Cb^{-/-}$ mice, indicating a normal mitochondrial abundance despite the absence of PVα and CB. Similarly, we did not detect an up-regulation of the plasma membrane Ca^{2+}-pumps (PMCAs; *SI Appendix*, Fig. S4).
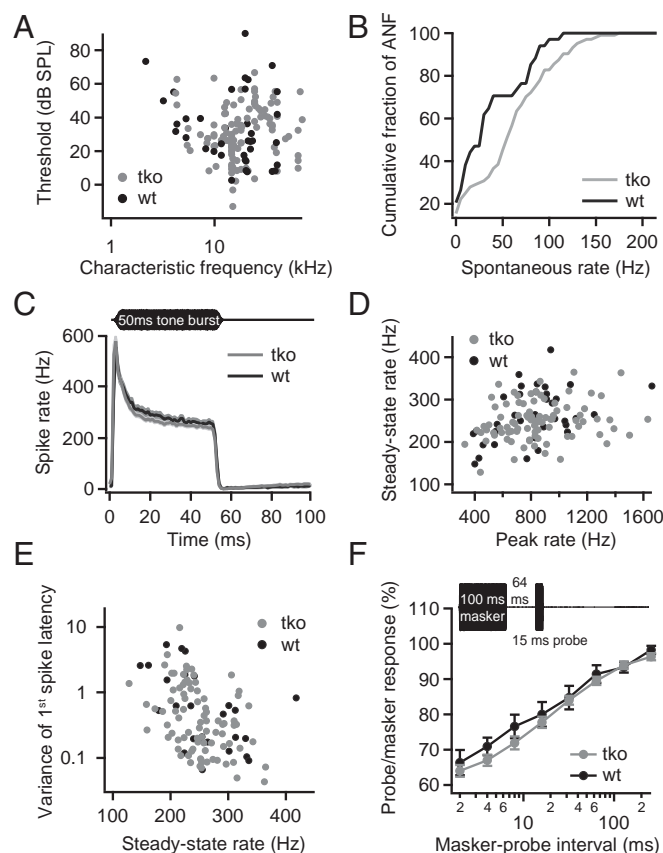
$Cr^{-/-}$ mice. In the majority of animals, there was no noticeable increase in the ABR thresholds for tone bursts at different frequencies or clicks in comparison with age-matched $Pv^{+/+}Cb^{+/+}Cr^{+/+}$ mice (Fig. 5*D*). We additionally tested hearing in mice deficient only in PVα and CB ($Pv^{-/-}Cb^{-/-}$). They did not show a significant hearing deficit as assessed by ABR (Fig. 5 *C* and *D*), which is consistent with the majority of our $Pv^{-/-}Cb^{-/-}Cr^{-/-}$ data.

Next, we studied sound encoding at the single SGN level. Consistent with their near normal population responses (Fig. 5), the single fiber thresholds were comparable between $Pv^{-/-}Cb^{-/-}Cr^{-/-}$ and $Pv^{+/+}Cb^{+/+}Cr^{+/+}$ SGNs (Fig. 6*A*). The rate of spontaneous SGN firing was increased in $Pv^{-/-}Cb^{-/-}Cr^{-/-}$ mice ($P = 0.04$, Kolmogorov–Smirnov test; Fig. 6*B*), which likely reflects enhanced transmitter release from buffer-deficient IHCs in the absence of sound.

We then stimulated each SGN with 50-ms tone bursts at 30 dB above threshold at the characteristic frequency (CF) to study sound-driven spike rates at saturating sound pressure levels (Fig. 6*C*). Like in previously published data (23–25), all SGNs showed a high onset firing rate followed by adaptation to reach a lower, but still sizable, steady-state rate. We found no significant differences in the peak rates in SGNs of $Pv^{-/-}Cb^{-/-}Cr^{-/-}$ mice (Fig. 6*D*). Steady-state spike rates were comparable (*SI Appendix*, Fig. S2B) or even slightly lower in $Pv^{-/-}Cb^{-/-}Cr^{-/-}$ mice (Fig. 6 *C* and *D*), in apparent contrast to the enhanced sustained exocytosis in IHCs (Fig. 3), an unexpected observation that we investigated in more detail by mathematical modeling (as detailed later). $Pv^{-/-}Cb^{-/-}Cr^{-/-}$ SGNs also showed very good temporal precision of sound-onset coding (Fig. 6*E*). Forward masking experiments (26, 27) revealed a normal extent of depletion of the RRP and unaltered replenishment kinetics (Fig. 6*F*). In summary, the single SGN data agree with the notion of a largely unimpaired peripheral auditory function, including a normal temporal precision of sound encoding for transient and sustained stimuli (*SI Appendix*, Fig. S3).

No Obvious Up-Regulation of Perisynaptic Mitochondria or Plasma Membrane Ca^{2+} Pumps in IHCs Lacking PVα and CB. The weak effects of Ca^{2+}-buffer deficiency on synaptic sound coding prompted us to test for a potential compensation by enhanced perisynaptic mitochondrial Ca^{2+} uptake (11, 28). To test whether mitochondria are present in increased number or are perhaps

Fig. 6. Disruption of PVα, CB, and CR has little impact on sound encoding by single SGNs. (*A*) Thresholds measured at the CF of each auditory nerve fiber. The thresholds of the TKO fibers (gray, $n = 111$) were comparable to WT controls (black, $n = 37$). (*B*) Spontaneous rate distributions in TKO mice (gray, $n = 104$) and control groups (black, $n = 34$). Higher spontaneous rates were observed in SGNs of the TKO animals. (*C*) Mean peristimulus time histograms (±SEM) plotting the instantaneous spiking rate in 1-ms time bins over the time course of stimulation with tone bursts at the CF of each SGN, 30 dB above threshold. The rates and the time course of adaptation were similar in TKO (gray, $n = 87$) and WT SGNs (black, $n = 35$). (*D*) The analysis of the peak rates (rate in largest 1-ms bin) vs. the steady-state spike rates (averaged over 10 ms from 35 ms after stimulus onset) shows comparable rates between TKO SGNs (gray) and WT controls (black). (*E*) The variance of the first spike latency was similar between fibers from TKO mice and WT controls. (*F*) Recovery from adaptation probed by a forward-masking paradigm (*Inset*): maximal masking and the time course of recovery were similar for TKO (gray, $n = 35$) and WT controls (black, $n = 8$). Stimuli were applied at CF, 30 dB above threshold.
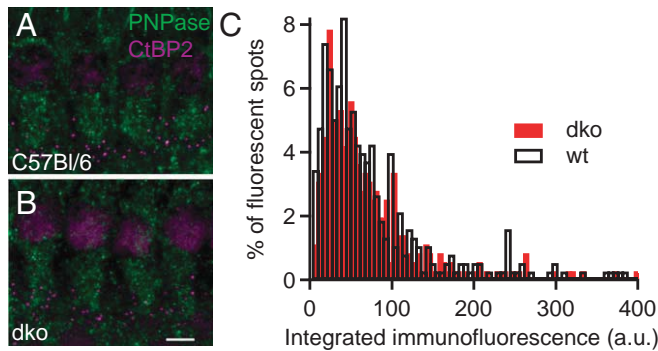
Fig. 7. Immunofluorescence analysis of perisynaptic abundance of mitochondria. (*A* and *B*) The whole mount of the C57BL/6 (WT) and DKO organs of Corti double stained for the mitochondrial marker PNPase (green) and the presynaptic marker CtBP2 (magenta) reveals similar abundance of mitochondria in IHCs of both genotypes. (Scale bar: 5 μm.) (*C*) Perisynaptic PNPase immunofluorescence intensity (integrated within a 0.5-μm radius around the center of mass of CtBP2 fluorescence in single confocal sections) in WT and DKO IHCs. A total of 377 synapses from four C57BL/6 (WT) organs and 357 synapses from four DKO organs were analyzed, and the distributions were statistically indistinguishable (*P* = 0.94, Wilcoxon rank-sum test).

Computational Analysis of IHC Exocytosis and SGN Spiking Indicates Enhanced Extrasynaptic Release in *Pv⁻/⁻Cb⁻/⁻Cr⁻/⁻* IHCs. SGN activity is governed by transmitter release at the IHC ribbon synapse. To understand how increased IHC exocytosis of the *Pv⁻/⁻Cb⁻/⁻Cr⁻/⁻* animals influences SGN spiking rate, we used mathematical modeling (24) (Fig. 8*A* and *Materials and Methods*). Specifically, we addressed the question whether the excess sustained exocytosis reflects an acceleration of synaptic vesicle replenishment by Ca^{2+} (30, 31) or extrasynaptic release caused by the wider spread of the synaptic Ca^{2+} signal. The model converts release events in IHCs into SGN spiking by taking into account neuronal refractoriness (32, 33). Refractory periods in WT and TKO SGNs were similar (1.11 ± 0.04 ms and 1.02 ± 0.03 ms, respectively; *SI Appendix*, Fig. S5*C*). By using these parameters and assuming that all sustained IHC exocytosis occurs synaptically, i.e., drives spiking in the postsynaptic SGNs, the spike rates predicted for *Pv⁻/⁻Cb⁻/⁻Cr⁻/⁻* SGNs substantially exceeded the experimentally observed ones (Fig. 8*B*). The discrepancy persisted even when assuming unrealistically long refractory periods (*SI Appendix*, Fig. S5*D*). This indicates that a large fraction of the increased sustained exocytosis in the *Pv⁻/⁻Cb⁻/⁻Cr⁻/⁻* IHCs occurs at extrasynaptic (i.e., ectopic) locations, and is ineffective in driving SGNs. Indeed, membrane-proximal vesicles outside the AZ are observed in hair cells (34, 35) (Fig. 8*C*). We then estimated what fraction of the excess sustained exocytosis in *Pv⁻/⁻Cb⁻/⁻Cr⁻/⁻* IHCs could be synaptic (Fig. 8*D*). Only when this fraction was set at less than 10% did the difference between the computed and experimentally observed spike rates fall within the uncertainty range of the experimental data. Therefore, we conclude that only a minor part of the excess sustained exocytosis, if any, reflects enhanced vesicle replenishment caused by stronger Ca^{2+} signaling in the absence of mobile Ca^{2+} buffers.
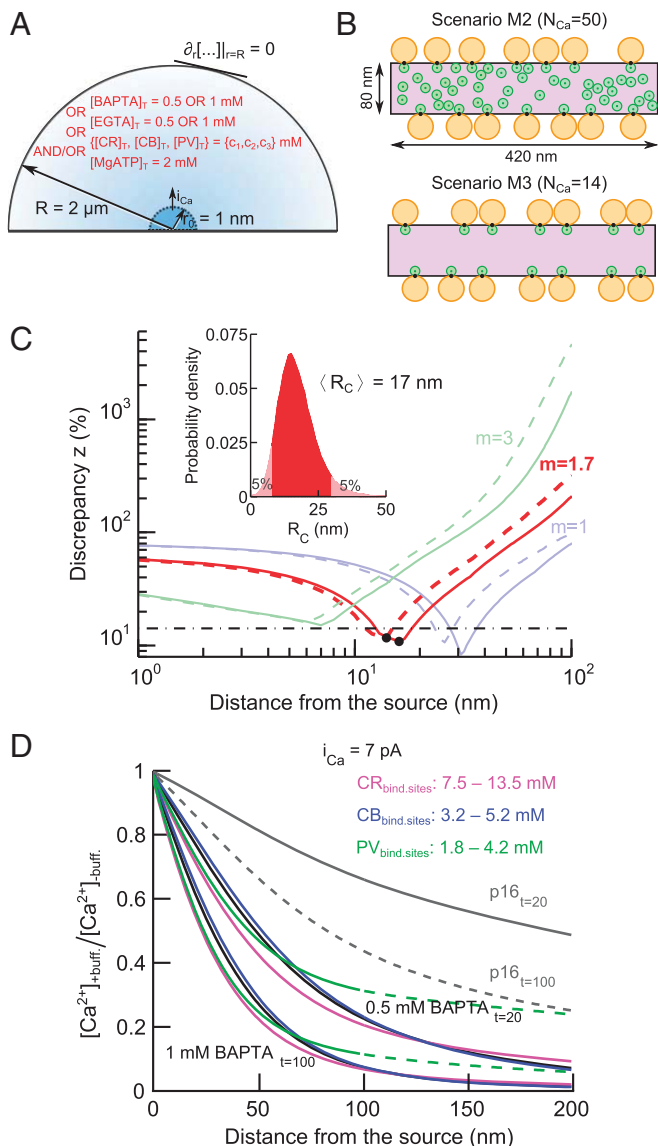
Tight Coupling Between Presynaptic Ca^{2+} Channels and Ca^{2+} Sensors of Exocytosis Limits the Interference of Mobile Ca^{2+} Buffers with IHC Synaptic Exocytosis. Our experimental observations suggest that endogenous EF-hand Ca^{2+}-binding proteins possess only modest ability to influence synaptic transmitter release in IHCs. This might reflect a very small distance between the Ca^{2+} source (i.e., Ca^{2+} channels) and vesicles undergoing fusion at the AZ ("coupling distance"). To determine this coupling distance in IHCs, we constructed a model that predicts the relative amount of exocytosis triggered when changing the distance between the Ca^{2+} source and

the Ca^{2+} sensor of release (Fig. 9*A* and *Materials and Methods*). We used this model to determine the effective coupling distance R_c (weighted average distance for all channels contributing to the $[Ca^{2+}]$ at the Ca^{2+} sensor; *Materials and Methods* and *SI Appendix*, section 8) that best matched exocytosis as observed experimentally under various Ca^{2+}-buffering conditions at room temperature. The model was based on the spatiotemporal profile of intracellular $[Ca^{2+}]$ resulting from Ca^{2+} influx through a single 1-nm radius hemispherical source. The integrated exocytosis was assumed to follow $[Ca^{2+}]$ according to a power law relation: $\Delta C_m \sim ([Ca^{2+}])^{m \cdot q}$. The exponent q accounts for the supralinear dependence of $[Ca^{2+}]$ on Q_{Ca}: $[Ca^{2+}] \sim Q_{Ca}^{1/q}$ that may result from partial buffer depletion at high Ca^{2+} influx (*SI Appendix*, section 7.4). The apparent Ca^{2+} cooperativity of exocytosis m was derived from prior experiments (36) and the value of 1.7 was obtained (*SI Appendix*, Fig. S6). We note that our previous studies aimed at determining the maximal apparent Ca^{2+} cooperativity of the RRP exocytosis, which is close to the intrinsic Ca^{2+} cooperativity, thus yielding an m in the range of 3–4 in 2-wk-old animals (36, 37). The model relationship of the present study needs to use an effective m value matched to the experimental conditions [i.e., in the presence of partial pool depletion/sensor saturation observed at high Q_{Ca} (36)].

Fig. 9*C* displays the discrepancy between modeled and experimentally observed exocytosis for assumed coupling distances between 1 and 100 nm and for three different values of m. When m is equal to 1.7, the minimum discrepancy is ~11%, which is smaller than the experimental error [~14% for the average $SEM(\Delta C_m)/mean(\Delta C_m)$ under different Ca^{2+} buffering conditions; Fig. 9*C*, dash-dotted line]. For small Ca^{2+} influx, i_{Ca}, buffer depletion was negligible and the discrepancy between the model and the measurements insensitive to the absolute value of i_{Ca}. For instance, a Ca^{2+} influx of 0.3 pA (approximating the
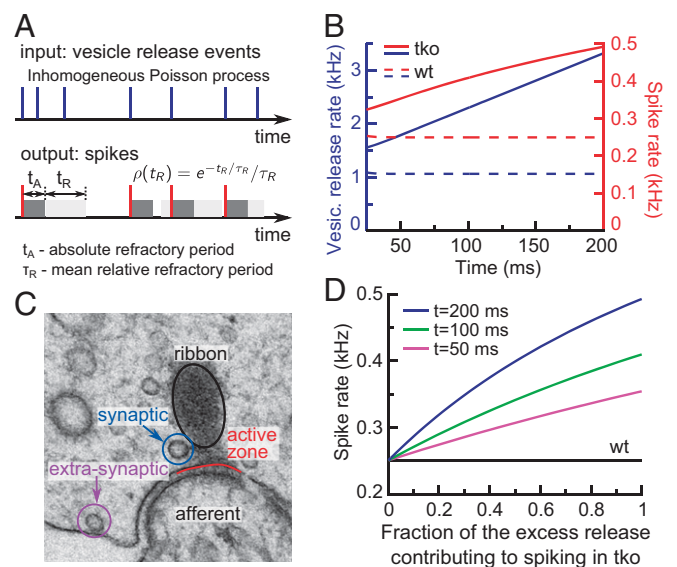
Fig. 8. Mathematical modeling of spike rates in WT and TKO SGNs. (*A*) Schematic representation of the model for release event to spike conversion (*Materials and Methods*). (*B*) Time dependence of vesicle release rate (blue) and spike rate (red) during sustained exocytosis (*t* > 25 ms) in WT (dashed lines) and TKO (solid lines). (*C*) An example of a transmission EM micrograph of an IHC ribbon synapse illustrating the concept of the synaptic vs. ectopic/extrasynaptic vesicle release. Image courtesy of C. Wichmann, University of Göttingen, Göttingen, Germany. (*D*) Modeled spike rate dependence on a putative fraction of the excess release contributing to the spike generation in SGNs in TKO compared with WT at average overall refractory period $t_A + τ_R = 1.1$ ms.

Fig. 9. Estimation of endogenous buffer concentrations and effective coupling distance between presynaptic Ca^{2+} channels and Ca^{2+} sensors of exocytosis. (*A*) Schematic representation of the hemispherical source model. (*B*) AZ scenarios M2 and M3 from Wong et al. (36) corresponding to the nanodomain-coupling regime. Orange discs represent RRP vesicles, green discs represent Ca^{2+} channels, black spots represent Ca^{2+} sensors of exocytosis, and violet area represents the presynaptic density. (*C*) Dependence of the discrepancy measure z on the effective coupling distance R_c. Different colors stand for different values of the apparent Ca^{2+} cooperativity of exocytosis, m. Dashed lines correspond to i_{Ca} of 0.3 pA; solid lines correspond to i_{Ca} of 7 pA. Black points denote the local minima of the discrepancy measure z for m of 1.7. Black dash-dotted line corresponds to the average of experimental $SEM[\Delta C_m]/mean[\Delta C_m]$ at different Ca^{2+} buffering conditions. (*Inset*) Bootstrap distribution of R_c estimate for m of 1.7 and i_{Ca} of 7 pA, generated as described in *Materials and Methods*. (*D*) Spatial profiles of $[Ca^{2+}]$ reduction, $[Ca^{2+}]_{+buff.}/[Ca^{2+}]_{-buff.}$, caused by particular intracellular buffers during Ca^{2+} influx (i_{ca} = 7 pA). Black lines show ratios of the Ca^{2+} profiles in the presence and absence of 0.5 mM and 1 mM BAPTA, gray lines in the presence and absence of endogenous buffers with concentrations as reported previously (8) in P16 rat IHCs (solid and dashed lines correspond to $[Ca^{2+}]$ spatial profiles at $t = 20$ ms and $t = 100$ ms, respectively). Colored lines are the best fits of $[Ca^{2+}]_{+buff.}/[Ca^{2+}]_{-buff.}$ with CR (magenta), CB (blue), and PVα (green) corresponding to 0.5 mM and 1 mM BAPTA.

single channel current at −17 mV) (38) drove negligible buffer depletion and led to estimates of the effective coupling distance of

15 nm, for m of 1.7 (Fig. 9C, dashed red line). As buffer depletion effects might be more prominent for larger Ca^{2+} influx, we also determined R_c assuming conditions of strong Ca^{2+} influx. To this end, we calculated the extent of buffer depletion near the AZ by using a hemispherical source equivalent to the entire presynaptic density in a mature synapse (surface area ~420 × 80 nm²) (36) and the maximal depolarization-evoked Ca^{2+} current per synapse in $Pv^{+/+}Cb^{+/+}Cr^{+/+}$ IHCs (15 pA). Near a 1-nm hemispherical source, a similar level of buffer depletion was obtained for an i_{Ca} of 7 pA (*SI Appendix*, section 7.3). Even for this extreme scenario, partial buffer depletion resulted in only a slight rightward shift of the discrepancy curves (Fig. 9C) with an R_c of 17 nm for an m of 1.7. We used bootstrapping to estimate the confidence range of the R_c estimate for i_{Ca} of 7 pA, which is affected by the estimation errors of m and ΔC_m. The 5–95 percentile range spanned from 8 to 30 nm (Fig. 9C, *Inset*).

In our previous work, we introduced some possible IHC presynaptic AZ arrangements (36). In spatially resolved simulations with two of these AZ topographies that correspond to the "nanodomain-coupling" regimen (Fig. 9B), R_c ranged between 15 and 27 nm (*SI Appendix*, section 8.4). They might thus be a good representation of the true IHC AZs. At the average R_c of 17 nm, the influence of the Ca^{2+} buffers on $[Ca^{2+}]$ at the Ca^{2+} sensor is small (0.5 mM BAPTA; Fig. 9D, black line). Together, these results indicate that endogenous Ca^{2+} buffers do not appreciably interfere with exocytosis at the AZ as a result of tight coupling between Ca^{2+} channels and Ca^{2+} sensors of exocytosis in IHCs of 2–3-wk-old mice. However, they effectively reduce extrasynaptic release at sites located more distant from the Ca^{2+} source.

Predicted Concentrations of Endogenous Buffers in Mature Mouse IHCs. Finally, we used the model to establish lower and upper bounds on the concentrations of endogenous Ca^{2+} buffers in IHCs. Exocytosis of a given readily releasable vesicle is governed by $[Ca^{2+}]$ at the Ca^{2+} sensor. According to ΔC_m recordings (Fig. 4), $[Ca^{2+}]$ at the Ca^{2+} sensor of exocytosis in $Pv^{+/+}Cb^{+/+}Cr^{+/+}$ IHCs should be matched in $Pv^{-/-}Cb^{-/-}Cr^{-/-}$ IHCs when they are loaded with 0.5 mM BAPTA. On the contrary, 1 mM BAPTA was required for adjusting sustained exocytosis of $Pv^{-/-}Cb^{-/-}Cr^{-/-}$ IHCs to WT levels, likely by limiting $[Ca^{2+}]$ further away from the Ca^{2+} channel. The spatial $[Ca^{2+}]$ profiles in the presence of these two BAPTA concentrations thus define the range of plausible $[Ca^{2+}]$ levels in the presence of endogenous buffers.

Fig. 9D shows the predicted ratios of the spatial $[Ca^{2+}]$ profiles with 0.5 and 1 mM BAPTA and the best approximation of these $[Ca^{2+}]$ profiles in the presence of the endogenous Ca^{2+} buffers CB, CR, and PVα. The spatial $[Ca^{2+}]$ profiles with 0.5 and 1 mM BAPTA were fitted 20 and 100 ms after stimulus onset, respectively. Solving the model with concentrations of endogenous mobile Ca^{2+} buffers (0.5 mM Ca^{2+}-binding sites in total) as estimated in rat IHCs by using quantitative immunogold EM (8) showed that these concentrations would be considerably less efficient than 0.5 mM BAPTA. According to our model, the concentration of Ca^{2+}-binding sites equivalent to 0.5–1 mM BAPTA is between 3.2 and 5.2 mM for CB, between 7.5 and 13.5 mM for CR, and between 1.8 and 4.2 mM for PVα when each buffer is considered separately (Fig. 9D). We note that, to convert these concentrations of Ca^{2+}-binding sites into equivalent protein concentrations, the values have to be divided by 4, 5, and 2 for CB, CR, and PV, respectively; thus, 0.5 mM BAPTA would correspond to 0.8, 1.5, and 0.9 mM of the three buffers. These values are consistent with previous estimates of EF-hand buffer concentrations in neurons (39–41) and hair cells (7). PVα alone could not fully reproduce the spatial $[Ca^{2+}]$ profiles predicted for 0.5 or 1 mM BAPTA over distances longer than 100 nm. However, it is likely that, at low concentrations, it acts together with higher amounts of CB and CR to shape the $[Ca^{2+}]$ signal at the IHC synapses.

As shown in Fig. 9D, the upper bounds on endogenous buffer Ca^{2+}-binding site concentrations were estimated by probing

$[Ca^{2+}]$ at a t = 100 ms after stimulus application. Negligible at first, the effect of accumulated Ca^{2+} on $[Ca^{2+}]$ during stimulation grows with time (*SI Appendix*, Fig. S7 *A* and *B*). This might affect the estimated upper bounds on endogenous Ca^{2+}-binding site concentrations. We thus reestimated the upper bounds on the Ca^{2+}-binding site concentrations by using spatial profiles of $[Ca^{2+}]$ calculated for times between 20 ms and 100 ms after stimulus application. As shown in *SI Appendix*, Fig. S10 (solid lines), the upper bound estimates were not considerably different at intermediate times for CB and PV (by ~20% higher at t = 20 ms than at t = 100 ms). For CR, the difference in the estimated Ca^{2+}-binding site concentrations was significant, being 50% higher at t = 20 ms than at t = 100 ms. In summary, our results suggest that the concentrations of endogenous buffers in IHCs are (approximately one order) higher than those obtained from immunogold counts (8) or the k_{on} rates of the buffers in situ (i.e., inside cells) are considerably higher than currently assumed (*SI Appendix*, section 7.1).

Discussion

In the present study we addressed the role of Ca^{2+} buffering EF-hand Ca^{2+}-binding proteins in the presynaptic function of IHCs. By using KO mice lacking PVα, CB, and CR, we indicate that mobile Ca^{2+} buffers shape IHC synaptic Ca^{2+} current by decreasing its amplitude and attenuating inactivation. Independent of their regulation of Ca^{2+} channels, they constrain transmitter release to AZs, ensuring efficient presynaptic function. By using exocytosis as readout together with mathematical modeling, we provide quantitative functional estimates for the concentration of the endogenous Ca^{2+} buffers in IHCs. Furthermore, we estimated the effective coupling distance between the Ca^{2+} channels and sensors for exocytosis in IHCs to be very short (mean value of R_c = 17 nm). Surprisingly, sound encoding and hearing were largely intact upon disruption of the three Ca^{2+} buffers. This can be explained by "Ca^{2+} nanodomain control" of exocytosis, minimizing the impact of buffers on stimulus–secretion coupling at AZs.

Ca^{2+} Buffering in Mammalian IHCs. Previous work on hair cells had provided estimates of the concentration of mobile Ca^{2+}-binding sites (5–9, 42–44), demonstrated the significance of mobile and immobile Ca^{2+} buffers for shaping the spatiotemporal properties of synaptic Ca^{2+} microdomains (2, 44–46), and investigated the sensitivity of exocytosis to Ca^{2+} buffering (9, 22, 37, 47–49). The $Pv^{-/-}Cb^{-/-}Cr^{-/-}$ mice now enabled us to refine the estimates of the concentration of mobile Ca^{2+}-binding sites in hair cells and to study the role of the three endogenous Ca^{2+} buffers in hair cell presynaptic function and afferent auditory signaling.

We found that the length constants of Ca^{2+} buffering, defined by Ca^{2+}-binding kinetics, diffusion coefficients, and concentrations of the three Ca^{2+} buffers, are large relative to the effective Ca^{2+} channel–Ca^{2+} sensor coupling distance. Consequently, exocytosis of the RRP, triggered by short depolarization pulses (<20 ms), was not noticeably affected by the three Ca^{2+} buffers. During longer depolarizations (≥20 ms), they reduced exocytosis in IHCs primarily by limiting Ca^{2+} spread from the AZ to ectopic release sites (Fig. 3*C*). In the substitution experiments, 1 mM BAPTA or EGTA reduced sustained exocytosis in $Pv^{-/-}Cb^{-/-}Cr^{-/-}$ IHCs to levels observed in $Pv^{+/+}Cb^{+/+}Cr^{+/+}$ mice, whereas lower concentrations (≤0.5 mM) were insufficient. This is in good agreement with previous results in mice, in which imaging of synaptic Ca^{2+} microdomains yielded values equivalent to 0.5–2 mM Ca^{2+}-binding sites of synthetic Ca^{2+} buffers (44). It also largely agrees with functional estimates on hair cells from other species (5–7, 9, 42). However, when estimating the concentrations of endogenous Ca^{2+}-binding sites, a significant difference in the diffusion coefficients and the Ca^{2+} (un)binding rates of synthetic and endogenous buffers has to be taken into account. Relying on published Ca^{2+}-binding rates, our model suggested that the concentration of Ca^{2+}-binding sites is approximately one order of magnitude higher than

reported in rat hair cells by using quantitative immunogold labeling (~0.54 mM endogenous Ca^{2+}-binding sites) (8). Alternatively, faster Ca^{2+}-binding rates of the endogenous buffers (an order of magnitude higher than published) could account for the observations, or it could be a combination of both effects.

Modulation of Ca^{2+} Influx by Ca^{2+} Buffering EF-Hand Ca^{2+}-Binding Proteins. A somewhat unexpected finding was the enhanced initial Ca^{2+} influx in $Pv^{-/-}Cb^{-/-}Cr^{-/-}$ IHCs. We did not observe more synapses in $Pv^{-/-}Cb^{-/-}Cr^{-/-}$ IHCs, which could have been an obvious cause for a greater number of Ca^{2+} channels. Instead, potential mechanisms for the increased Ca^{2+} influx include more Ca^{2+} channels per synapse and an enhanced open probability. In addition, we found that Ca^{2+}-current inactivation was enhanced in $Pv^{-/-}Cb^{-/-}Cr^{-/-}$ IHCs. Reduced Ca^{2+} buffering could increase Ca^{2+}-calmodulin–dependent inactivation (CDI). However, the enhanced inactivation was not reversed upon addition of synthetic Ca^{2+} chelators, which generally show little potency to antagonize CDI in mature IHCs (50, 51). Alternatively, EF-hand Ca^{2+}-binding proteins might directly interact with the channel, which is established for calmodulin and CaBPs (52–55). Indeed, CR suppresses CDI in $Ca_V2.1$ channels (but not $Ca_V1.2$ channels) in HEK 293-T cells (56).

Ca^{2+} Nanodomain Control of Fusion at the IHC Ribbon Synapse. Our previous work suggested that vesicle fusion at IHC ribbon synapses is induced by Ca^{2+} provided by one or few proximal Ca^{2+} channels (36, 37), nicknamed Ca^{2+} nanodomain control. In accordance, it has been demonstrated that not even 10 mM BAPTA completely blocks exocytosis in auditory hair cells (57). The present study took advantage of the disruption of endogenous Ca^{2+} buffers and substitution with synthetic Ca^{2+} buffers to further test this hypothesis. Based on experiments and modeling, we estimated the effective coupling distance R_c between Ca^{2+} channels and vesicular Ca^{2+} sensors at IHC AZs to be ~17 nm with a 5–95 percentile range of 8–30 nm. Our previously proposed AZ scenarios of nanodomain control (36) (Fig. 9*B*) give R_c values that fit well into the proposed range and might thus represent a good approximation of the true IHC AZ arrangement. Such tight coupling increases efficacy and speed of synaptic transmission.

Mobile IHC Ca^{2+} Buffering and Hearing. At first sight, finding a near-normal function of the cochlea in the $Pv^{-/-}Cb^{-/-}Cr^{-/-}$ mice is surprising. In SGNs, only spontaneous spiking rates were increased, which might be related to the increased Ca^{2+} influx. In fact, a regulation of spontaneous firing rates by modulating Ca^{2+} channel open probability has been shown (58). A minor increase (e.g., 17%) in the number or open probability of Ca^{2+} channels could explain the significantly enhanced spontaneous rate in SGNs of $Pv^{-/-}Cb^{-/-}Cr^{-/-}$ mice, but may not lead to an obvious enhancement of the evoked firing rates when driven by strong suprathreshold stimulation (Fig. 6; see also ref. 59).

Sound encoding during continued stimulation was not significantly altered despite increased sustained IHC exocytosis. Mathematical modeling indicated that this discrepancy reflects extrasynaptic exocytosis of vesicles that contributes less efficiently to sound coding, if at all. Alternative explanations such as refractoriness (Fig. 8*B* and *SI Appendix*, Fig. S5*D*) and increased AMPA desensitization (49) seem unlikely. A supralinear rise of exocytosis during prolonged stimulation was reported for turtle hair cells and interpreted as Ca^{2+}-dependent vesicle replenishment (60), but the relation to sound encoding remained to be elucidated, and a contribution of extrasynaptic exocytosis could not be ruled out.

Release away from the ribbon-type AZ has previously been observed in retinal bipolar cells (61, 62), where it is physiologically relevant for communication of bipolar cells to AII amacrine cells (62). The results of our study suggest that such extrasynaptic exocytosis of IHCs has little influence on the postsynaptic SGN

spiking. Together with previous studies demonstrating a good correlation between the presynaptic release rate and postsynaptic spiking in WT and bassoon mutant animals (24), it further suggests little or no ectopic release in the presence of endogenous Ca^{2+} buffers. We conclude that the properties of the endogenous buffer Ca^{2+} binding and their diffusion kinetics allow for a metabolically efficient control of the Ca^{2+}-dependent sound encoding.

Materials and Methods

Animals. The TKO line $Pv^{-/-}Cb^{-/-}Cr^{-/-}$ was generated by breeding the two double KO (DKO) lines, $Pv^{-/-}Cb^{-/-}$ (63) (genetic background: C57BL/6 × 129/OlaHsd × 129/SvJ) and $Pv^{-/-}Cr^{-/-}$ (64) (genetic background: C57BL/6 × 129/OlaHsd). The initial double-heterozygous litters ($Pv^{-/-}Cb^{+/-}Cr^{+/-}$) were used to generate the TKO line. The genotype was determined by PCR for the mutated loci in the three genes, *Pvalb*, *Calb1*, and *Calb2*, as reported before (65–67). The line was then maintained as an inbred line with a mixed C57BL/6 × 129/(OlaHsd × SvJ) background. We studied the auditory phenotype of DKO ($Pv^{-/-}Cb^{-/-}$) and TKO ($Pv^{-/-}Cb^{-/-}Cr^{-/-}$) mice. Control experiments were performed on WT animals ($Pv^{+/+}Cb^{+/+}Cr^{+/+}$) with the most similar background to TKO mice (mixed background of C57BL/6 and 129/OlaHsd). These animals originated from a previous heterozygote ($Pv^{+/-}Cr^{+/-}$) breeding. All experiments were done in compliance with the national animal care guidelines and were approved by the board for animal welfare of the University Medical Center Goettingen, the animal welfare office of the state of Lower Saxony, and the institutional animal care and use committee of the Massachusetts Eye and Ear Infirmary.

Immunohistochemistry and Confocal Microscopy. Immunohistochemistry was performed as described previously (19). To analyze the abundance of mitochondria, we fixed organs of Corti in methanol at −20 °C for 20 min and double-stained hair cells for PNPase (mitochondria marker) (29) and CtBP2 (19) (to identify ribbons). In all other cases, organs were fixed with 4% (wt/vol) formaldehyde for 10–60 min on ice. The following antibodies were used: mouse IgG1 anti-CtBP2 (1:200; BD Biosciences), rabbit anti-GluR2/3 (1:200; Chemicon), mouse anti–calbindin-D28k, mouse anti-calretinin, mouse anti–parvalbumin-α, rabbit anti-oncomodulin (anti–parvalbumin-β; all 1:500; Swant), rabbit anti-PNPase (1:500; Proteintech), rabbit VGlut3 (1:500; Abcam), mouse 5F10 (pan-PMCA marker, 1:200; Abcam) and secondary Alexa Fluor 488- and Alexa Fluor 568-labeled antibodies (1:200; Molecular Probes). In some instances, nuclei were stained with Hoechst 34580 (1:1,000; Molecular Probes). Confocal images were acquired by using a laser-scanning confocal microscope (TCS SP2; Leica Microsystems) with 488-nm (Ar) and 561-nm (He-Ne) lasers and a 63× oil immersion objective. z-axis stacks of 2D images were taken with a step size of 0.5 μm. Z-projections were done in ImageJ (National Institutes of Health). The ribeye/CtBP2 and GluR2/3 immunofluorescence spots were counted in the z-stacks and divided by the number of IHCs. Juxtaposed spots of pre- and postsynaptic immunofluorescence were taken to identify intact IHC ribbon synapses. To assess the perisynaptic abundance of mitochondria, we measured the cumulative PNPase immunofluorescence intensity within a circle with a radius of 0.5 μm around the center of mass of the ribbon (CtBP2 immunofluorescence) in confocal sections of IHCs by using a custom-written MATLAB routine.

Patch-Clamp Recordings. KO ($Pv^{-/-}Cb^{-/-}Cr^{-/-}$) and WT mice ($Pv^{+/+}Cb^{+/+}Cr^{+/+}$) with postnatal ages of 14–23 d were killed by decapitation. The apical cochlear turns were dissected in Hepes Hanks solution containing (in mM): 5.36 KCl, 141.7 NaCl, 1 $MgCl_2$, 0.5 $MgSO_4$, 10 Hepes, 11.1 D-glucose, and 3.42 L-glutamine, pH 7.2. IHCs were patch-clamped in the perforated-patch configuration as previously described (17). For estimation of endogenous buffer equivalents, $Pv^{-/-}Cb^{-/-}Cr^{-/-}$ IHCs were patch-clamped in the ruptured-patch configuration. The pipette solution contained (in mM): 130 Cs-gluconate, 10 TEA-Cl, 10 4-AP (4-aminopyridine; Merck), 1 $MgCl_2$, 10 Hepes, 300 μg/mL amphotericin B (for perforated patch-clamp experiments; Calbiochem), 2 MgATP, and 0.3 NaGTP (both for ruptured-patch experiments), pH 7.2, with osmolarity of approximately 290 mOsm. In ruptured-patch experiments, pipette solution additionally contained different concentrations of exogenous buffers: 0.1, 0.5, or 1 mM BAPTA or 0.5 or 1 mM EGTA. The extracellular solution contained (in mM): 106 NaCl (113 mM in Fig. 3 *G* and *H*), 35 TEA-Cl, 2.8 KCl, 5 $CaCl_2$ (2 mM in Fig. 3 *G* and *H*), 1 $MgCl_2$, 10 Hepes, 1 CsCl, 11.1 D-glucose, pH 7.2, with osmolarity of approximately 300 mOsm. All chemicals were obtained from Sigma-Aldrich unless stated otherwise.

We used an EPC-9 amplifier (HEKA Electronics) controlled by Pulse software (HEKA Electronics). C_m increments (ΔC_m) were measured as previously described (22), averaging 400 ms before and after (skipping the first 40 ms) depolarization. To measure ΔC_m, IHCs were stimulated by depolarizations of different durations to peak Ca^{2+} current potential at

intervals of 30–60 s. For Ca^{2+} current inactivation experiments, IHCs were depolarized for 100 ms. All voltages were corrected for liquid junction potential (−17 mV). In ruptured-patch experiments, measurements were initiated an average of 2.5 min after patch rupture to allow for the diffusion of exogenous buffer into the cytosol. The waiting time depended on the series resistance R_s, which relates to the kinetics of diffusional exchange as previously described (68). Unless stated otherwise, all recordings were performed at room temperature.

ABRs, Otoacoustic Emissions, and Recordings from Single SGNs. Recordings of ABRs and DPOAEs (69) as well as extracellular recordings from SGNs (23, 24) were performed as described previously. Briefly, 12–16-wk-old mice were anesthetized by i.p. injection of xylazine (2.5 mg/kg) and ketamine (125 mg/kg, ABR and DPOAE) or xylazine (5 mg/kg) and urethane (1.32 mg/kg, for single SGN recordings). The occipital bone and cerebellum were partly removed, and SGNs near the auditory nerve's entry zone into the cochlear nucleus were approached by a glass microelectrode filled with 2 M KCl and 4% (wt/vol) methylene blue during noise burst stimulation. Sound-responsive neurons were first characterized by obtaining their spontaneous rate, tuning curves, and responses to 50-ms tone bursts presented at the CF of the SGN, 30 dB above threshold. SGNs were distinguished from primary cochlear nucleus units based on their primary-like response characteristics and irregular firing pattern, as well as by the electrode position, which was confirmed after the end of the experiment. Spike detection was performed online based on a manually set amplitude criterion.

Data Analysis. Data analysis was performed in Igor Pro (Wavemetrics) and MATLAB (Mathworks) software, confocal images were assembled for display by using ImageJ and Photoshop (Adobe Systems), and final figures were composed in Illustrator (Adobe Systems). To calculate activation time constants of Ca^{2+} currents, data were fitted with the following function: $I(t) = I_0 + I_{max} \times (1 - e^{-t/\tau})^p$. In most cases, data could be well fitted with the parameter power (p) fixed to 2, or else p was set as a free parameter. Mean ΔC_m and Ca^{2+} current estimates present grand averages calculated from the mean estimates of individual IHCs. All results are expressed as mean ± SEM. Data were tested for randomness, normality (Jarque–Bera test), and equality of variances (F-test) and compared for statistical significance by using a Student t test (in case of normal distribution and equal variance of both samples) or Wilcoxon rank-sum test.

Mathematical Modeling. Mathematical modeling was done by using MATLAB R2012b (Mathworks).

Conversion of neurotransmitter release to spikes. The release rate was inferred from exocytic ΔC_m estimates of IHCs (at room temperature). In the model, the SGN generates a spike in response to each release event unless it is in the refractory state, which lasts for a period of $t_A + t_R$ (t_A is the absolute refractory period, t_R the relative refractory period; Fig. 9*A*). Although t_A was fixed for a particular SGN, t_R was a random number drawn from a monoexponential distribution with a mean value τ_R. The stationary spike rate (R_{sp}^{∞}) is related to the release rate (R_r^{∞}) and the refractory period in the following way (32): $R_{sp}^{\infty} = R_r^{\infty}/[1 + R_r^{\infty} \cdot (t_A + \tau_R)]$. Given that changes in the sustained release rate (between 50 and 200 ms; Fig. 9*B*) are slow in comparison with the duration of the refractory period, we applied the adiabatic approximation: $R_{sp}(t) \sim R_r(t)/[1 + R_r(t) \cdot (t_A + \tau_R)]$. To estimate the release rate $R_r(t)$, the experimental $\Delta C_m(t)$ values were first converted to the number of released synaptic vesicles, $N(t)$: $N(t) = sc \cdot \Delta C_m(t)/(C_{sv} \cdot N_{syn})$. Here, a C_{sv} of 44.5 aF was taken as average ΔC_m upon fusion of single synaptic vesicle (70), the N_{syn} of 12 is the number of synapses per IHC as obtained from immunohistochemistry (Fig. 2). $sc \leq 1$ is a scaling coefficient to account for differences between in vitro (patch-clamp) and in vivo (single unit recordings) conditions [such as the amplitude of stimulus-evoked IHC depolarization, temperature, ion homeostasis (e.g., $[Ca^{2+}]_e$), and/or the case that a single release event may correspond to release of a few synaptic vesicles] (70, 71). Next, $N(t)$ was fitted by $A \cdot t + B \cdot (1 - e^{-t/\tau})^n$ for the $Pv^{+/+}Cb^{+/+}Cr^{+/+}$ IHCs and $A \cdot t + B \cdot (1 - e^{-t/\tau})^n + t \cdot (a \cdot t + b)$ for the $Pv^{-/-}Cb^{-/-}Cr^{-/-}$ IHCs (*SI Appendix*, Fig. S2A). Finally, the release rate $R_r(t)$ was obtained by calculating the time derivative of $N(t)$.

Refractory periods. We collected experimental cumulative interspike intervals corresponding to the sustained part of PSTH (30–50-ms interval; Fig. 6*C*). The parameter t_A was estimated as the interspike interval smaller than 99.5% of the remaining interspike intervals in the sample from the SGN under consideration. To estimate τ_R, the cumulative interspike interval distribution excluding the 0.5% smallest interspike intervals was fitted for each SGN with the expression (which applies for the model formulated earlier):

8

$$P^M(t) = \begin{cases} 1 - \dfrac{(\tau_s - \tau_R - t_A)^{-1} \cdot e^{-\frac{(t-t_A)}{\tau_R}} - \tau_R^{-1} \cdot e^{-\frac{(t-t_A)}{\tau_s - \tau_R - t_A}}}{(\tau_s - \tau_R - t_A)^{-1} - \tau_R^{-1}}, & \text{if } t > t_A \\ 0, & \text{if } t \le t_A \end{cases} \quad [1]$$

where τ_s is experimental estimate of the mean interspike interval. The fitting was done by minimizing the relative discrepancy between the model and the experimental cumulative distributions $\sum_i |P^M_i - P^E_i|/P^E_i$ in the range of P^E values between 0 and 0.9 (*SI Appendix*, Fig. S5 *A* and *B*).

Concentrations of the endogenous Ca²⁺ buffers and effective coupling distance between presynaptic Ca²⁺ channels and Ca²⁺ sensors of exocytosis. Buffer concentrations and the effective Ca²⁺ channel–exocytosis coupling distance (i.e., R_c) were estimated by using a hemispherical Ca²⁺ source model (Fig. 9*A*). A hemispherical Ca²⁺ source with 1-nm radius was embedded in a hemispherical volume with 2-μm radius, which corresponds to the mean distance between neighboring synapses in IHCs (72). The simulation volume was filled with 2 mM MgATP and the chosen concentrations of BAPTA, EGTA, or endogenous buffers. Initially, the system was in a steady state with uniform distribution of Ca²⁺, Mg²⁺, and buffers. The boundary of the simulation volume was assumed to be reflective for all considered particle species. This effectively mimics the effect of Ca²⁺ coming from the neighboring synapses and also fixes the amount of buffers available per synapse. On the contrary, pure reflection of Ca²⁺ from the boundary ignores Ca²⁺ removal by the pumps and through exchange with the remaining volume of the IHC, which is considerably larger (2.2 pL) (73) than the volume of 12 hemispheres of 2 μm each (~0.02 pL). It is shown in *SI Appendix*, section 7.6, however, that these effects do not considerably influence our results. Ca²⁺ concentration at time t and distance r from the source, $[Ca^{2+}](t,r)$, is governed by a system of reaction–diffusion equations as described in *SI Appendix*, section 7.1.

We assumed that the amount of release in a 20-ms time window was proportional to $([Ca^{2+}](r))^{m \cdot q(r)}$. $[Ca^{2+}](r)$ was estimated 20 ms after the onset of stimulus. During this time window, $[Ca^{2+}](r)$ in simulations was essentially stationary (apart from the initial equilibration of the profile, which, however, is very fast; *SI Appendix*, section 7.2).

To find R_c based on the experimental data, we minimized the mean relative deviation of the ratios of modeled and experimentally observed release during the first 20 ms in different Ca²⁺ buffering conditions:

$$z(r) = \sum_{j=1}^{4} w_j \cdot \frac{|a_j - b_j(r)|}{\min(a_j, b_j(r))} \quad [2]$$

Here, $a_j = \Delta C_{m,0}/\Delta C_{m,j}$ is the ratio of ΔC_m values estimated in TKO IHCs (at room temperature) with 1 mM BAPTA ($\Delta C_{m,0}$) and 1 mM EGTA ($j = 1$), 0.5 mM BAPTA ($j = 2$), 0.5 mM EGTA ($j = 3$), or no exogenous buffer ($j = 4$). $b_j =$ ($[Ca^{2+}]_0(r)/([Ca^{2+}]_j(r))^{m \cdot q(r)}$, $[Ca^{2+}]_0(r)$—the model's estimate of $[Ca^{2+}]$ at distance r from the source in TKO IHCs loaded with 1 mM BAPTA, $[Ca^{2+}]_j(r)$—the model's estimates of $[Ca^{2+}]$ at distance r from the source in the other four buffering conditions as mentioned earlier. w_j is relative weight of the jth term in the sum, which depends on the ratio of the mean and SEM values of experimental ΔC_m estimates: $w_j = [\Delta C_{m,j}/SEM(\Delta C_{m,j})]/\sum_{i=1}^{4}[\Delta C_{m,i}/SEM(\Delta C_{m,i})]$. Note that ΔC_m estimated in different buffering conditions, corresponds to slightly different Q_{Ca} values which reflect different influx of Ca²⁺. To take this into account, we rescaled the actual i_{Ca} values for estimating each $[Ca^{2+}]$. This was done so that the average $Q_{Ca} = 3.78$ pC measured for 20 ms depolarization in $Pv^{+/+}Cb^{+/+}Cr^{+/+}$ IHCs corresponded to the nominal i_{Ca} values. Bootstrapping was used to estimate the confidence interval of R_c (given as a 5–95 percentile range; Fig. 9*C*) because of uncertainty in experimental estimates of m and ΔC_m for different buffering conditions. A total of 10^5 artificial data sets were generated by drawing numbers from normal distributions with their mean and SD values set to experimentally estimated mean and SEM values.

As shown in *SI Appendix*, section 8, the R_c of a particular AZ is not simply the average distance between Ca²⁺ sensors of exocytosis and Ca²⁺ channels. Rather, it is a nonlinear average of those distances weighted by the contributions of the corresponding channels to the $[Ca^{2+}]$ driving exocytosis at the AZ. This aspect is relevant for the functional interpretation of R_c. Qualitatively, the more a particular Ca²⁺ channel contributes to $[Ca^{2+}]$ at a particular release site and the more that release site contributes to the overall neurotransmitter release at the AZ, the more the distance between the channel and the corresponding Ca²⁺ sensor of exocytosis weighs in determining the R_c.

The fitting procedure for endogenous buffer concentration estimation was based on minimization of a relative discrepancy measure of the form $\sum_i |c_1(r_i) - c_2(r_i)|/[c_1(r_i) + c_2(r_i)]$ for $r \in [0; 200]$ nm.

1. Lenzi D, Roberts WM (1994) Calcium signalling in hair cells: Multiple roles in a compact cell. *Curr Opin Neurobiol* 4(4):496–502.
2. Roberts WM (1994) Localization of calcium signals by a mobile calcium buffer in frog saccular hair cells. *J Neurosci* 14(5 pt 2):3246–3262.
3. Schwaller B, Meyer M, Schiffmann S (2002) 'New' functions for 'old' proteins: The role of the calcium-binding proteins calbindin D-28k, calretinin and parvalbumin, in cerebellar physiology. Studies with knockout mice. *Cerebellum* 1(4):241–258.
4. Schneggenburger R, Neher E (2005) Presynaptic calcium and control of vesicle fusion. *Curr Opin Neurobiol* 15(3):266–274.
5. Heller S, Bell AM, Denis CS, Choe Y, Hudspeth AJ (2002) Parvalbumin 3 is an abundant Ca2+ buffer in hair cells. *J Assoc Res Otolaryngol* 3(4):488–498.
6. Roberts WM (1993) Spatial calcium buffering in saccular hair cells. *Nature* 363(6424): 74–76.
7. Edmonds B, Reyes R, Schwaller B, Roberts WM (2000) Calretinin modifies presynaptic calcium signaling in frog saccular hair cells. *Nat Neurosci* 3(8):786–790.
8. Hackney CM, Mahendrasingam S, Penn A, Fettiplace R (2005) The concentrations of calcium buffering proteins in mammalian cochlear hair cells. *J Neurosci* 25(34):7867–7875.
9. Johnson SL, Forge A, Knipper M, Münkner S, Marcotti W (2008) Tonotopic variation in the calcium dependence of neurotransmitter release and vesicle pool replenishment at mammalian auditory ribbon synapses. *J Neurosci* 28(30):7670–7678.
10. Servais L, et al. (2005) Mono- and dual-frequency fast cerebellar oscillation in mice lacking parvalbumin and/or calbindin D-28k. *Eur J Neurosci* 22(4):861–870.
11. Racay P, Gregory P, Schwaller B (2006) Parvalbumin deficiency in fast-twitch muscles leads to increased 'slow-twitch type' mitochondria, but does not affect the expression of fiber specific proteins. *FEBS J* 273(1):96–108.
12. Farré-Castany MA, et al. (2007) Differences in locomotor behavior revealed in mice deficient for the calcium-binding proteins parvalbumin, calbindin D-28k or both. *Behav Brain Res* 178(2):250–261.
13. Kreiner L, Christel CJ, Benveniste M, Schwaller B, Lee A (2010) Compensatory regulation of Cav2.1 Ca2+ channels in cerebellar Purkinje neurons lacking parvalbumin and calbindin D-28k. *J Neurophysiol* 103(1):371–381.
14. Schwaller B (2012) The use of transgenic mouse models to reveal the functions of Ca2+ buffer proteins in excitable cells. *Biochim Biophys Acta* 1820(8):1294–1303.
15. Hackney CM, Mahendrasingam S, Jones EM, Fettiplace R (2003) The distribution of calcium buffering proteins in the turtle cochlea. *J Neurosci* 23(11):4577–4589.
16. Platzer J, et al. (2000) Congenital deafness and sinoatrial node dysfunction in mice lacking class D L-type Ca2+ channels. *Cell* 102(1):89–97.
17. Brandt A, Striessnig J, Moser T (2003) CaV1.3 channels are essential for development and presynaptic activity of cochlear inner hair cells. *J Neurosci* 23(34):10832–10840.
18. Dou H, et al. (2004) Null mutation of alpha1D Ca2+ channel gene results in deafness but no vestibular defect in mice. *J Assoc Res Otolaryngol* 5(2):215–226.
19. Khimich D, et al. (2005) Hair cell synaptic ribbons are essential for synchronous auditory signalling. *Nature* 434(7035):889–894.
20. Naraghi M, Neher E (1997) Linearized buffered Ca2+ diffusion in microdomains and its implications for calculation of [Ca2+] at the mouth of a calcium channel. *J Neurosci* 17(18):6961–6973.
21. Nägerl UV, Novo D, Mody I, Vergara JL (2000) Binding kinetics of calbindin-D(28k) determined by flash photolysis of caged Ca(2+). *Biophys J* 79(6):3009–3018.
22. Moser T, Beutner D (2000) Kinetics of exocytosis and endocytosis at the cochlear inner hair cell afferent synapse of the mouse. *Proc Natl Acad Sci USA* 97(2):883–888.
23. Taberner AM, Liberman MC (2005) Response properties of single auditory nerve fibers in the mouse. *J Neurophysiol* 93(1):557–569.
24. Buran BN, et al. (2010) Onset coding is degraded in auditory nerve fibers from mutant mice lacking synaptic ribbons. *J Neurosci* 30(22):7587–7597.
25. Jing Z, et al. (2013) Disruption of the presynaptic cytomatrix protein bassoon degrades ribbon anchorage, multiquantal release, and sound encoding at the hair cell afferent synapse. *J Neurosci* 33(10):4456–4467.
26. Dallos P, Harris D (1978) Properties of auditory nerve responses in absence of outer hair cells. *J Neurophysiol* 41(2):365–383.
27. Frank T, et al. (2010) Bassoon and the synaptic ribbon organize Ca²⁺ channels and vesicles to add release sites and promote refilling. *Neuron* 68(4):724–738.
28. Chen G, et al. (2006) Deficiency in parvalbumin, but not in calbindin D-28k upregulates mitochondrial volume and decreases smooth endoplasmic reticulum surface

9

selectively in a peripheral, subplasmalemmal region in the soma of Purkinje cells. *Neuroscience* 142(1):97–105.

29. von Ameln S, et al. (2012) A mutation in PNPT1, encoding mitochondrial-RNA-import protein PNPase, causes hereditary hearing loss. *Am J Hum Genet* 91(5):919–927.

30. Pangršič T, et al. (2010) Hearing requires otoferlin-dependent efficient replenishment of synaptic vesicles in hair cells. *Nat Neurosci* 13(7):869–876.

31. Cho S, Li G-L, von Gersdorff H (2011) Recovery from short-term depression and facilitation is ultrafast and Ca2+ dependent at auditory hair cell synapses. *J Neurosci* 31(15):5682–5692.

32. Young ED, Barta PE (1986) Rate responses of auditory nerve fibers to tones in noise near masked threshold. *J Acoust Soc Am* 79(2):426–442.

33. Li J, Young ED (1993) Discharge-rate dependence of refractory behavior of cat auditory-nerve fibers. *Hear Res* 69(1-2):151–162.

34. Lenzi D, Crum J, Ellisman MH, Roberts WM (2002) Depolarization redistributes synaptic membrane and creates a gradient of vesicles on the synaptic body at a ribbon synapse. *Neuron* 36(4):649–659.

35. Kantardzhieva A, Liberman MC, Sewell WF (2013) Quantitative analysis of ribbons, vesicles, and cisterns at the cat inner hair cell synapse: correlations with spontaneous rate. *J Comp Neurol* 521(14):3260–3271.

36. Wong AB, et al. (2014) Developmental refinement of hair cell synapses tightens the coupling of Ca2+ influx to exocytosis. *EMBO J* 33(3):247–264.

37. Brandt A, Khimich D, Moser T (2005) Few CaV1.3 channels regulate the exocytosis of a synaptic vesicle at the hair cell ribbon synapse. *J Neurosci* 25(50):11577–11585.

38. Zampini V, et al. (2013) Burst activity and ultrafast activation kinetics of CaV1.3 Ca²⁺ channels support presynaptic activity in adult gerbil hair cell ribbon synapses. *J Physiol* 591(Pt 16):3811–3820.

39. Saftenku EÈ (2012) Effects of calretinin on Ca2+ signals in cerebellar granule cells: implications of cooperative Ca2+ binding. *Cerebellum* 11(1):102–120.

40. Eggermann E, Jonas P (2012) How the 'slow' Ca(2+) buffer parvalbumin affects transmitter release in nanodomain-coupling regimes. *Nat Neurosci* 15(1):20–22.

41. Maeda H, Ellis-Davies GCR, Ito K, Miyashita Y, Kasai H (1999) Supralinear Ca2+ signaling by cooperative and mobile Ca2+ buffering in Purkinje neurons. *Neuron* 24(4):989–1002.

42. Tucker TR, Fettiplace R (1996) Monitoring calcium in turtle hair cells with a calcium-activated potassium channel. *J Physiol* 494(Pt 3):613–626.

43. Ricci AJ, Wu YC, Fettiplace R (1998) The endogenous calcium buffer and the time course of transducer adaptation in auditory hair cells. *J Neurosci* 18(20):8261–8277.

44. Frank T, Khimich D, Neef A, Moser T (2009) Mechanisms contributing to synaptic Ca2+ signals and their heterogeneity in hair cells. *Proc Natl Acad Sci USA* 106(11):4483–4488.

45. Tucker T, Fettiplace R (1995) Confocal imaging of calcium microdomains and calcium extrusion in turtle hair cells. *Neuron* 15(6):1323–1335.

46. Issa NP, Hudspeth AJ (1996) The entry and clearance of Ca2+ at individual presynaptic active zones of hair cells from the bullfrog's sacculus. *Proc Natl Acad Sci USA* 93(18):9527–9532.

47. Beutner D, Moser T (2001) The presynaptic function of mouse cochlear inner hair cells during development of hearing. *J Neurosci* 21(13):4593–4599.

48. Spassova MA, et al. (2004) Evidence that rapid vesicle replenishment of the synaptic ribbon mediates recovery from short-term adaptation at the hair cell afferent synapse. *J Assoc Res Otolaryngol* 5(4):376–390.

49. Goutman JD, Glowatzki E (2007) Time course and calcium dependence of transmitter release at a single ribbon synapse. *Proc Natl Acad Sci USA* 104(41):16341–16346.

50. Johnson SL, Marcotti W (2008) Biophysical properties of CaV1.3 calcium channels in gerbil inner hair cells. *J Physiol* 586(4):1029–1042.

51. Grant L, Fuchs P (2008) Calcium- and calmodulin-dependent inactivation of calcium channels in inner hair cells of the rat cochlea. *J Neurophysiol* 99(5):2183–2193.

52. Peterson BZ, DeMaria CD, Adelman JP, Yue DT (1999) Calmodulin is the Ca2+ sensor for Ca2+ -dependent inactivation of L-type calcium channels. *Neuron* 22(3):549–558.

53. Lee A, et al. (1999) Ca2+/calmodulin binds to and modulates P/Q-type calcium channels. *Nature* 399(6732):155–159.

54. Lee A, et al. (2002) Differential modulation of Ca(v)2.1 channels by calmodulin and Ca2+-binding protein 1. *Nat Neurosci* 5(3):210–217.

55. Haeseleer F, et al. (2000) Five members of a novel Ca(2+)-binding protein (CABP) subfamily with similarity to calmodulin. *J Biol Chem* 275(2):1247–1260.

56. Christel CJ, et al. (2012) Calretinin regulates Ca2+-dependent inactivation and facilitation of Ca(v)2.1 Ca2+ channels through a direct interaction with the α12.1 subunit. *J Biol Chem* 287(47):39766–39775.

57. Graydon CW, Cho S, Li G-L, Kachar B, von Gersdorff H (2011) Sharp Ca²⁺ nanodomains beneath the ribbon promote highly synchronous multivesicular release at hair cell synapses. *J Neurosci* 31(46):16637–16650.

58. Robertson D, Paki B (2002) Role of L-type Ca2+ channels in transmitter release from mammalian inner hair cells. II. Single-neuron activity. *J Neurophysiol* 87(6):2734–2740.

59. Wong AB, et al. (2013) Concurrent maturation of inner hair cell synaptic Ca2+ influx and auditory nerve spontaneous activity around hearing onset in mice. *J Neurosci* 33(26):10661–10666.

60. Schnee ME, Santos-Sacchi J, Castellano-Muñoz M, Kong J-H, Ricci AJ (2011) Calcium-dependent synaptic vesicle trafficking underlies indefatigable release at the hair cell afferent fiber synapse. *Neuron* 70(2):326–338.

61. Midorikawa M, Tsukamoto Y, Berglund K, Ishii M, Tachibana M (2007) Different roles of ribbon-associated and ribbon-free active zones in retinal bipolar cells. *Nat Neurosci* 10(10):1268–1276.

62. Mehta B, et al. (2014) Global Ca2+ signaling drives ribbon-independent synaptic transmission at rod bipolar cell synapses. *J Neurosci* 34(18):6233–6244.

63. Vecellio M, Schwaller B, Meyer M, Hunziker W, Celio MR (2000) Alterations in Purkinje cell spines of calbindin D-28 k and parvalbumin knock-out mice. *Eur J Neurosci* 12(3):945–954.

64. Bouilleret V, Schwaller B, Schurmans S, Celio MR, Fritschy JM (2000) Neurodegenerative and morphogenic changes in a mouse model of temporal lobe epilepsy do not depend on the expression of the calcium-binding proteins parvalbumin, calbindin, or calretinin. *Neuroscience* 97(1):47–58.

65. Airaksinen MS, et al. (1997) Ataxia and altered dendritic calcium signaling in mice carrying a targeted null mutation of the calbindin D28k gene. *Proc Natl Acad Sci USA* 94(4):1488–1493.

66. Schwaller B, et al. (1999) Prolonged contraction-relaxation cycle of fast-twitch muscles in parvalbumin knockout mice. *Am J Physiol* 276(2 pt 1):C395–C403.

67. Schiffmann SN, et al. (1999) Impaired motor coordination and Purkinje cell excitability in mice lacking calretinin. *Proc Natl Acad Sci USA* 96(9):5257–5262.

68. Pusch M, Neher E (1988) Rates of diffusional exchange between small cells and a measuring patch pipette. *Pflugers Arch* 411(2):204–211.

69. Pauli-Magnus C, et al. (2007) Detection and differentiation of sensorineural hearing loss in mice using auditory steady-state responses and transient auditory brainstem responses. *Neuroscience* 149(3):673–684.

70. Neef A, et al. (2007) Probing the mechanism of exocytosis at the hair cell ribbon synapse. *J Neurosci* 27(47):12933–12944.

71. Glowatzki E, Fuchs PA (2002) Transmitter release at the hair cell ribbon synapse. *Nat Neurosci* 5(2):147–154.

72. Meyer AC, et al. (2009) Tuning of synapse number, structure and function in the cochlea. *Nat Neurosci* 12(4):444–453.

73. Lenzi D, Runyeon JW, Crum J, Ellisman MH, Roberts WM (1999) Synaptic vesicle populations in saccular hair cells reconstructed by electron tomography. *J Neurosci* 19(1):119–132.

Supplementary Material for

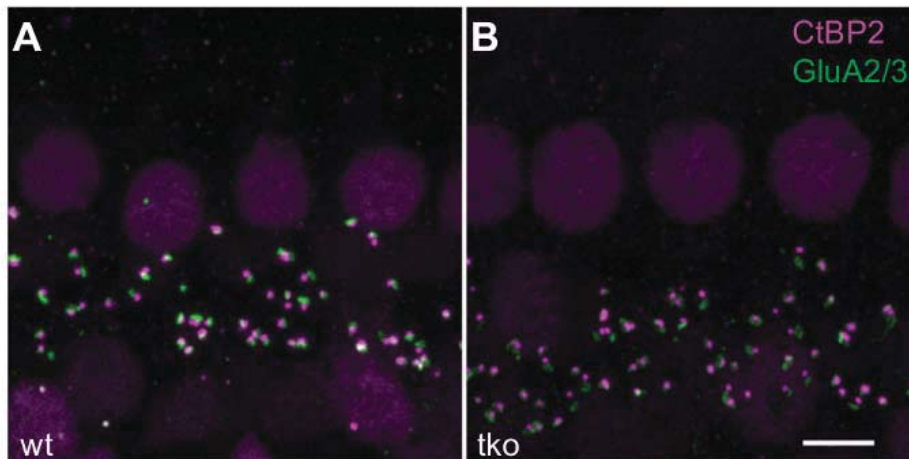# EF-hand Protein Ca^{2+} Buffers Regulate Ca^{2+} Influx and Exocytosis in Sensory Hair Cells

by

Tina Pangršič, Mantas Gabrielaitis, Susann Michanski, Beat Schwaller, Fred Wolf, Nicola Strenzke, Tobias Moser

Contents

1 Supplementary Figure 1

Figure S1: Comparable number of ribbon synapses in the IHCs of the triple buffer knockout and wild-type mice. (A – B) Confocal images of whole-mounts of organs of Corti double stained for the presynaptic marker CtBP2/Ribeye (magenta) and postsynaptic marker GluA 2/3 (green). The number of synapses in tko IHCs (B) was comparable to that of wt IHCs (A). Intact synapses are defined by the juxtaposition of pairs of pre- and postsynaptic fluorescent spots. Scale bar: $5\,\mu$m.

2 Supplementary Figure 2
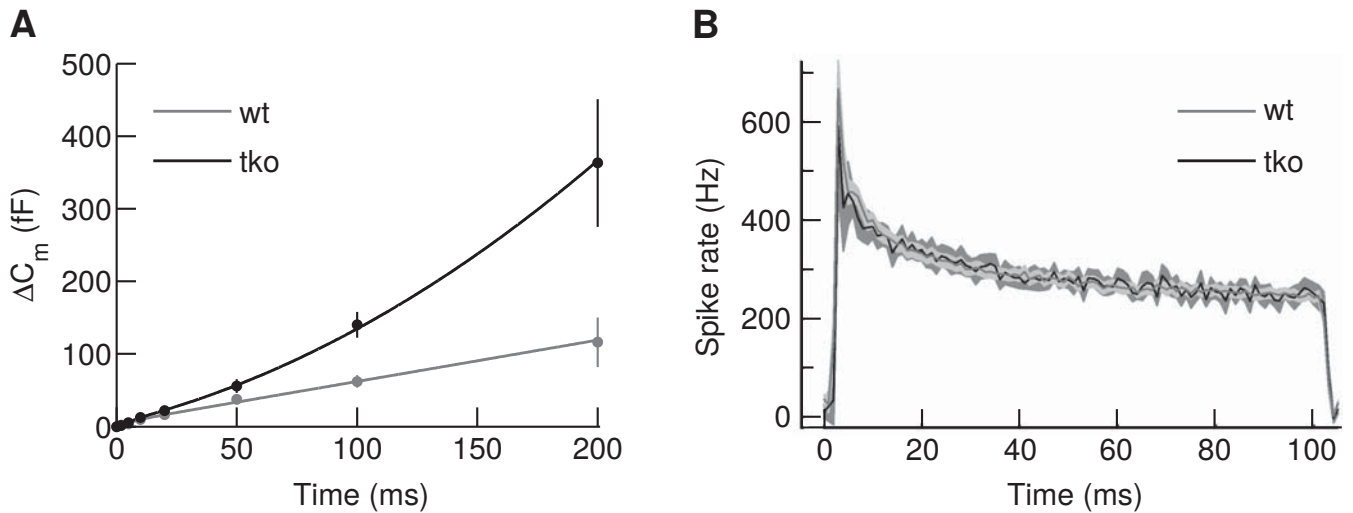
Figure S2: Cumulative exocytosis and SGN spike rates in response to prolonged stimuli in wt and tko mice. (A) Phenomenological fits to the experimental $\Delta C_m(t)$ data. The wt data were fitted by $\Delta C_m(t) = A' \cdot t + B' \cdot (1 - e^{-t/\tau})^n$ with (A', B', τ, n) treated as fitting parameters. The tko data were fitted by $\Delta C_m(t) = A' \cdot t + B' \cdot (1 - e^{-t/\tau})^n + t \cdot (a' \cdot t + b')$ with parameters (A', B', τ, n) set to the same values as for the wt data. Parameters a' and b' were found by fitting the difference between the experimental estimates of $\Delta C_m(t)$ from tko and wt IHCs by $t \cdot (a' \cdot t + b')$. Note that parameters (A, B, a, b) considered in Methods section "Conversion of neurotransmitter release events to spikes" correspond to the parameters (A', B', a', b') multiplied by $sc/(C_{sv} \cdot N_{syn})$. **(B)** Mean peristimulus time histogram ($\pm$s.e.m.), plotting the instantaneous spiking rate in 1-ms time bins over the time course of stimulation with 100 ms long tone bursts at the characteristic frequency of each SGN, 30 dB above threshold. The rates and the time course of adaptation were similar in tko (grey, n = 35) and wt SGNs (black, n = 8).

3 Supplementary Figure 3
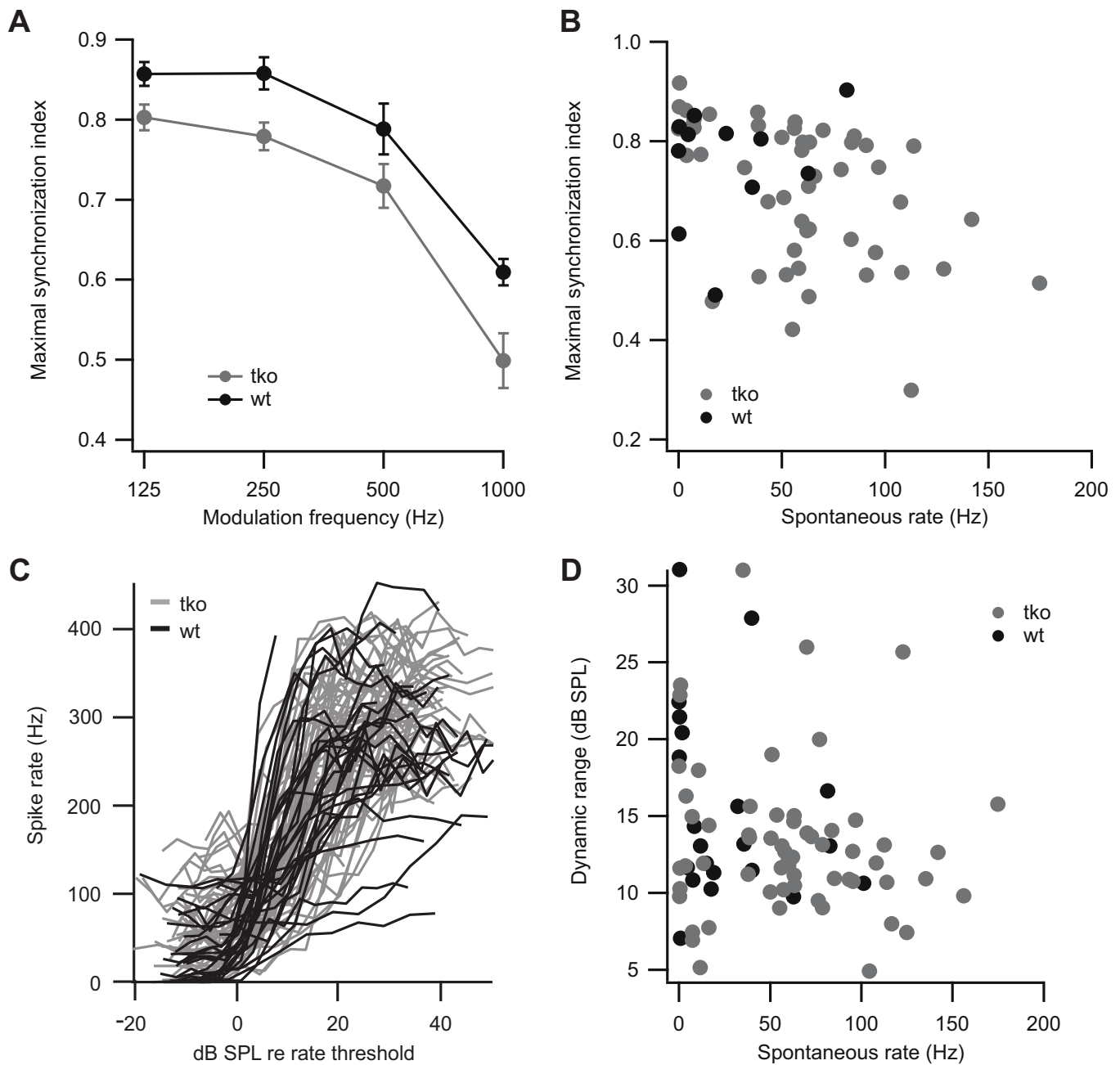
Figure S3: Precision of ongoing sound encoding is not affected by the absence of the three Ca^{2+} buffers. (A) Synchronization of SGN spiking to amplitude modulated transposed tones (formed by modulating a continuous sine wave at CF by a half-wave rectified sinusoid) was assessed at several stimulus intensities and modulation frequencies to determine the maximal synchronization index. **(B)** Maximal synchronization at 500 Hz was comparable between tko (grey, n = 49) and wt SGNs (black, n = 11) in spite of the tendency towards higher spontaneous rates in tko. **(C)** The steepness of spike rate increase with tone burst intensities was unchanged between tko (grey, n = 64) and wt (black, n = 22) SGNs. **(D)** The dynamic range of sound encoding (range of intensities over which the spike rate increases), which co-varies with spontaneous spiking rate, was similar among genotypes.

4   Supplementary Figure 4
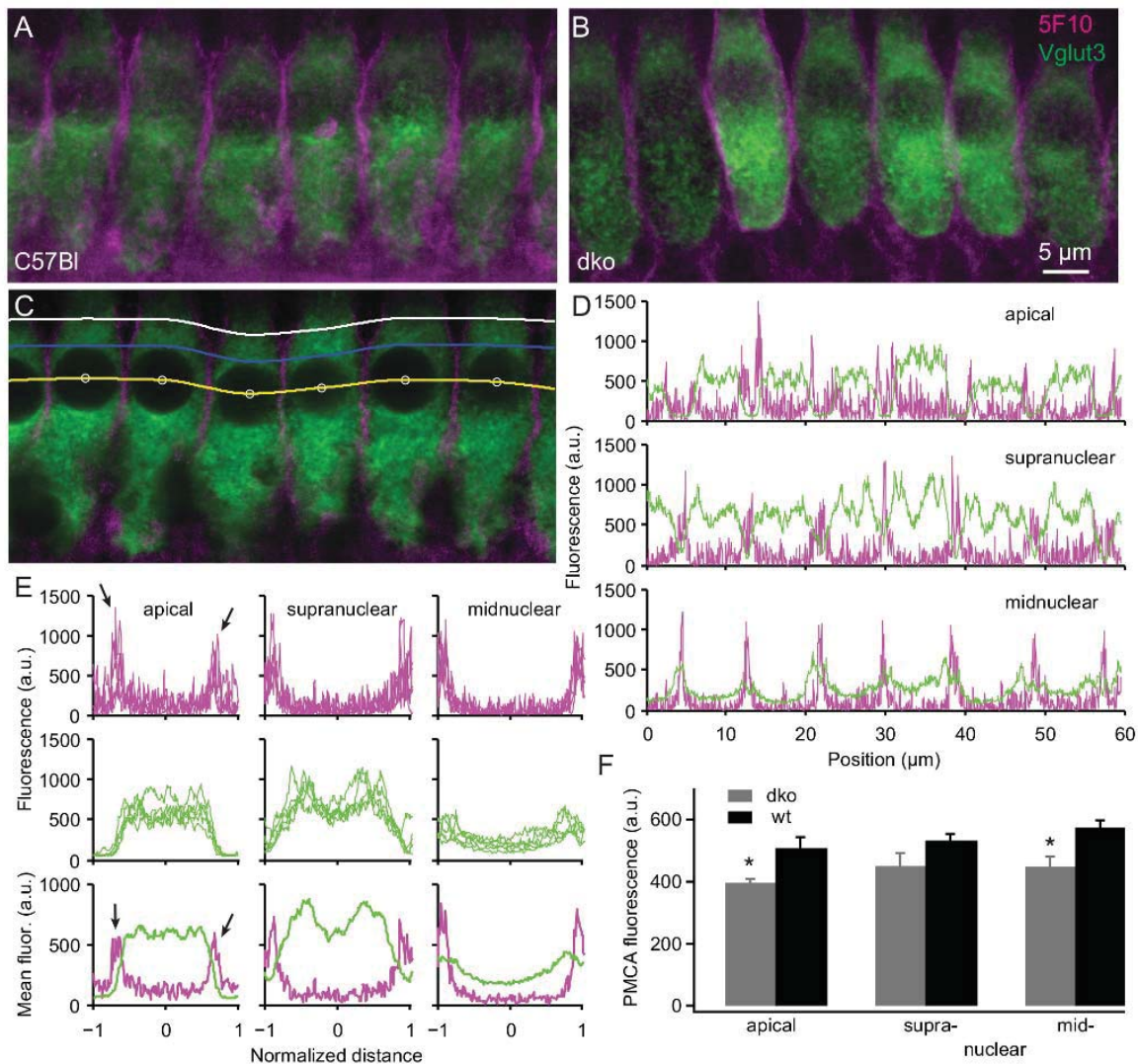
Figure S4: No compensatory upregulation of Ca^{2+} ATPases (PMCAs) in the plasma membrane of the double buffer knockout IHCs. (A-B) Maximal projections of confocal image stacks of a wt (A) and a dko (B) organ of Corti, stained for panPMCA (5F10, magenta) and an IHC marker Vglut3 (green). **(C-E)** An example demonstrating how the analysis of the PMCA fluorescence intensity was performed. **(C)** For each z-stack the immunofluorescence intensity was analyzed in the image plane with the best discernible nuclei (white circles denoting their centers). **(D)** Line profiles of Vglut3 (green) and PMCA (magenta) fluorescence intensity in the apical, supranuclear and midnuclear IHC region (white, blue and yellow line in panel C, respectively). Please note that we restricted our analysis to these cellular regions because the PMCA immunofluerescence was less well discernible in the basal parts of IHCs of either genotype (due to strong fluorescence in the surrounding tissue, e.g., the nerve fibers). **(E)** Fluorescence line profiles (from D) of separate cells aligned and superimposed (upper and middle panels). Lower panels show grand averages. Note a visible increase in the PMCA immunofluorescence at the cell borders (arrows). The average fluorescence intensity of these peaks was taken as the IHC PMCA fluorescence. **(F)** Histogram of average PMCA immunofluorescence in the three cellular regions. Note a significant decrease in the PMCA fluorescence in the plasma membranes of dko IHCs as compared to wt controls (Wilcoxon rank sum test, asterisks, $p < 0.05$).

5   Supplementary Figure 5
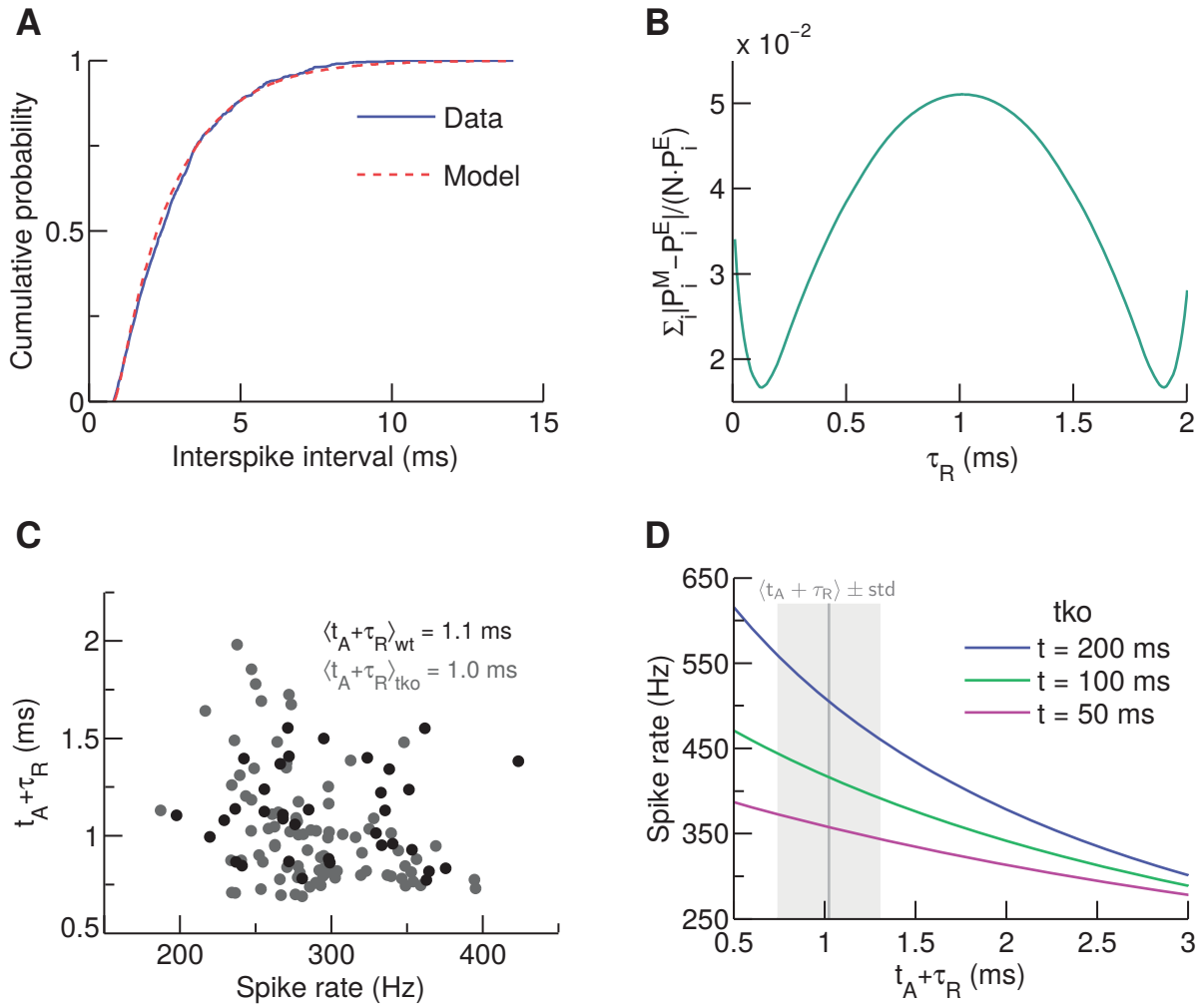
Figure S5: Estimation of the refractory periods and their impact on the discrepancy between the modeled spiking rates in wt and tko SGNs. (A) An exemplary cumulative distribution function of inter-spike intervals of SGNs. Blue solid line – experimental data (wt), red dashed line – the best model fit. τ_R estimated by this model is likely a minor overestimate because this model ignores the finding that spiking slightly deviates from Poissonian statistics for short inter-spike intervals (1). **(B)** Dependence of the discrepancy between the experimental data and the model from (A) on the fitting parameter τ_R. As it follows from the expression of $P^M(t)$ given in Methods, the discrepancy measure has two equivalent minimum points. We found, however, that, in most of the cases considered, the minimum point corresponding to the larger of the two values of τ_R resulted in release rate estimates considerably higher than those based on the capacitance increment recordings from wt IHCs. We thus selected the smaller of the two τ_R estimates, which always gave reasonable release rate estimates. In a few cases, when both estimates of τ_R resulted in reasonable release rates, the difference between them was small. **(C)** Scatter plot of the overall refractory period estimate $t_A + \tau_R$ vs. steady-state spike rate from different SGNs (wt n = 35, tko n = 87). **(D)** Spike rate dependence on $t_A + \tau_R$ of <u>modeled</u> tko SGNs. Different colors represent spike rate estimates at different time points after stimulus onset. The scaling coefficient sc was chosen in such a way that the modeled spike rate of wt SGNs, derived from the ΔC_m data from wt IHCs, equaled the experimental observation – 250 Hz – at a given $t_A + \tau_R$, 50 ms after stimulus onset. The sc values increased from 0.23 at $t_A + \tau_R = 0$ to 0.94 at $t_A + \tau_R = 3$ ms. The same sc values were then used for calculating spike rates of modelled tko SGNs based on ΔC_m data from tko IHCs.

6   Supplementary Figure 6
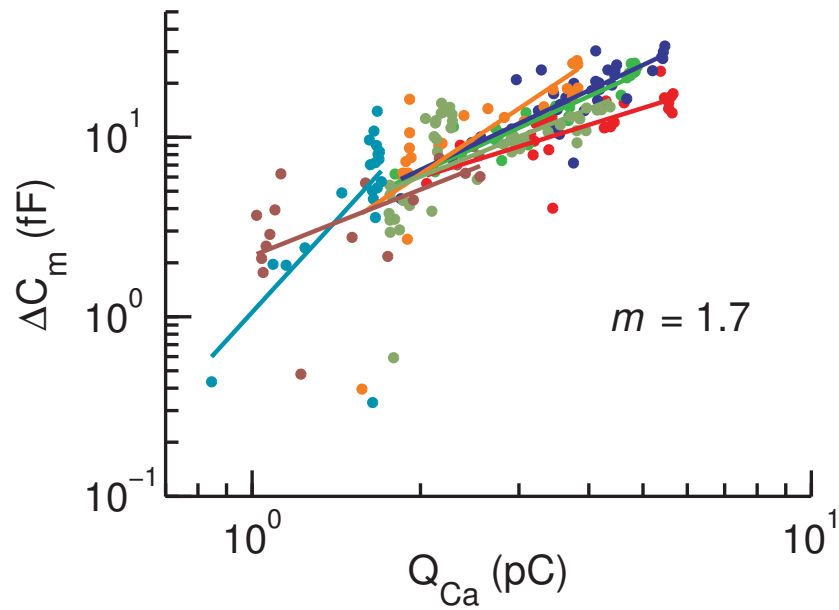
Figure S6: Apparent Ca²⁺ cooperativity of exocytosis in the operating range of Ca²⁺ influx at IHC synapses used for estimating the effective coupling distance R$_c$. Apparent Ca²⁺ cooperativities were estimated as the slope factors of linear fits (solid lines) of ΔC_m vs Q_{Ca} relations based on external [Ca²⁺]manipulation from seven mature IHCs (points) in log-log scale. Each color in the figure represents a particular cell. The data were taken from (2). Q_{Ca} interval used for the data fitting shown here was $\left[\max[Q_{Ca}]/2.5, \max[Q_{Ca}]\right]$ for each cell individually. The resulting Ca²⁺ cooperativity averaged over all cells, which we denote by m, was equal to 1.7. This value of m was used for estimating the effective coupling distance R_c, as described in Methods. To make sure that the estimate of m was not sensitive to small changes in the choice of the left boundary of the Q_{Ca} interval, we also considered values of the left boundary from $\max[Q_{Ca}]/1.1$ to $\max[Q_{Ca}]/3$. The resulting m values varied between 1.5 and 1.9.

7 Modeling of Ca^{2+} Dynamics (Including Supplementary Figures 7 − 11)

In this section, we provide additional information on modeling Ca^{2+} dynamics in the framework of a single Ca^{2+} source model formulated in Methods.

7.1 Reaction-Diffusion equations for [Ca^{2+}] dynamics

In the presence of one of the mobile exogenous buffers, BAPTA or EGTA, the dynamics of [Ca^{2+}] and concentrations of the mobile Ca^{2+} buffers following the onset of Ca^{2+} influx at t = 0 were modeled by the following closed system of reaction-diffusion equations:

$$\begin{cases} \partial_t[MgB_0] = k'_{on,0} \cdot [Mg^{2+}] \cdot \left([B_0]_T - [MgB_0] - [CaB_0]\right) - \left(k'_{off,0} - D_0 \cdot \Delta_r\right) \cdot [MgB_0] \\ \partial_t[Mg^{2+}] = \left(D_0 \cdot \Delta_r[MgB_0] - \partial_t[MgB_0]\right) + D' \cdot \Delta_r[Mg^{2+}] \\ \partial_t[CaB_0] = k_{on,0} \cdot [Ca^{2+}] \cdot \left([B_0]_T - [MgB_0] - [CaB_0]\right) - \left(k_{off,0} - D_0 \cdot \Delta_r\right) \cdot [CaB_0] \\ \partial_t[CaB_1] = k_{on,1} \cdot [Ca^{2+}] \cdot \left([B_1]_T - [CaB_1]\right) - \left(k_{off,1} - D_1 \cdot \Delta_r\right) \cdot [CaB_1] \\ \partial_t[Ca^{2+}] = \sum_{i=0}^{1} \left(D_i \cdot \Delta_r[CaB_i] - \partial_t[CaB_i]\right) + D \cdot \Delta_r[Ca^{2+}] \end{cases} .$$

Here, B$_0$ stands for ATP, and B$_1$ stands either for BAPTA or EGTA. k$_{on}$ and k$_{off}$ are Ca^{2+} binding and dissociation rates of a particular buffer. k$'_{on}$ and k$'_{off}$ are Mg^{2+} binding and dissociation rates of a particular buffer. D$_0$ and D$_1$ are the diffusion coefficients of B$_0$ and B$_1$ respectively. We assumed that the diffusion coefficients of Ca^{2+}- or Mg^{2+}-bound buffer molecules are equal to the the diffusion coefficients of the corresponding free buffer molecules. D and D$'$ stand for the diffusion coefficients of Ca^{2+} and Mg^{2+} respectively. $\Delta_r \equiv \frac{1}{r^2}\frac{\partial}{\partial r}\left(r^2\frac{\partial}{\partial r}\ldots\right)$ is the radial component of the Laplace operator. Note that concentrations of free buffer molecules at any point of space and time were determined by the difference between the total and Mg^{2+}-bound and/or Ca^{2+}-bound buffer concentrations. The total buffer concentrations were constant in space and time. This applies whenever Ca^{2+}-bound and Mg^{2+}-bound molecules have the same diffusion coefficients as the corresponding free buffer molecules, the total buffer concentrations are distributed uniformly within the simulation volume at t = 0 (as it was assumed in our model), and boundary conditions formulated in the next paragraph are used (see (3)).

In the case of the original model, the boundary conditions read as

$$\left.\frac{\partial[Ca^{2+}]}{\partial r}\right|_{r=r_0} = -\frac{i_{Ca}}{4\cdot\pi\cdot D\cdot F\cdot r_0^2}\cdot H(t), \quad \left.\frac{\partial[X]}{\partial r}\right|_{r=r_0} = 0, \quad \left.\frac{\partial[Ca^{2+}]}{\partial r}\right|_{r=R} = 0, \quad \left.\frac{\partial[X]}{\partial r}\right|_{r=R} = 0,$$

here, X – Mg^{2+} or one of the Ca^{2+} or Mg^{2+} bound buffer molecules, F – Faraday constant, $H(t)$ – Heaviside step function. In the case of the modified version of the original model considered in section 7.6, the boundary conditions read as

$$\left.\frac{\partial[Ca^{2+}]}{\partial r}\right|_{r=r_0} = -\frac{i_{Ca}}{4\cdot\pi\cdot D\cdot F\cdot r_0^2}\cdot H(t), \quad \left.\frac{\partial[X]}{\partial r}\right|_{r=r_0} = 0, \quad [Ca^{2+}]\big|_{r=R} = [Ca^{2+}]_0, \quad [X]\big|_{r=R} = [X]_0.$$

Here, [Ca^{2+}]$_0$ and [X]$_0$ are concentrations of Ca^{2+} and other ions and molecules in the simulation volume before onset of Ca^{2+} influx. Noteworthy, due to the symmetry, a hemispherical source model with

reflecting boundary at the base of the hemispherical simulation volume is equivalent to a spherical source model, with identical Ca^{2+} flux density, embedded in a spherical simulation volume.

In the presence of mobile endogenous Ca^{2+} buffers, $[Ca^{2+}]$ was determined by the following set of equations (or a particular subset of this set, when not all of the physiological endogenous buffers were considered together):

$$
\begin{cases}
\partial_t[MgB_0] = k'_{on,0} \cdot [Mg^{2+}] \cdot \left([B_0]_T - [MgB_0] - [CaB_0]\right) - \left(k'_{off,0} - D_0 \cdot \Delta_r\right) \cdot [MgB_0] \\
\partial_t[MgB_1] = k'_{on,1} \cdot [Mg^{2+}] \cdot \left(2 \cdot [B_1]_T - [MgB_1] - [CaB_1]\right) - \left(k'_{off,1} - D_1 \cdot \Delta_r\right) \cdot [MgB_1] \\
\partial_t[Mg^{2+}] = \sum_{i=0}^{1} \left(D_i \cdot \Delta_r[MgB_i] - \partial_t[MgB_i]\right) + D' \cdot \Delta_r[Mg^{2+}] \\
\partial_t[CaB_0] = k_{on,0} \cdot [Ca^{2+}] \cdot \left([B_0]_T - [MgB_0] - [CaB_0]\right) - \left(k_{off,0} - D_0 \cdot \Delta_r\right) \cdot [CaB_0] \\
\partial_t[CaB_1] = k_{on,1} \cdot [Ca^{2+}] \cdot \left(2 \cdot [B_1]_T - [MgB_1] - [CaB_1]\right) - \left(k_{off,1} - D_1 \cdot \Delta_r\right) \cdot [CaB_1] \\
\partial_t[CaB_2] = k_{on,2} \cdot [Ca^{2+}] \cdot \left(4 \cdot [B_2]_T - [CaB_2]\right) - \left(k_{off,2} - D_2 \cdot \Delta_r\right) \cdot [CaB_2] \\
\partial_t[CaB_3] = k_{on,3} \cdot [Ca^{2+}] \cdot \left([B_3]_T - [CaB_3]\right) - \left(k_{off,3} - D_3 \cdot \Delta_r\right) \cdot [CaB_3] \\
\partial_t[CaB_4] = k^T_{on,4} \cdot [Ca^{2+}] \cdot \left(2 \cdot [B_4]_T - [CaB_4] - [Ca_2B_4]\right) - \left(k^T_{off,4} - D_4 \cdot \Delta_r\right) \cdot [CaB_4] \\
\partial_t[Ca_2B_4] = k^R_{on,4} \cdot [Ca^{2+}] \cdot [CaB_4] - \left(k^R_{off,4} - D_4 \cdot \Delta_r\right) \cdot [Ca_2B_4] \\
\partial_t[Ca^{2+}] = \sum_{i=0}^{3} \left(D_i \cdot \Delta_r[CaB_i] - \partial_t[CaB_i]\right) + D_i \cdot \Delta_r[Ca_2B_4] - \partial_t[Ca_2B_4] + D \cdot \Delta_r[Ca^{2+}]
\end{cases}
.
$$

Here, B_0 stands for ATP, B_1 – parvalbumin-α (PV), B_2 – calbindin-D28k (CB), B_3 – non-cooperative binding site of calretinin ($CR_{non.coop.}$), B_4 – cooperative binding site of calretinin with no Ca^{2+}-bound ($CR_{coop.}$), CaB_4 – cooperative binding site of calretinin with one Ca^{2+}-bound ($CaCR_{coop.}$), Ca_2B_4 – cooperative binding site of calretinin with two Ca^{2+} bound. The following Ca^{2+} and Mg^{2+} binding and unbinding rates were used for simulations:

· BAPTA – $k_{on} = 400\,mM^{-1} \cdot ms^{-1}$, $k_{off} = 0.088\,ms^{-1}$, (3).

· EGTA – $k_{on} = 10\,mM^{-1} \cdot ms^{-1}$, $k_{off} = 0.0007\,ms^{-1}$, (4).

· ATP – $k_{on} = 1000\,mM^{-1} \cdot ms^{-1}$, $k_{off} = 90\,ms^{-1}$, (5).

· ATP (Mg^{2+}) – $k_{on} = 10\,mM^{-1} \cdot ms^{-1}$, $k_{off} = 0.45\,ms^{-1}$, (5).

· PV – $k_{on} = 103\,mM^{-1} \cdot ms^{-1}$, $k_{off} = 0.00095\,ms^{-1}$, (6).

· PV (Mg^{2+}) – $k_{on} = 0.8\,mM^{-1} \cdot ms^{-1}$, $k_{off} = 0.025\,ms^{-1}$, (6).

· CB – $k_{on} = 75\,mM^{-1} \cdot ms^{-1}$, $k_{off} = 0.0295\,ms^{-1}$, (7).

· $CR_{non.coop.}$ – $k_{on} = 7.3\,mM^{-1} \cdot ms^{-1}$, $k_{off} = 0.252\,ms^{-1}$, (8).

· $CR_{coop.}$ – $k_{on} = 1.8\,mM^{-1} \cdot ms^{-1}$, $k_{off} = 0.053\,ms^{-1}$, (8).

· $CaCR_{coop.}$ – $k_{on} = 310\,mM^{-1} \cdot ms^{-1}$, $k_{off} = 0.02\,ms^{-1}$, (8).

The diffusion coefficients were set to $0.22\,\mu m^2 \cdot ms^{-1}$ for Ca^{2+}, Mg^{2+}, ATP, BAPTA, and EGTA (3), to $0.02\,\mu m^2 \cdot ms^{-1}$ for PV and CR (8,9), and to $0.043\,\mu m^2 \cdot ms^{-1}$ for CB (10). The resting Ca^{2+} concentration, $[Ca^{2+}](r, t = 0)$, was set to $50\,nM$ (11).

The above systems of partial differential equations were solved numerically in MATLAB using built-in PDE solver *pdepe*.
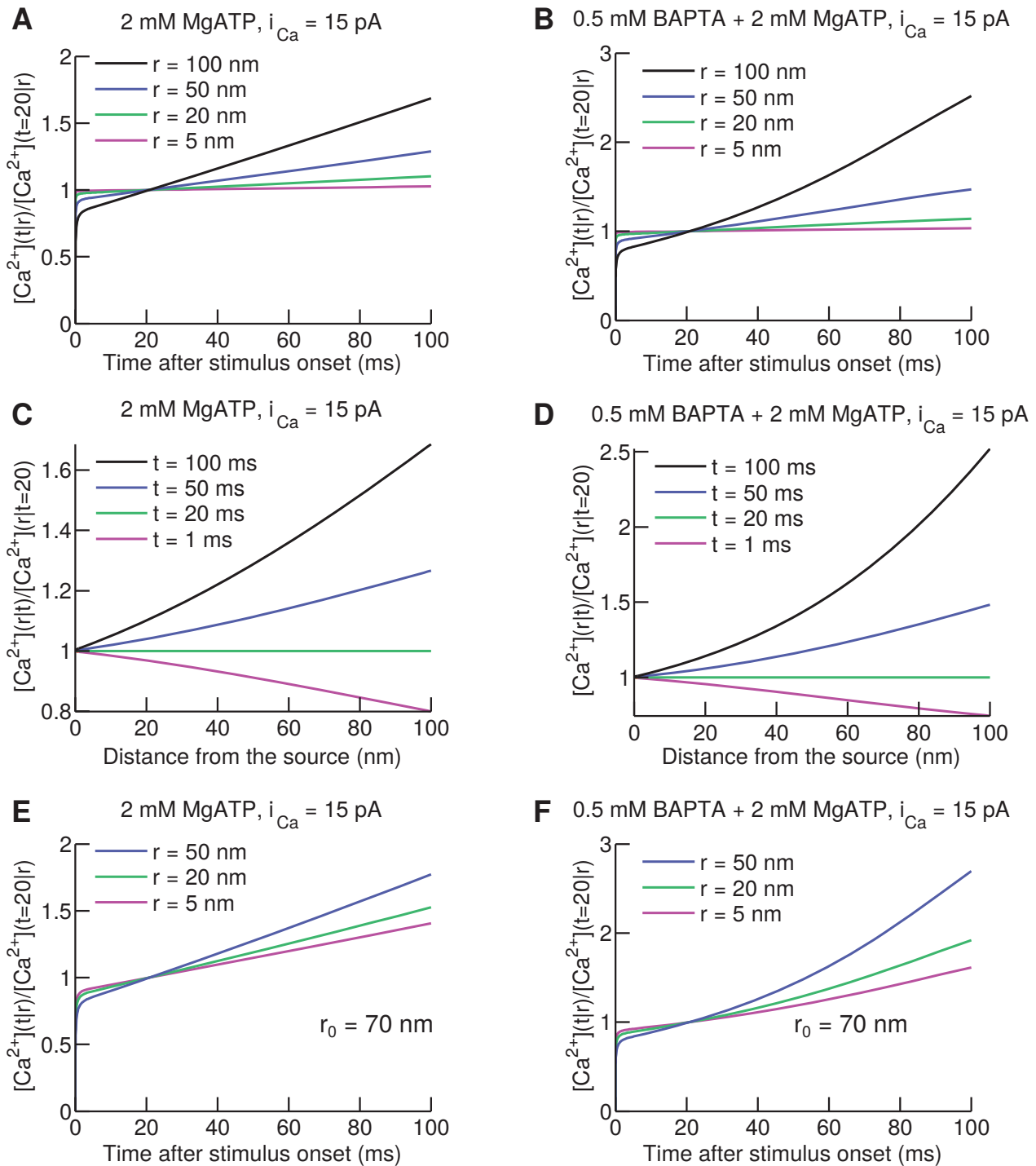
7.2 Temporal evolution of [Ca^{2+}]

Fig. **S7A**-**B** show time evolution of normalized [Ca^{2+}] after onset of stimulus[1] at distances up to 100 nm from the edge of a $r_0 = 1$ nm hemispherical source ($i_{Ca} = 15$ pA) embedded in a hemispherical simulation volume of 2 μm radius with reflecting boundary conditions. In all plots shown, [Ca^{2+}](r, t) was normalized to [Ca^{2+}]$(r, t = 20$ ms). Panels on the left in **Fig**. **S7** were obtained for the simulation volume filled with 2 mM MgATP, while panels on the right correspond to the simulation volume filled with 2 mM MgATP + 0.5 mM BAPTA. It follows from the panels (A) and (B) that the temporal profiles of [Ca^{2+}] were approximately characterized by two time scales. The initial time scale corresponded to the quasi-equilibration of Ca^{2+} diffusion and reaction with the buffer molecules. The later, much slower time scale corresponded to accumulation of Ca^{2+} and the accompanying increase in the fraction of Ca^{2+}-bound buffer molecules due to the prolonged Ca^{2+} influx. As can be seen in the plots, [Ca^{2+}] at distances up to 100 nm away from the source stayed rather constant during the first 20 ms after the initial build-up. This was especially true for points located closer to the source. At t = 100 ms, however, the accumulation of Ca^{2+} was considerable at the greater distances, in relative terms. This is seen better in **Fig**. **S7C**-**D**, where normalized spatial [Ca^{2+}] profiles are shown for selected time points[2].

In the case of a real presynaptic active zone, a 15 pA influx of Ca^{2+} ions (a finding of our present work) is spread over an area of the cellular membrane which is considerably larger than the surface area of a $r_0 = 1$ nm hemispherical source. Thus, the absolute levels of [Ca^{2+}] at small distances from the source were overestimated in our model[3]. This overestimation could result in a decreased effect of the accumulated bulk Ca^{2+} on [Ca^{2+}] in the proximity of the source during prolonged depolarizations. To examine this, we repeated the calculations with a $r_0 = 70$ nm radius hemispherical source. The surface area of this larger hemisphere approximately matched the area of the presynaptic density at IHC synapses (420×80 nm^2, (2)). We found that, although the influence of the accumulated Ca^{2+} on [Ca^{2+}] was slightly stronger in this case, the conclusions drawn from the model with $r_0 = 1$ nm radius hemispherical source did not change – compare plots in **Fig**. **S7E**-**F** with the corresponding plots in **Fig**. **S7A**-**B**. Note that, when a point of interest is close to the edge of the Ca^{2+} source, the average distance between the point of interest and effective Ca^{2+} point sources which are spread on the surface of the hemisphere is considerably higher in the case of the $r_0 = 70$ nm radius hemisphere than the $r_0 = 1$ nm radius hemisphere. This is one of the reasons why the influence of the accumulated Ca^{2+} on [Ca^{2+}] was slightly stronger for the $r_0 = 70$ nm source than for the $r_0 = 1$ nm source. The same fact explains why initial phases of the [Ca^{2+}] temporal profiles were associated with a slightly slower time scale in the case of the larger, $r_0 = 70$ nm, hemisphere.

---

[1] "Onset of stimulus" and "onset of Ca^{2+} influx" are used as synonyms in sections 6.1 - 6.6.

[2] Similar effects were also found when 2 mM MgATP + 1 mM BAPTA or 2 mM MgATP + $(0.5 - 1)$ mM EGTA were used as Ca^{2+} buffers. Naturally, the effect of Ca^{2+} accumulation on [Ca^{2+}] is less pronounced for higher concentrations of exogenous Ca^{2+} buffers and/or smaller i_{Ca} levels.

[3] Note that, in this work, estimations of concentrations of the endogenous buffers or the coupling distance between presynaptic Ca^{2+} channels and Ca^{2+} sensors of exocytosis were based on the ratios of [Ca^{2+}] estimated in different Ca^{2+} buffering conditions, not the absolute levels of [Ca^{2+}].

Figure S7: Temporal evolution of [Ca²⁺]. **(A)** Ratios of temporal $[Ca^{2+}]$ profiles at certain distances from the source, $[Ca^{2+}](t|r)/[Ca^{2+}](t=20|r)$, based on $i_{Ca} = 15$ pA Ca^{2+} influx through a $r_0 = 1$ nm hemispherical source with the simulation volume filled with 2 mM MgATP. **(B)** The same as (A), but with the simulation volume filled with 0.5 mM BAPTA and 2 mM MgATP. **(C)** Ratios of spatial Ca^{2+} profiles at fixed times, $[Ca^{2+}](r|t)/[Ca^{2+}](r|t=20)$, corresponding to the temporal profiles shown in (A). **(D)** The same as (C), but with the simulation volume filled with 0.5 mM BAPTA and 2 mM MgATP. **(E)** Temporal profiles of $[Ca^{2+}]$ based on $i_{Ca} = 15$ pA Ca^{2+} influx through a $r_0 = 70$ nm hemispherical source with simulation volume filled with 2 mM MgATP. **(F)** The same as (E), but with the simulation volume filled with 0.5 mM BAPTA and 2 mM MgATP.

11

7.3 Extent of Ca²⁺ buffer depletion due to Ca²⁺ influx

To find the value of i_{Ca} which results in a similar extent of Ca²⁺ buffer depletion for a $r_0 = 1$ nm hemispherical source as at the presynaptic active zone, we varied levels of i_{Ca} and compared the resulting Ca²⁺ buffer concentrations with the ones corresponding to a $r_0 = 70$ nm source[4] with $i_{Ca} = 15$ pA. **Fig. S8** shows the ratios of increments of the Ca²⁺-bound buffer concentrations due to onset of Ca²⁺ influx through the $r_0 = 1$ nm and $r_0 = 70$ nm hemispherical sources as functions of the distance from the edge of the sources. In the case shown here, Ca²⁺ influx was set to 15 pA for the $r_0 = 70$ nm source and 7 pA for the $r_0 = 1$ nm source. The concentrations were estimated 20 ms after onset of Ca²⁺ influx. The simulation volume was a hemisphere of $2\,\mu$m radius with reflecting boundary conditions. The total concentrations of exogenous buffers BAPTA and EGTA, each of them considered separately, were set to either 0.5 mM or 1 mM. Moreover, in all considered cases, a total of 2 mM ATP was included. As can be seen from the plots, the ratios of the amounts of depleted buffers, BAPTA + ATP or EGTA + ATP, were around 1 or higher for the distances considered. This indicates that the $r_0 = 1$ nm source with $i_{Ca} = 7$ pA resulted in a similar extent of Ca²⁺ buffer depletion as the $r_0 = 70$ nm source with $i_{Ca} = 15$ pA over distances 0 to 50 nm from the Ca²⁺ source.
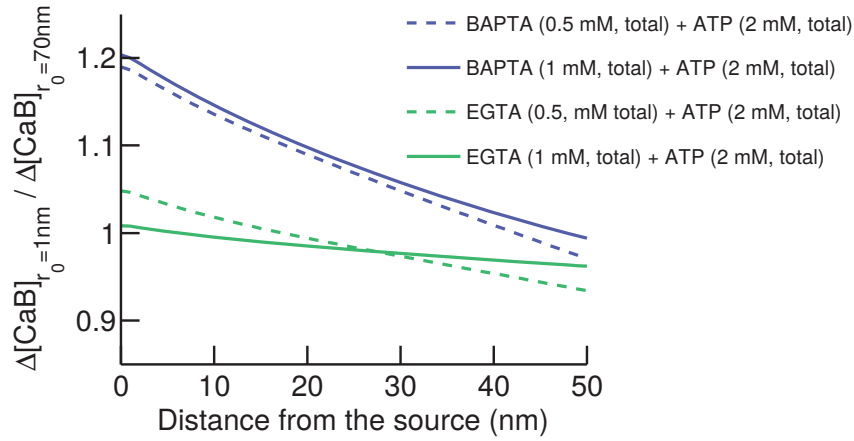
Figure S8: **Ratios between increased Ca²⁺-bound buffer concentrations due to Ca²⁺ influx for hemispherical Ca²⁺ sources with $r_0 = 1$ nm, $i_{Ca} = 7$ pA, and $r_0 = 70$ nm, $i_{Ca} = 15$ pA as functions of the distance from the edge of the sources**.

7.4 Influence of the partial buffer depletion on the [Ca²⁺] vs. i_{Ca} relation

It was assumed in the model considered in Results that integrated exocytosis, ΔC_m follows [Ca²⁺] at the sensor of exocytosis according to a power law relation. However, [Ca²⁺] at the sensor of exocytosis is not an experimentally accessible quantity currently. Thus, in order to determine the exponent parameter of the relation between ΔC_m and [Ca²⁺] at the sensor of exocytosis, we have to employ the experimentally accessible relation between the integrated release and integrated Ca²⁺ influx, Q_{Ca}: $\Delta C_m \sim (Q_{Ca})^m$ (see section 6). We show below that $Q_{Ca} \sim [\text{Ca}^{2+}]^q$. Thus, $\Delta C_m \sim [\text{Ca}^{2+}]^{m \cdot q}$.

Due to nonlinearities inherent to the dynamics of Ca²⁺ and buffer concentrations, the dependence of [Ca²⁺](t, r) on the Ca²⁺ influx level i_{Ca} is nonlinear in general. We simulated the dependence of

---

[4]Which has the surface area similar in extent to that of a real IHC presynaptic density as explained in section 7.2.

$[\mathrm{Ca}^{2+}](t, r)$ on i_{Ca} to quantitatively check how much this relation deviates from the linear approximation. It turned out that, for all the considered buffering conditions, the relation was well approximated by $[\mathrm{Ca}^{2+}](r) \sim i_{Ca}^{1/q(r)}$ at distances of 0 to 100 nm from the source. **Fig**. **S9B-D** show the $[\mathrm{Ca}^{2+}]$ vs. i_{Ca} relations at distances of 0, 10, 25, 50, 100 nm away from the source, at t = 20 ms for three different Ca^{2+} buffer sets: 2 mM MgATP, 0.5 mM BAPTA + 2 mM MgATP, 0.5 mM EGTA + 2 mM MgATP. Black solid lines represent the simulated data, while magenta dashed lines represent the best fits of the form $[\mathrm{Ca}^{2+}](r) = k(r) \cdot i_{Ca}^{1/q(r)}$. i_{Ca} values ranging from 0.3 pA to 7 pA were considered. The radius of the hemispherical source was set to 1 nm. The radius of the simulation volume hemisphere was 2 μm. The boundary was reflective for all ions and molecules considered. **Fig**. **S9A** shows the dependence of the exponent q on the distance from the source, r, for the three aforementioned Ca^{2+} buffering conditions. q values were only slightly smaller than 1, thus the $[\mathrm{Ca}^{2+}]$ vs. i_{Ca} relation was only slightly supralinear. When concentrations of BAPTA and EGTA were increased from 0.5 mM to 1 mM, $q(r)$ shifted slightly towards 1.
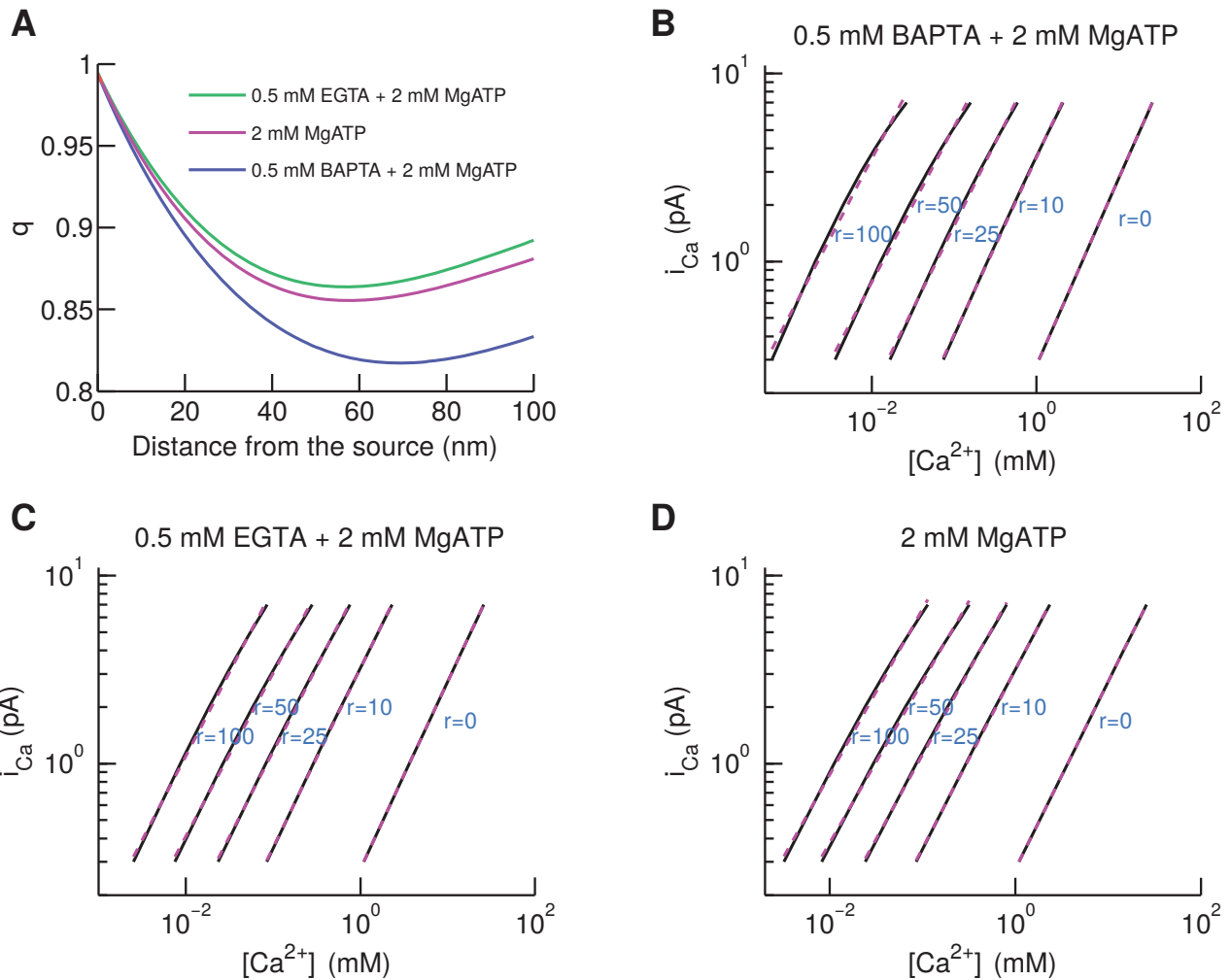
Figure S9: Influence of the partial buffer depletion on $[\mathrm{Ca}^{2+}]$ vs. i_{Ca} relation. (A) Dependence of the exponent q corresponding to the best fits of simulated i_{Ca} vs. $[\mathrm{Ca}^{2+}]$ relations by $i_{Ca} = k \cdot [\mathrm{Ca}^{2+}]^{q}$ on the distance from a $\mathrm{r_0} = 1$ nm hemispherical Ca^{2+} source with $i_{\mathrm{Ca}} = 7$ pA. **(B-D)** Simulated i_{Ca} vs. $[\mathrm{Ca}^{2+}]$ relations (black solid lines) and the optimal fits of the form $i_{Ca} = k \cdot [\mathrm{Ca}^{2+}]^{q}$ (dashed magenta lines) with different contents of Ca^{2+} buffers.

Note that $Q_{Ca} = t \cdot i_{Ca}$ for constant i_{Ca}, where t is the time passed since stimulus onset. Thus, $[Ca^{2+}](r) = (k(r)/t^{1/q(r)}) \cdot Q_{Ca}^{1/q(r)}$. To take into account the effect of partial buffer depletion on the estimate of the effective coupling distance between presynaptic Ca^{2+} channels and Ca^{2+} sensors of exocytosis for $i_{Ca} = 7$ pA, we used $q(r)$ profiles corresponding to 0.5 mM BAPTA +2 mM MgATP buffering conditions, which roughly approximates the natural Ca^{2+} buffering conditions in IHC as shown in our present work. We used $q(r) \equiv 1$ for estimating the coupling distance for weak $[Ca^{2+}]$ influx ($i_{Ca} = 0.3$ pA).

7.5 Effect of accumulated bulk Ca^{2+} during prolonged stimulation on the model predictions of concentrations of the endogenous Ca^{2+} buffers

The upper bounds for concentrations of the endogenous Ca^{2+} buffers shown in **Fig**. **9C** were estimated by probing $[Ca^{2+}]$ at t = 100 ms after stimulus onset. It was shown in section 7.2 (see **Fig**. **S7A-B**) that the effect of the accumulated Ca^{2+} on $[Ca^{2+}]$ increased with time after stimulus onset from negligible at t = 20 ms to significant at t = 100 ms. This could affect the estimates of the upper bounds for the concentrations of the endogenous Ca^{2+} buffers, which were determined by matching the spatial $[Ca^{2+}]$ profiles at t = 100 ms (see Results and **Fig**. **9C**). To test this, we re-estimated the upper bounds for the concentrations of the endogenous Ca^{2+} buffers by probing spatial profiles of $[Ca^{2+}]$ at times between 20 ms and 100 ms after stimulus onset. Solid lines in **Fig**. **S10** show dependencies of the estimates of Ca^{2+}-binding site concentrations of the endogenous buffers on the time when $[Ca^{2+}]$ was probed. The estimates of Ca^{2+}-binding site concentrations for calbindin-D28k and parvalbumin-α decreased only slightly when comparing values obtained at t = 20 ms to t = 100 ms: from 6.4 mM to 5.2 mM for calbindin-D28k and from 5.0 mM to 4.2 mM for parvalbumin-α. The difference was more significant for calretinin – the estimate of the Ca^{2+}-binding site concentration decreased from 21.0 mM at t = 20 ms to 13.8 mM t = 100 ms. The reason why calretinin was so sensitive to the accumulated Ca^{2+} is that it has highly cooperative Ca^{2+} binding sites, with the first binding step being much slower than the second one.
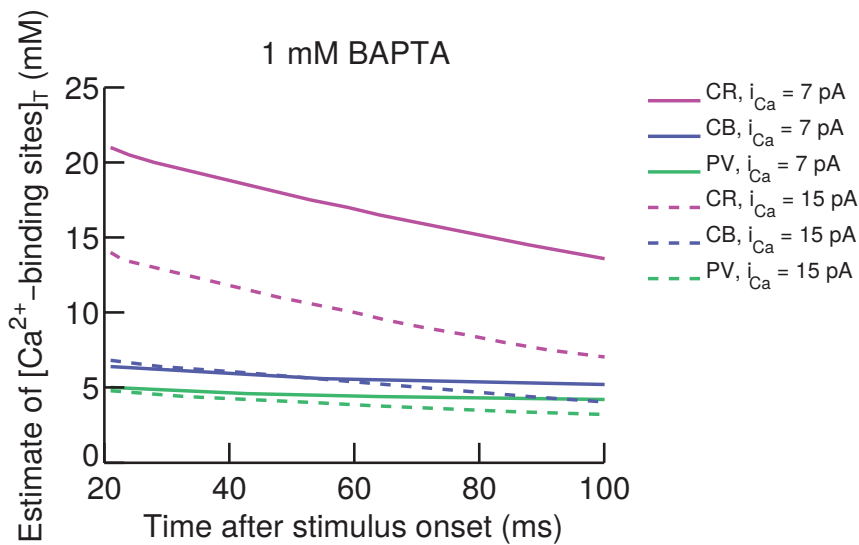
Figure S10: **Estimation of concentrations of the endogenous buffer Ca^{2+}-binding sites equivalent to 1 mM BAPTA based on $[Ca^{2+}]$ probed at different moments after stimulus onset.**

Dashed lines in **Fig**. **S10** show dependencies of the estimates of the Ca^{2+}-binding site concentrations on the moment when $[Ca^{2+}]$ was probed after onset of i_{Ca} of 15 pA. The results were essentially the same as with $i_{Ca} = 7$ pA for calbindin-D28k and parvalbumin-α. However, the concentration estimates were decreased by ~ 7 mM for calretinin.

7.6 Influence of the type of boundary conditions on the estimates of the endogenous buffer concentrations and the coupling distance R_c

The original model of $[Ca^{2+}]$ dynamics presented in this work assumed a hemispherical simulation volume with $2 \, \mu$m radius. The boundaries of the simulation volume were set to be reflective to all molecules and ions considered. The choice of the radius of the simulation volume was based on the finding that the presynaptic active zones of inner hair cells are separated by $2 \, \mu$m on average (12). The reflecting boundary condition set at the hemispherical boundary of the simulation volume was meant to effectively take into account accumulation of Ca^{2+} due to Ca^{2+} channels from the synapse under consideration as well as Ca^{2+} channels from neighboring synapses. On the other hand, such a boundary condition could lead to an overestimation of the $[Ca^{2+}]$ because it does not take into account removal of Ca^{2+} ions and Ca^{2+}-bound buffer molecules from the neighborhood of the presynaptic site due to exchange of the molecules with the large non-synaptic part of the IHC volume. Indeed, 12 hemispheres with $2 \, \mu$m radius correspond to only one percent of hair cell volume ($2.2 \cdot 10^{-15}$ m^{-3}, (13)) on average. The purely reflective boundary at the base of the simulation volume ignores Ca^{2+} removal by Ca^{2+} pumps. To check how the choice of the boundary conditions affected our estimates of the endogenous buffer concentrations and the coupling distance between presynaptic Ca^{2+} channels and Ca^{2+} sensors of exocytosis, we performed equivalent simulations with different boundary conditions. Specifically, we fixed concentrations of all considered molecules and ions at the hemispherical boundary of the simulation volume to their resting levels, i.e., levels before the onset of Ca^{2+} influx. The base of the hemisphere was chosen to be reflecting as in the original model. The radius of the hemispherical simulation volume, R, was set to either $2 \, \mu$m or $4 \, \mu$m. Such boundary conditions can be treated as overestimating the intensity of Ca^{2+} removal from the neighborhood of the presynaptic active zones.

Fig. **S11A**-B show plots of ratios $[Ca^{2+}](r|t)/[Ca^{2+}]^*(r| + \infty)$ at selected times. Here, $[Ca^{2+}](r|t)$ stands for $[Ca^{2+}]$ at the distance r from the source at moment t after stimulus onset, estimated by using the original model with reflecting boundary conditions. $[Ca^{2+}]^*(r| + \infty)$ stands for the steady state $[Ca^{2+}]$ at the distance r from the source, estimated by using the "resting-level" boundary conditions introduced in the previous paragraph (see also section 7.1). Solid (dashed) lines correspond to $[Ca^{2+}]^*$ estimated using a R = $2 \, \mu$m (R = $4 \, \mu$m) simulation volume. **Fig**. **S11A** corresponds to 2 mM MgATP, **Fig**. **S11B** corresponds to 0.5 mM BAPTA + 2 mM MgATP. These profiles are quantitatively similar to the spatial profiles shown in **Fig**. **S7C-D**, where $[Ca^{2+}](r|t = 20)$ was used for scaling. The differences between the results corresponding to R = $2 \, \mu$m and R = $4 \, \mu$m simulation volumes were negligible (compare solid and dashed lines in **Fig**. **S11A**-B). This similarity can be explained by the fact that, in the first 20 ms after onset of Ca^{2+} influx, the processes of Ca^{2+} diffusion and binding to the buffers were confined to a small volume, which was far away from the hemispherical surface of the simulation volume. These results suggest that the estimate of R_c is rather insensitive to the precise choice of boundary conditions, given

that the radius of the simulation volume, R, is $\geq 2\,\mu$m. This idea is corroborated by the observation that dependencies of the discrepancy measure z on the effective distance between the Ca^{2+} source and Ca^{2+} sensors of exocytosis shown in **Fig. S11C** were strikingly similar to the equivalent plots shown in **Fig. 9B**. Estimates of the effective concentrations of the endogenous buffer Ca^{2+} binding sites did not strongly depend on which of the boundary conditions were used either (compare **Fig. S11D** with **Fig. 9C**), except the upper bound estimate for calretinin. The latter was larger by $\sim 50\%$ in the case of the resting-level boundary conditions because of the Ca^{2+} binding cooperativity of calretinin.
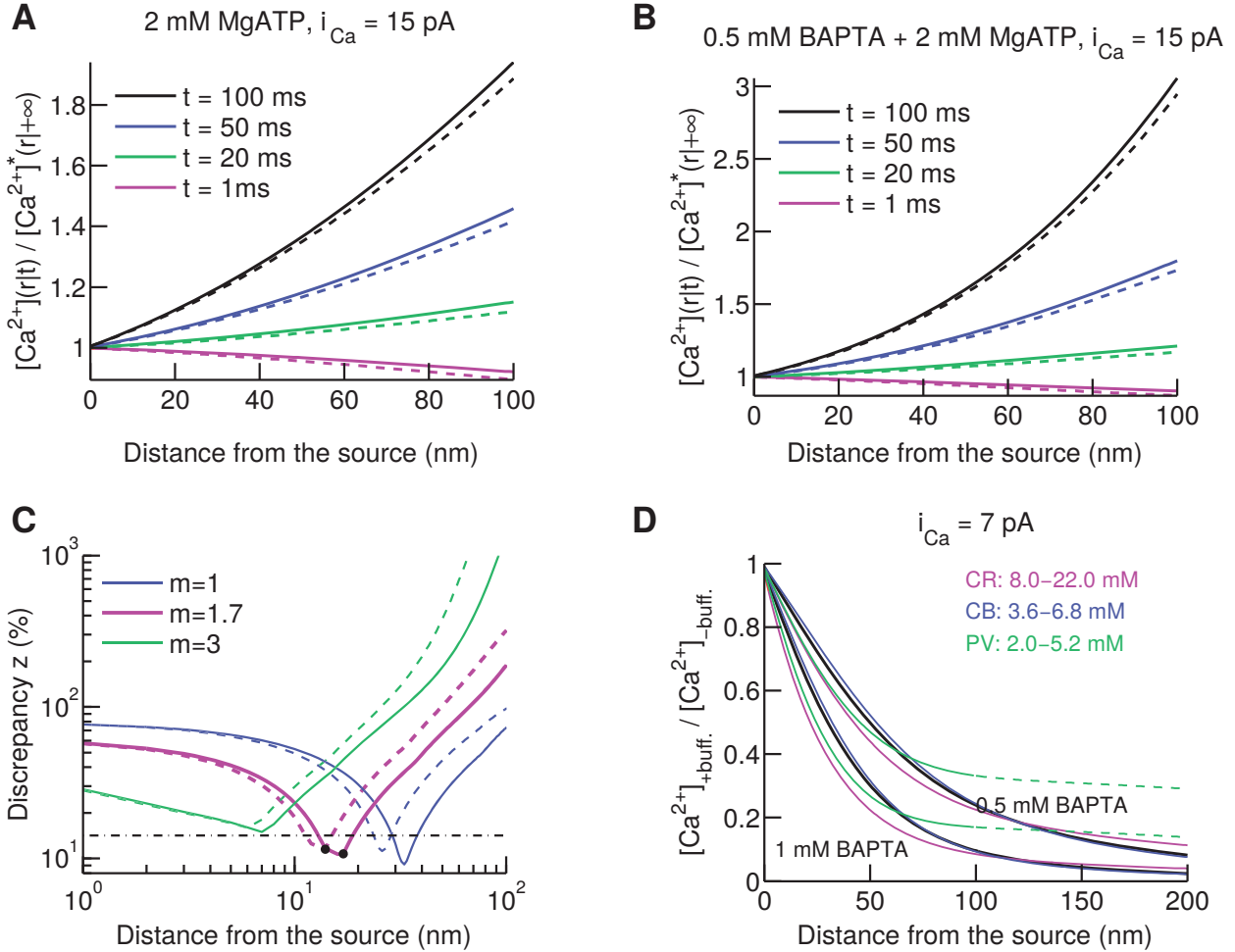
Figure S11: Results based on the simulations with boundary conditions that fix concentrations of all molecular species to the resting levels at the hemispherical surface of the simulation volume. **(A-B)** Spatial profiles of ratios $[\text{Ca}^{2+}](r|t)/[\text{Ca}^{2+}]^*(r|+\infty)$ at selected times. Solid (dashed) lines correspond to $[\text{Ca}^{2+}]^*(r|+\infty)$ estimated with the radius of the simulation volume equal to R $= 2\,\mu$m (R $= 4\,\mu$m). **(C)** Dependence of the discrepancy measure z on the effective coupling distance between presynaptic Ca^{2+} channels and sensors of exocytosis. Dashed lines correspond to $i_{\text{Ca}} = 0.3$ pA, solid lines correspond to $i_{\text{Ca}} = 7$ pA. The black dash-dotted line corresponds to the average of the experimental s.e.m.$[\Delta C_m]/\langle \Delta C_m \rangle$ over different Ca^{2+} buffering conditions (R $= 2\,\mu$m). **(D)** Ratios of $[\text{Ca}^{2+}]$ in the presence, denoted by $[\text{Ca}^{2+}]_{+\text{buff.}}$, and the absence, denoted by $[\text{Ca}^{2+}]_{-\text{buff.}}$, of particular buffers as functions of the distance from the 1 nm radius hemispherical source. Color lines are the best fits of $[\text{Ca}^{2+}]_{+\text{buff.}}/[\text{Ca}^{2+}]_{-\text{buff.}}$ corresponding to 0.5 mM and 1 mM BAPTA with $[\text{Ca}^{2+}]_{+\text{buff.}}/[\text{Ca}^{2+}]_{-\text{buff.}}$ corresponding to either calretinin (magenta), calbindin-D28k (blue) or parvalbumin-α (green).

16

8 Defining and Evaluating the Effective Coupling Distance R_c (Including Supplementary Figure 12)

Several versions of the model of a single effective vesicular release site driven by a single effective Ca^{2+} channel have been applied to evaluate the proximity between presynaptic Ca^{2+} channels and Ca^{2+} sensors of exocytosis based on the differential effect of mobile exogenous Ca^{2+} buffers with different Ca^{2+} binding kinetics and concentrations on exocytosis (see, for example, (14 – 17)). Intuitively, the coupling distance, which we denote by R_c, estimated in the framework of that model reflects the proximity between the Ca^{2+} channels and the vesicular release sites within the active zone. However, how R_c is quantitatively related to the parameters which define the spatial arrangement of presynaptic Ca^{2+} channels and vesicular release sites, as well as the kinetic parameters which define the Ca^{2+} dynamics, has not been analyzed before.

In this section we provide a mathematical analysis for understanding the physical meaning of R_c. This analysis unravels that R_c, in general, is a complicated, nonlinear average of the physical distances between the presynaptic Ca^{2+} channels and Ca^{2+} sensors of exocytosis. The main advantage of the single Ca^{2+} source model compared to spatially resolved models is that it produces a single output, R_c, which embodies the essence of all possible active zone topographies which are compatible with the experimental data. However, as we explain later in this section, the model also has a disadvantage that the exact value of R_c depends not only on the structural but also on the kinetic parameters of the system, such as Ca^{2+} cooperativity of exocytosis or Ca^{2+} binding kinetics of intracellular Ca^{2+} buffers. Thus, to avoid misinterpretations of R_c, care has to be taken when designing the experiments.

In this section, we also provide results of spatially resolved models of IHC presynaptic active zones introduced previously (see (2)). We show that active zone topographies suggested as corresponding to the "Ca^{2+} nanodomain coupling" regime in (2) are compatible with the R_c estimate determined in our present work.

8.1 Active zones with 1 vesicular release site and N Ca^{2+} channels, no Ca^{2+} buffers

First of all, let us consider a presynaptic active zone which contains N Ca^{2+} channels and one vesicular release site (see **Fig. S12A**). We assume that no Ca^{2+} buffers are present in the cytoplasm and that Ca^{2+} diffuses freely above the reflective cellular membrane. In this case, a particular channel i results in an increment of $[Ca^{2+}]$, which, averaged over time in steady state at fixed membrane potential, is inversely proportional to the distance from the mouth of that channel[5] (3):

$$\delta\langle[Ca^{2+}]\rangle_i = \frac{i_{Ca} \cdot P_o}{4 \cdot \pi \cdot F \cdot D \cdot R_i}, \qquad [1]$$

---

[5]For the sake of mathematical tractability, here and further on in sections 8.1 – 8.5, we treat Ca^{2+} channels as point sources and assume open boundary conditions above the plane of the plasma membrane (see (3)), unless stated otherwise. It follows from the results of section 7.6 that such an approximation would have negligible effect on the estimates of the effective coupling distance R_c.

17

where i_{Ca} is single Ca^{2+} channel current, R_i — distance from the mouth of i-th channel to the point of interest, F — Faraday constant, D — diffusion coefficient of Ca^{2+}, P_o — open probability of the channels in steady state at a given membrane potential. Let us now consider a response of such a model synapse to a depolarizing pulse of certain length. We assume that exocytosis at the synapse is fully determined by the time-averaged Ca^{2+} concentration at the vesicular release site[6], $\langle[Ca^{2+}]\rangle = \sum_{i=1}^{N} \delta\langle[Ca^{2+}]\rangle_i$ [7], and is not affected by momentary Ca^{2+} concentration fluctuations due to the channel opening and closing (the validity of this assumption is considered in section 8.5). We also assume that functional relation between $\langle[Ca^{2+}]\rangle$ and the amount of vesicles released in a chosen time period T, which we denote by $\Delta_{rel.}$, is bijective: $\Delta_{rel.} = f(\langle[Ca^{2+}]\rangle)$. Given this, we can apply a single Ca^{2+} source model to determine the effective coupling distance R_c from a measured $\Delta_{rel.}$: R_c is the distance from a single Ca^{2+} source, with total Ca^{2+} influx $I_{Ca} = N \cdot i_{Ca}$, to the point of interest at which Ca^{2+} concentration is equal to $\langle[Ca^{2+}]\rangle = f^{-1}(\Delta_{rel.})$. Taking into account equation [1], we can express R_c in the following way:

$$R_c = \frac{I_{Ca} \cdot P_o}{4 \cdot \pi \cdot F \cdot D \cdot \langle[Ca^{2+}]\rangle} = \frac{\sum_{i=1}^{N} (i_{Ca} \cdot P_o)/(4 \cdot \pi \cdot F \cdot D)}{\langle[Ca^{2+}]\rangle} = \frac{\sum_{i=1}^{N} R_i \cdot \delta\langle[Ca^{2+}]\rangle_i}{\langle[Ca^{2+}]\rangle} =$$

$$= \sum_{i=1}^{N} R_i \cdot \left(\frac{\delta\langle[Ca^{2+}]\rangle_i}{\sum_{j=1}^{N} \delta\langle[Ca^{2+}]\rangle_j} \right) \equiv \langle R \rangle_{Ca}^{\mathcal{L}} \qquad [2]$$

Thus, R_c is a weighted average of distances from all the channels to the Ca^{2+} sensor of exocytosis, which we denote by $\langle R \rangle_{Ca}^{\mathcal{L}}$. Here, superscript $\mathcal{L}$ stands for "linear" and subscript Ca indicates that the averaging weights depend on how $\delta\langle[Ca^{2+}]\rangle_i$ depends on R_i [8]. The weight for each channel is the relative contribution of that channel to $\langle[Ca^{2+}]\rangle$ at the vesicular release site. The higher is the contribution of a channel to $\langle[Ca^{2+}]\rangle$ and, thus, exocytosis, the closer is $\langle R \rangle_{Ca}^{\mathcal{L}}$ to the distance from that channel to the sensor. Note that the choice $I_{Ca} = N \cdot i_{Ca}$ is derived from the requirement that $R_c = R_i$ when $R_i = R_j$ for any i and j, i.e., when all the channels are equidistant to the Ca^{2+} sensor.

---

[6]Here and further on, we assume that the exocytosis rate depends on $[Ca^{2+}]$ at a particular point associated with the vesicular release site which we will call "Ca^{2+} sensor". "Ca^{2+} concentration at a vesicular release site" and "Ca^{2+} concentration at a Ca^{2+} sensor of exocytosis" are used as synonyms in sections 8.1 – 8.5.

[7]Here and further on, we assume that the contribution of the background $[Ca^{2+}]$, i.e., $[Ca^{2+}]$ in the absence of stimulus, is negligible.

[8]It is shown in section 8.4 that, in general, the averaging weights depend not only on the quantitative expression of $\delta\langle[Ca^{2+}]\rangle_i$ vs. R_i but also on the properties of release rate dependence on $\langle[Ca^{2+}]\rangle$. Moreover, as it is shown in 8.2, the averaging is nonlinear if Ca^{2+} buffers are present in the presynaptic solution.
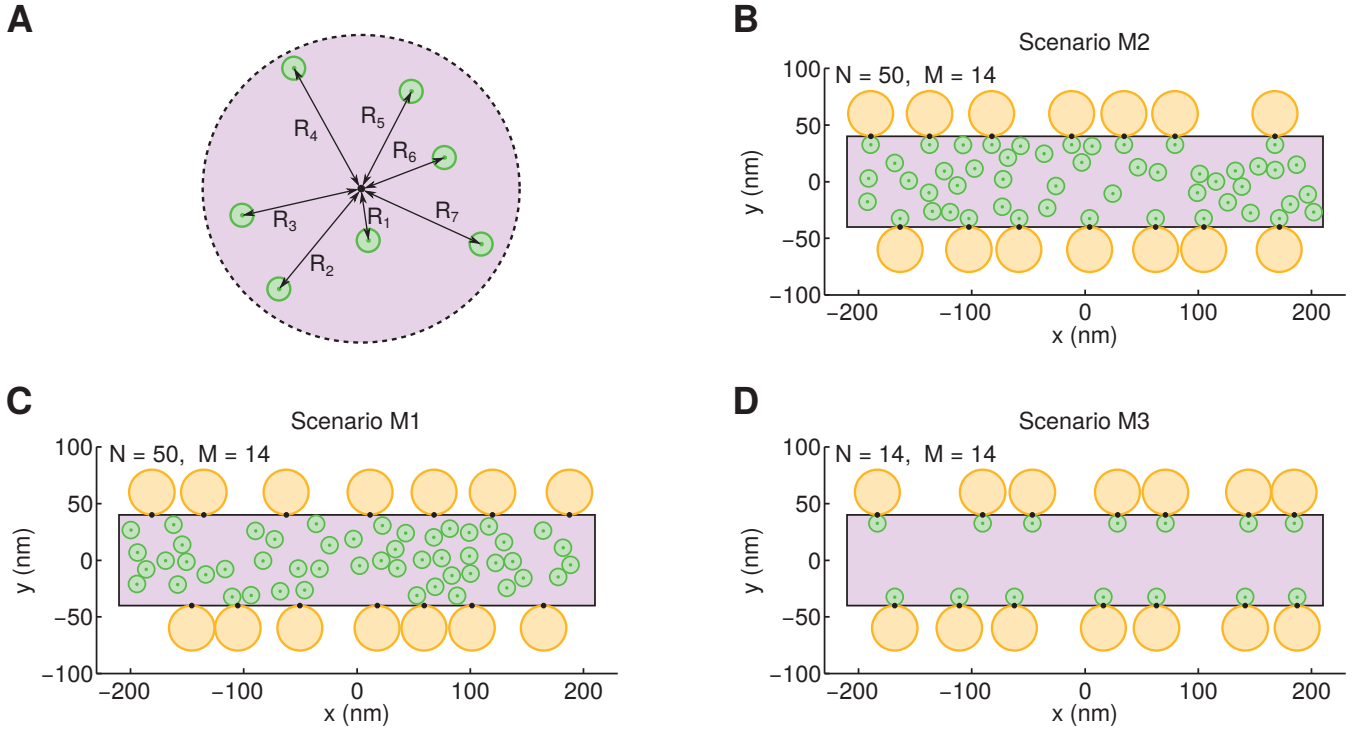
Figure S12: Examples of the active zone topographies considered in section 8. Orange discs – RRP vesicles, green discs – Ca^{2+} channels, black spots – Ca^{2+} sensors of exocytosis, violet area – presynaptic density.

8.2 Active zones with 1 vesicular release site and N Ca^{2+} channels, one set of Ca^{2+} buffers

Let us next consider a situation equivalent to that introduced in the previous section, except that we now assume the presence of one presynaptic mobile Ca^{2+} buffer. As it was shown in section 7.4, the linearized approximation of Ca^{2+} dynamics works well for the synapse considered in this work[9]. Then, the time-averaged stationary spatial Ca^{2+} concentration profile resulting from a single Ca^{2+} channel in the presence of a Ca^{2+} buffer with a single binding site reads as (3):

$$\delta\langle[\text{Ca}^{2+}]\rangle_i = \frac{i_{Ca} \cdot P_o}{4 \cdot \pi \cdot F \cdot (\kappa \cdot D_B + D) \cdot R_i} \cdot \left(1 + \frac{\kappa \cdot D_B}{D} \cdot e^{-R_i/\lambda}\right) = \frac{i_{Ca} \cdot P_o}{R_i} \cdot (A + B \cdot e^{-R_i/\lambda}), \quad [3]$$

where D_B is diffusion coefficient of the buffer molecules, κ and λ are parameters dependent on the resting Ca^{2+} concentration, Ca^{2+} binding and unbinding rates of the buffer as well as D and D_B (see (3) for quantitative definition of κ and λ). Let us now, as in the previous section, assume that we estimate $\langle[\text{Ca}^{2+}]\rangle$ at the vesicular release site based on an experimentally measured amount of exocytosis: $\langle[\text{Ca}^{2+}]\rangle = f^{-1}(\Delta_{rel.})$. Then, we can apply the single Ca^{2+} source model and estimate the effective coupling distance R_c by solving the following equation:

$$\langle[\text{Ca}^{2+}]\rangle = \frac{I_{Ca} \cdot P_o}{R_c} \cdot (A + B \cdot e^{-R_c/\lambda}) \quad \rightarrow \quad R_c. \quad [4]$$

---

[9]This assumption is applied to all the situations considered in sections 8.2-8.5 whenever the presence of Ca^{2+} buffers is assumed.

If we denote $\delta\langle[\mathrm{Ca}^{2+}]\rangle_i = g(R_i)$, equation [4] can be written in the following way:

$$R_c = g^{-1}\left(\frac{\langle[\mathrm{Ca}^{2+}]\rangle}{N}\right) = g^{-1}\left(\frac{1}{N}\sum_{i=1}^{N}g(R_i)\right) \equiv \langle R\rangle_{Ca}^{\mathcal{N}}, \qquad [5]$$

Thus, in this case, R_c can be interpreted as a nonlinear average, which we denote by $\langle R\rangle_{Ca}^{\mathcal{N}}$, of R_is implicitly weighted by contributions of the corresponding channels to $\langle[\mathrm{Ca}^{2+}]\rangle$. Here, superscript $\mathcal{N}$ stands for "nonlinear". The higher the contribution of a channel to $\langle[\mathrm{Ca}^{2+}]\rangle$ and, thus, exocytosis, the closer $\langle R\rangle_{Ca}^{\mathcal{N}}$ is to the distance from that channel to the Ca^{2+} sensor of exocytosis. Equation [5] is valid for any arbitrary well defined dependence of $\delta\langle[\mathrm{Ca}^{2+}]\rangle_i$ on R_i, for example, the one in the presence of multiple mobile Ca^{2+} buffers in the presynaptic solution.

It follows from equation [5] that $\langle R\rangle_{Ca}^{\mathcal{N}} = \langle R\rangle_{Ca}^{\mathcal{L}} = R_i$ if all the channels are equidistant to the Ca^{2+} sensor, i.e., $R_i = R_j$ for any i and j. If the channels are not equidistant, $\langle R\rangle_{Ca}^{\mathcal{N}} \neq \langle R\rangle_{Ca}^{\mathcal{L}}$. However, note that at sufficiently small distances, i.e., when $R_i \ll \lambda$, and at sufficiently large distances, i.e., when $R_i \gg \lambda$, $\delta\langle[\mathrm{Ca}^{2+}]\rangle_i$ is approximately inversely proportional to R_i even in the presence of Ca^{2+} buffers. This statement follows from equation [3], see also (3). Thus, if a fraction of the channels is sufficiently close to the Ca^{2+} sensor, while the remaining channels are sufficiently far away from the Ca^{2+} sensor, $\langle R\rangle_{Ca}^{\mathcal{N}} \approx \langle R\rangle_{Ca}^{\mathcal{L}}$.

To estimate how big the difference between $\langle R\rangle_{Ca}^{\mathcal{N}}$ and $\langle R\rangle_{Ca}^{\mathcal{L}}$ might be in Ca^{2+} buffering conditions used in this work, we considered a Ca^{2+} channel cluster consisting of 2 to 5 channels, which were distributed in a 2D area, like in **Fig. S12A**. Each of the channels was located from the Ca^{2+} sensor of exocytosis not closer than 1 nm and not further than 100 nm. 0.5 mM and 1 mM of either BAPTA or EGTA were considered as presynaptic Ca^{2+} buffers. To estimate the maximum and the minimum values of the difference $\langle R\rangle_{Ca}^{\mathcal{N}} - \langle R\rangle_{Ca}^{\mathcal{L}}$, we used the optimization based on a genetic algorithm (MATLAB function ga, $Generations=20\cdot N$, $StallGenLimit=15\cdot N$, $PopulationSize=N\cdot 50$, $EliteCount=N\cdot 5$, $CrossoverFraction=0.6$, $TolFun=10^{-12}$) followed by Nelder-Mead simplex method (MATLAB function $fminsearch$) repeated with 100 different initial conditions. In all these cases considered, the numerical optimization suggested that $\langle R\rangle_{Ca}^{\mathcal{N}} \geq \langle R\rangle_{Ca}^{\mathcal{L}}$ with the equality between the two present only when all the Ca^{2+} channels were equidistant to the sensor. $\max[\langle R\rangle_{Ca}^{\mathcal{N}} - \langle R\rangle_{Ca}^{\mathcal{L}}]$ was larger for buffers with smaller parameter λ, and for larger N, as summarized in **Table S1**.

	$\max[\langle R\rangle_{Ca}^{\mathcal{N}} - \langle R\rangle_{Ca}^{\mathcal{L}}]$, nm			
	0.5 mM EGTA	1 mM EGTA	0.5 mM BAPTA	1 mM BAPTA
$N = 2$	3	4	9	9
$N = 3$	4	6	14	14
$N = 4$	5	7	17	17
$N = 5$	6	7	19	19

Table S1

8.3 Active zones with 1 vesicular release site and N Ca^{2+} channels, two sets of Ca^{2+} buffers

As it is formulated in Methods, the single Ca^{2+} source model was designed to estimate the effective coupling distance R_c from experimental data in such a way that knowledge of the absolute values of $\langle[Ca^{2+}]\rangle$ at the vesicular release sites is not required[10]. Indeed, if we measure amounts of released vesicles in two different Ca^{2+} buffering conditions, then the ratio of these two estimates, $\Delta_{rel.,1}/\Delta_{rel.,2} = f(\langle[Ca^{2+}]_1\rangle)/f(\langle[Ca^{2+}]_2\rangle) = (\langle[Ca^{2+}]_1\rangle/\langle[Ca^{2+}]_2\rangle)^m$ can be used to extract the R_c:

$$\frac{\Delta_{rel.,1}}{\Delta_{rel.,2}} = \left(\frac{A_1 + B_1 \cdot e^{-R_c/\lambda_1}}{A_2 + B_2 \cdot e^{-R_c/\lambda_2}} \right)^m \quad \rightarrow \quad R_c \qquad [6]$$

Here, A's and B's depend only on the physical parameters of the buffer molecules, their concentrations, diffusion coefficient of Ca^{2+} and the resting $[Ca^{2+}]$ at the presynaptic site. m is the apparent cooperativity of exocytosis[11]. If we denote $\delta\langle[Ca^{2+}]_1\rangle_i = g_1(R_i)$, $\delta\langle[Ca^{2+}]_2\rangle_i = g_2(R_i)$, and $g_1(x)/g_2(x) = g_{12}(x)$, equation [6] can be rewritten in the following way:

$$R_c = g^{-1}\left(\frac{\langle[Ca^{2+}]_1\rangle}{\langle[Ca^{2+}]_2\rangle} \right) = g_{12}^{-1}\left(\frac{\sum_{i=1}^N g_1(R_i)}{\sum_{i=1}^N g_2(R_i)} \right) \equiv \langle R\rangle_{Ca,12}^{\mathcal{N}*}, \qquad [7]$$

Here, subscript 12 stands for the two buffering conditions "1" and "2" used to estimate $\langle R\rangle_{Ca,12}^{\mathcal{N}*}$. The superscript $*$ is used to emphasize that the effective coupling distance is calculated by estimating exocytosis in two different presynaptic Ca^{2+} buffering conditions "1" and "2". Like $\langle R\rangle_{Ca}^{\mathcal{N}}$, $\langle R\rangle_{Ca,12}^{\mathcal{N}*}$ can be interpreted as a nonlinear average, of R_is implicitly weighted by the contributions of the corresponding channels to $\langle[Ca^{2+}]\rangle$. However, in general, $\langle R\rangle_{Ca,12}^{\mathcal{N}*} \neq \langle R\rangle_{Ca,1}^{\mathcal{N}}$ and $\langle R\rangle_{Ca,12}^{\mathcal{N}*} \neq \langle R\rangle_{Ca,2}^{\mathcal{N}}$, unless all the Ca^{2+} channels are equidistant to the Ca^{2+} sensor of exocytosis, in which case $\langle R\rangle_{Ca,12}^{\mathcal{N}*} = \langle R\rangle_{Ca,1}^{\mathcal{N}} = \langle R\rangle_{Ca,2}^{\mathcal{N}} = R_i$. Clearly, equation [7] is valid for any arbitrary well defined dependence of $\delta\langle[Ca^{2+}]\rangle_i$ on R_i, for example, the one in the presence of multiple mobile Ca^{2+} buffers in the presynaptic solution.

That we do not need to know the absolute values of $\langle[Ca^{2+}]\rangle$ at the Ca^{2+} sensor of exocytosis or Ca^{2+} currents that give rise to $\langle[Ca^{2+}]\rangle$ in order to determine R_c as defined by equation [7] is a very important advantage of the mentioned approach over that considered in section 8.2. Indeed, $\langle[Ca^{2+}]\rangle$ at Ca^{2+} sensors of exocytosis is not a measurable quantity with currently available experimental techniques. On the other hand, this approach has one disadvantage, which always has to be kept in mind when interpreting estimates of R_c based on the experimental data. The disadvantage is that it is necessary to measure the release in at least two different Ca^{2+} buffering conditions, only one of which can be the natural one. Thus, an estimate of R_c achieved by using this approach depends not only on the intrinsic properties of the system being studied, but also on how we choose to study the system. It follows from equation [3] that, when the buffering length constant λ is decreased (by increasing concentration of the buffer, for example), the contribution of a particular channel to $\langle[Ca^{2+}]\rangle$ at a Ca^{2+} sensor of exocytosis is decreased the more the further that channel is away from the sensor. Thus, if mobile Ca^{2+} buffers used for estimating R_c are much stronger than the endogenous buffers of the synapse, the coupling distance may be

---

[10]Assuming the linearity between i_{Ca} and $\langle[Ca^{2+}]\rangle$ at the vesicular release sites.

[11]Here and further on, we assume that the apparent Ca^{2+} cooperativity is the same in both Ca^{2+} buffering conditions used for determining R_c.

considerably underestimated. Vice versa, if mobile Ca^{2+} buffers used for estimating R_c are much weaker than the endogenous buffers of the synapse, the coupling distance may be overestimated. Nevertheless, as it is shown next, $\langle R \rangle_{Ca,12}^{\mathcal{N}*}$ is closely related to quantities uniquely determined by the configuration of the natural system, for example, $\langle R \rangle_{Ca,1}^{\mathcal{L}}$ or $\langle R \rangle_{Ca,2}^{\mathcal{L}}$, and carries valuable information about the system if the experiment is designed appropriately. Noteworthy, if spatially resolved simulations are performed to check the hypothesis of particular scenarios of the active zone organization, the experimental estimate of R_c can be directly compared to its modeled counterpart independently of the buffering conditions[12].

To better understand the physical meaning of $\langle R \rangle_{Ca,12}^{\mathcal{N}*}$, we compared it with linear weighted average distances $\langle R \rangle_{Ca,1}^{\mathcal{L}}$ and $\langle R \rangle_{Ca,2}^{\mathcal{L}}$, estimated separately in the two Ca^{2+} buffering conditions used for estimating $\langle R \rangle_{Ca,12}^{\mathcal{N}*}$ [13]. To this end, we first considered the previously introduced active zone model consisting of one vesicular release site and two to five Ca^{2+} channels (see section 8.2). Pairs constructed from four Ca^{2+} buffers introduced above were considered, namely: 1 mM BAPTA & 0.5 mM BAPTA, 1 mM BAPTA & 1 mM EGTA, 1 mM BAPTA & 0.5 mM EGTA, 0.5 mM BAPTA & 1 mM EGTA, 1 mM EGTA & 0.5 mM EGTA and 0.5 mM BAPTA & 0.5 mM EGTA. Numerical global optimization (performed in the same way as introduced in section 8.2) resulted in $\langle R \rangle_{Ca,2}^{\mathcal{L}} > \langle R \rangle_{Ca,12}^{\mathcal{N}*} > \langle R \rangle_{Ca,1}^{\mathcal{L}}$ for buffers "1" and "2" with $\lambda_2 > \lambda_1$.

Next, we got estimates of $\langle R \rangle_{Ca,1}^{\mathcal{L}}$, $\langle R \rangle_{Ca,2}^{\mathcal{L}}$, and $\langle R \rangle_{Ca,12}^{\mathcal{N}*}$ for examples of physiologically realistic active zone topographies. To this end, we studied three IHC active zone topography scenarios – M1, M2, and M3 – considered in (2), see **Fig**. **S12B**-**D**. In those three scenarios, 14 readily releasable pool vesicles (orange disks, $R = 20$ nm) were randomly distributed at the longer sides of the presynaptic density (violet rectangle). All the Ca^{2+} sensors of exocytosis (black dots) were located at the level of the plasma membrane, at the longer sides of the presynaptic density. In scenario M1, 50 Ca^{2+} channels (green disks, $R = 7.5$ nm) were distributed randomly within the presynaptic density. In scenario M2, 36 out of 50 Ca^{2+} channels were distributed randomly within the presynaptic density, while the remaining 14 Ca^{2+} channels were placed in contact with the Ca^{2+} sensors of exocytosis. In scenario M3, there were only 14 Ca^{2+} channels in contact with the Ca^{2+} sensors. We considered 100 active zone realizations for each scenario. Four pairs of mobile Ca^{2+} buffer sets, the same as those used in our experiments, were assumed: 1 mM BAPTA + 2mM ATP & 0.5 mM BAPTA + 2mM ATP, 1 mM BAPTA + 2 mM ATP & 1 mM EGTA + 2 mM ATP, 1 mM BAPTA + 2mM ATP & 0.5 mM EGTA + 2 mM ATP, and 1 mM BAPTA + 2 mM ATP & 2 mM ATP. Mouth of each Ca^{2+} channel was treated as a hemispherical source with 1 nm radius and $i_{Ca} = 0.3$ pA. $\langle R \rangle_{Ca,1}^{\mathcal{L}}$, $\langle R \rangle_{Ca,2}^{\mathcal{L}}$, and $\langle R \rangle_{Ca,12}^{\mathcal{N}*}$ were estimated for each active zone scenario as averages over separate vesicular release sites within a particular realization of the active zone and over 100 realizations of that active zone scenario. The results are summarized in **Table S2**.

We found that, as in the case of the simplified active zone model considered before, inequality $\langle R \rangle_{Ca,2}^{\mathcal{L}} > \langle R \rangle_{Ca,12}^{\mathcal{N}*} > \langle R \rangle_{Ca,1}^{\mathcal{L}}$ holds for active zone scenarios M1, M2, and M3. $\langle R \rangle_{Ca,12}^{\mathcal{N}*}$ was shifted more towards $\langle R \rangle_{Ca,1}^{\mathcal{L}}$ than to $\langle R \rangle_{Ca,2}^{\mathcal{L}}$. As expected, values of $\langle R \rangle_{Ca,1}^{\mathcal{L}}$, $\langle R \rangle_{Ca,2}^{\mathcal{L}}$, and $\langle R \rangle_{Ca,12}^{\mathcal{N}*}$ were the

---

[12]Of course, in this case, the exact value of R_c depends on the properties of the Ca^{2+} buffers used. However, now we need to use only one set of Ca^{2+} buffers. This set of buffers may be chosen, at least in principle, to be that which is present in a real synapse.

[13]The main reason why we chose $\langle R \rangle_{Ca,1}^{\mathcal{L}}$ and $\langle R \rangle_{Ca,2}^{\mathcal{L}}$, not $\langle R \rangle_{Ca,1}^{\mathcal{N}}$ and $\langle R \rangle_{Ca,2}^{\mathcal{N}}$, to compare to $\langle R \rangle_{Ca,12}^{\mathcal{N}*}$ is that $\langle R \rangle_{Ca}^{\mathcal{L}}$ have a clearer physical meaning than $\langle R \rangle_{Ca}^{\mathcal{N}}$ (compare equations [2] and [5]).

			"1" 1 mM BAPTA "2" 0.5 mM BAPTA (+2 mM ATP)	"1" 1 mM BAPTA "2" 0.5 mM EGTA (+2 mM ATP)	"1" 1 mM BAPTA "2" 1 mM EGTA (+2 mM ATP)	"1" 1 mM BAPTA "2" - (+2 mM ATP)
M1	$\langle R\rangle_{Ca,1}^{\mathcal{L}}$	(nm)	35	35	35	35
	$\langle R\rangle_{Ca,12}^{\mathcal{N}*}$		36	44	43	45
	$\langle R\rangle_{Ca,2}^{\mathcal{L}}$		40	65	62	70
M2	$\langle R\rangle_{Ca,1}^{\mathcal{L}}$	(nm)	19	19	19	19
	$\langle R\rangle_{Ca,12}^{\mathcal{N}*}$		20	28	27	29
	$\langle R\rangle_{Ca,2}^{\mathcal{L}}$		24	47	44	52
M3	$\langle R\rangle_{Ca,1}^{\mathcal{L}}$	(nm)	10	10	10	10
	$\langle R\rangle_{Ca,12}^{\mathcal{N}*}$		11	15	15	16
	$\langle R\rangle_{Ca,2}^{\mathcal{L}}$		12	26	24	29

Table S2

smallest for scenario M3 (the most tight coupling), and the largest for scenario M1 (the least tight coupling) at any buffering conditions considered. The largest difference between $\langle R\rangle_{Ca,2}^{\mathcal{L}}$ and $\langle R\rangle_{Ca,1}^{\mathcal{L}}$, which reflects the sensitivity of R_c estimate to the Ca^{2+} buffering conditions, was found for scenario M1 and the smallest – for scenario M3. This is partially explained by the fact that a tighter coupling with fewer channels contributing Ca^{2+} to particular vesicular release sites results in a smaller variability of the distances between the channels and the vesicular release site about the average one. Another reason is that the considered mobile Ca^{2+} buffers have a relatively small effect on $\delta\langle[Ca^{2+}]\rangle_i$ when the coupling is so tight as in scenario M3, as mentioned in section 8.2. The estimates of $\langle R\rangle_{Ca,1}^{\mathcal{L}}$, $\langle R\rangle_{Ca,2}^{\mathcal{L}}$, and $\langle R\rangle_{Ca,12}^{\mathcal{N}*}$ were smaller with stronger Ca^{2+} buffering conditions. For example, in the case of scenario M1, $\langle R\rangle_{Ca,12}^{\mathcal{N}*}$ was equal to 36 nm for 1 mM BAPTA + 2 mM ATP & 0.5 mM BAPTA + 2 mM ATP, compared to 45 nm for 1 mM BAPTA + 2mM ATP & 2 mM ATP. This trend is explained by the fact that the relative contributions of more distant Ca^{2+} channels are reduced when the strength of the Ca^{2+} buffers is increased.

In conclusion, the results discussed in this section suggest that, at least for the Ca^{2+} buffering conditions considered in this work, $\langle R\rangle_{Ca,12}^{\mathcal{N}*}$ can be treated as an upper or lower bound for $\langle R\rangle_{Ca}^{\mathcal{L}}$ estimated in the natural Ca^{2+} buffering conditions. $\langle R\rangle_{Ca,12}^{\mathcal{N}*}$ is the upper bound for $\langle R\rangle_{Ca}^{\mathcal{L}}$ when buffer "2" is weaker, i.e., with higher *lambda*, than the natural Ca^{2+} buffer in the synapse while buffer "1" is not stronger than the endogenous buffer. $\langle R\rangle_{Ca,12}^{\mathcal{N}*}$ is the lower bound for $\langle R\rangle_{Ca}^{\mathcal{L}}$ when buffer "2" is not stronger than the endogenous Ca^{2+} buffer in the synapse while buffer "1" is stronger, i.e., with lower *lambda*, than the natural buffer.

8.4 Active zones with M vesicular release sites and N Ca^{2+} channels

Real presynaptic active zones contain considerably more than one vesicular release site. If the dependence of vesicle release rate on $[Ca^{2+}]$ is non-linear, the interpretation of the effective coupling distance R_c for an active zone with $M > 1$ site is more complicated compared to the situations with $M = 1$ considered

so far[14]. To see this, let us consider an active zone with $M > 1$ vesicular release sites driven by N Ca^{2+} channels. As before, we assume that the contribution to the time-averaged Ca^{2+} concentration at a particular vesicular release site j by a particular channel i is a bijective function of the distance between the channel and the corresponding Ca^{2+} sensor of exocytosis: $\delta\langle[Ca^{2+}]\rangle_{j,i} = g(R_{j,i})$. We also assume that, for each vesicular release site, the amount of vesicles released in particular time window T depends only on time-averaged Ca^{2+} concentration at that vesicular release site: $\Delta_{rel.,j} = f(\langle[Ca^{2+}]\rangle_j) = f\left(\sum_{i=1}^{N} \delta\langle[Ca^{2+}]\rangle_{j,i}\right)$. Then, R_c estimated by recording the amount of release at the active zone, $\Delta_{rel.,\Sigma} = \sum_{j=1}^{M} \Delta_{rel.,j}$, in the presence of a particular set of Ca^{2+} buffers can be expressed in the following way:

$$R_c = g^{-1}\left(\frac{1}{N} f^{-1}\left(\frac{1}{M} \sum_{j=1}^{M} f\left(\sum_{i=1}^{N} g(R_{j,i})\right)\right)\right). \qquad [8]$$

Equation [8] is a generalization of equation [5] for active zones with an arbitrary number of vesicular release sites. R_c defined by equation [8] can be interpreted as a nonlinear, implicitly weighted average of distances between a particular channel and a particular Ca^{2+} sensor of exocytosis over all possible channel-sensor pairs. Differently from the situation with a single vesicular release site, the nonlinear averaging of distances between one of the Ca^{2+} channels and one of the Ca^{2+} sensors of exocytosis now depends not only on how $\delta\langle[Ca^{2+}]\rangle_{j,i}$ depends on $R_{j,i}$ but also on how $\Delta_{rel.,j}$ depends on $\langle[Ca^{2+}]\rangle_j$. Qualitatively, the larger the relative contribution of a particular Ca^{2+} channel to $\langle[Ca^{2+}]\rangle_j$ at a particular vesicular release site is and the larger the relative contribution of that vesicular release site to the overall release at the active zone $\Delta_{rel.,\Sigma}$ is, the closer is R_c to the distance between that particular Ca^{2+} channel and Ca^{2+} sensor of exocytosis of that particular vesicular release site.

If all vesicular release sites are equivalent in the sense of how the Ca^{2+} channels are positioned in regards of them, i.e., if $R_{j,i} = R_{j',i} \equiv R_i$ for any j, j', and i, the effective coupling distance for the whole active zone is equal to the effective coupling distance for one of the vesicular release sites. Indeed, if that condition is met, equation [8] reduces to equation [5]. Equation [8] reduces to $R_c = R_{i,j}$ when $R_{i,j} = R_{i',j'}$ for arbitrary i, i', j, and j'. i.e., when all the Ca^{2+} channels are at the same distance from all the Ca^{2+} sensors. In this case, R_c is equal to the physical distance between any of those Ca^{2+} channels and any of those Ca^{2+} sensors of exocytosis at the active zone. If $\Delta_{rel.,j}$ depends on $\langle[Ca^{2+}]\rangle_j$ linearly, i.e., if $f(x) = a \cdot x + b$, the effective coupling distance R_c is equal to the effective coupling distance of the "average vesicular release site" within the active zone:

$$R_c = g^{-1}\left(\frac{1}{M} \sum_{j=1}^{M} \left(\frac{1}{N} \sum_{i=1}^{N} g(R_{j,i})\right)\right). \qquad [9]$$

When dependence of $\Delta_{rel.,j}$ on $\langle[Ca^{2+}]\rangle_j$ follows a power law, i.e., when $f(x) = k \cdot x^m$, and no Ca^{2+} buffers are present in the presynaptic solution, i.e., when $\delta\langle[Ca^{2+}]\rangle_{j,i}$ is described by [1], [8] has the

---

[14]This is true independently of how many vesicles are actually released during the observation window.

following form:

$$R_c = g^{-1}\left(\frac{1}{N}\left(\frac{1}{M}\sum_{j=1}^{M}\left(\sum_{i=1}^{N}g(R_{j,i})\right)^m\right)^{1/m}\right) = \frac{M \cdot N \cdot i_{Ca} \cdot P_o/(4 \cdot \pi \cdot F \cdot D)}{M \cdot \left(\frac{1}{M}\sum_{j=1}^{M}\left(\sum_{i=1}^{N}g(R_{j,i})\right)^m\right)^{1/m}} =$$

$$= \frac{\sum_{j=1}^{M}\sum_{i=1}^{N}R_{j,i}\cdot g(R_{j,i})}{M \cdot \left(\frac{1}{M}\sum_{j=1}^{M}\left(\sum_{i=1}^{N}g(R_{j,i})\right)^m\right)^{1/m}} =$$

$$= \sum_{j=1}^{M}\sum_{i=1}^{N}R_{j,i}\cdot\left(\frac{\delta\langle[\mathrm{Ca}^{2+}]_{\mathrm{j,i}}\rangle}{M \cdot \left(\frac{1}{M}\sum_{j'=1}^{M}\left(\sum_{i'=1}^{N}\delta\langle[\mathrm{Ca}^{2+}]_{\mathrm{j',i'}}\rangle\right)^m\right)^{1/m}}\right) \equiv \langle\langle R\rangle\rangle_{Ca}^{\mathcal{L},m}. \qquad [10]$$

Here, $\left(\frac{1}{M}\sum_{j'=1}^{M}\left(\sum_{i'=1}^{N}\delta\langle[\mathrm{Ca}^{2+}]_{\mathrm{j',i'}}\rangle\right)^m\right)^{1/m}$ is the power m mean (Hölder mean) of $\langle[\mathrm{Ca}^{2+}]\rangle_{j'}$ over all M vesicular release sites at the active zone. Thus, the effective coupling distance R_c, in this case, is a weighted linear average of distances from all the Ca^{2+} channels to all the Ca^{2+} sensors in the active zone, which we denote by $\langle\langle R\rangle\rangle_{Ca}^{\mathcal{L},m}$. Here, the second angular brackets stand for averaging over vesicular release sites (in addition to the averaging over Ca^{2+} channels). The superscript m expresses the idea that the effective coupling distance depends on the apparent Ca^{2+} cooperativity of exocytosis. The weight for distance $R_{j,i}$ between channel i and vesicular release site j is equal to the ratio between the increment of Ca^{2+} concentration at the vesicular release site j contributed by the channel i and the power m mean of Ca^{2+} concentrations over all vesicular release sites at the active zone multiplied by the number of the vesicular release sites. It follows from the properties of the Hölder mean that $\left(\frac{1}{M}\sum_{j'=1}^{M}\left(\sum_{i'=1}^{N}\delta\langle[\mathrm{Ca}^{2+}]_{\mathrm{j',i'}}\rangle\right)^{m_2}\right)^{1/m_2} > \left(\frac{1}{M}\sum_{j'=1}^{M}\left(\sum_{i'=1}^{N}\delta\langle[\mathrm{Ca}^{2+}]_{\mathrm{j',i'}}\rangle\right)^{m_1}\right)^{1/m_1}$ for $m_2 > m_1$. Thus, the higher is Ca^{2+} cooperativity of exocytosis, the smaller is $\langle\langle R\rangle\rangle_{Ca}^{\mathcal{L},m}$.

When R_c is estimated by using the measurements of $\Delta_{rel.,\Sigma}$ in two different Ca^{2+} buffering conditions[15] and $f(x) = k \cdot x^m$, the equivalent of equation [8] reads as

$$R_c = g_{12}^{-1}\left(\left(\frac{\sum_{j=1}^{M}\left(\sum_{i=1}^{N}g_1(R_{j,i})\right)^m}{\sum_{j=1}^{M}\left(\sum_{i=1}^{N}g_2(R_{j,i})\right)^m}\right)^{1/m}\right) \equiv \langle\langle R\rangle\rangle_{Ca,12}^{\mathcal{N}*,m}, \qquad [11]$$

where $g_1(R_{j,i})$ and $g_2(R_{j,i})$ are dependencies of $\langle[\mathrm{Ca}^{2+}]\rangle_{j,i}$ on $R_{j,i}$ in Ca^{2+} buffering conditions "1" and "2" respectively, $g_{12}(x) = g_1(x)/g_2(x)$. Taking into account the results from section 8.3, it is tempting to hypothesize that $\langle\langle R\rangle\rangle_{Ca,12}^{\mathcal{N}*,m}$ could be an upper and a lower bound for $\langle\langle R\rangle\rangle_{Ca,1}^{\mathcal{L},m}$ and $\langle\langle R\rangle\rangle_{Ca,2}^{\mathcal{L},m}$, respectively, and could be rather well approximated by the average of the later two. We checked this idea with the realistic active zone topographies considered in section 8.3 and shown in **Fig. S12B-D**. The results of our simulations for $m = 1.7$, the experimentally predicted value of the apparent Ca^{2+} cooperativity of exocytosis (see **Fig. S6**), are summarized in **Table S3**. The results are strikingly similar to those for $\langle R\rangle_{Ca,1}^{\mathcal{L}}$, $\langle R\rangle_{Ca,12}^{\mathcal{N}*}$, and $\langle R\rangle_{Ca,2}^{\mathcal{L}}$, shown in **Table S2**[16]. Thus, all the conclusions and comments made at the end of section 8.3 in the context of an active zone with a single vesicular release site, are valid for R_c estimated for scenarios M1, M2, and M3 with all vesicular release sites within an active zone considered collectively.

---

[15]As it was done in our study.

[16]We also considered higher m values. As mentioned before, R_c estimates are smaller for larger m. However, for active zone topographies scenarios M2 and M3, $m = 5$ resulted in estimates of $\langle\langle R\rangle\rangle_{Ca,12}^{\mathcal{N}*,m}$ only < 1 nm smaller than those for

			"1" 1 mM BAPTA "2" 0.5 mM BAPTA (+2 mM ATP)	"1" 1 mM BAPTA "2" 0.5 mM EGTA (+2 mM ATP)	"1" 1 mM BAPTA "2" 1 mM EGTA (+2 mM ATP)	"1" 1 mM BAPTA "2" - (+2 mM ATP)
M1	$\langle\langle R\rangle\rangle_{Ca,1}^{\mathcal{L},m}$	(nm)	31	31	31	31
	$\langle\langle R\rangle\rangle_{Ca,12}^{\mathcal{N}*,m}$		32	41	40	42
	$\langle\langle R\rangle\rangle_{Ca,2}^{\mathcal{L},m}$		37	63	60	68
M2	$\langle\langle R\rangle\rangle_{Ca,1}^{\mathcal{L},m}$	(nm)	19	19	19	19
	$\langle\langle R\rangle\rangle_{Ca,12}^{\mathcal{N}*,m}$		20	28	28	30
	$\langle\langle R\rangle\rangle_{Ca,2}^{\mathcal{L},m}$		24	47	44	51
M3	$\langle\langle R\rangle\rangle_{Ca,1}^{\mathcal{L},m}$	(nm)	10	10	10	10
	$\langle\langle R\rangle\rangle_{Ca,12}^{\mathcal{N}*,m}$		11	15	15	16
	$\langle\langle R\rangle\rangle_{Ca,2}^{\mathcal{L},m}$		12	26	24	29

Table S3

Finally, we have to note that we used estimates of capacitance increments in four different pairs of Ca^{2+} buffering conditions collectively to estimate the R_c (see Methods). This was done with the purpose to reduce the influence of measurement noise in the experimental data. Thus, in order to interpret the experimental estimate of R_c in the context of spatially resolved active zone models, we have to estimate the same quantity for those modeled active zones. The corresponding model estimates of R_c calculated in the mentioned way were 41 nm, 28 nm, and 15 nm for scenarios M1, M2, and M3, respectively. Thus, our experimental estimate $R_c = 17$ nm with $5 - 95$ percentile range of $8 - 30$ nm (see Results) for the single Ca^{2+} source model is compatible with the active zone topography scenarios M2 and M3 but not scenario M1.

8.5 Influence of the Ca^{2+} channel opening-closing dynamics on R_c estimate

All considerations related to R_c in sections 8.1-8.4 were based on the assumption that exocytosis rate at any vesicular release site is a well defined function of the time-averaged stationary Ca^{2+} concentration at that vesicular release site. In our experiments, cumulative release was measured 20 ms after the stimulus onset. 20 ms is much longer than the characteristic equilibration time of the channel opening, which is 0.5 ms at the membrane potential corresponding to the peak Ca^{2+} current in IHCs (18). Thus, the assumption of stationarity is justified. However, "averaging out" the fluctuations of Ca^{2+} concentration due to opening and closing of the presynaptic Ca^{2+} channels may still substantially influence the results, if channel gating is not sufficiently fast[17]. To check this averaging assumption we performed additional simulations where the build-up and decay of $[Ca^{2+}]$ due to the channel gating was modeled explicitly as it was done in (2). We assumed a three state Markov model of the channel gating: $C_1 \underset{1 \cdot k_{-1}}{\overset{2 \cdot k_{+1}}{\rightleftharpoons}} C_2 \underset{2 \cdot k_{-1}}{\overset{1 \cdot k_{+1}}{\rightleftharpoons}} O$, $k_1 = 1.78$ ms^{-1}, $k_{-1} = 1.37$ ms^{-1}. Vesicle fusion followed the kinetic model proposed by (19). All the

---

$m = 1.7$. For scenario M1, the differences were not larger than 4 nm, which is still small compared to the absolute values of $\langle\langle R\rangle\rangle_{Ca,12}^{\mathcal{N}*,m}$. Thus, at least for the considered active zone topographies, m does not affect value of R_c considerably.

[17]By speed of channel gating we mean the closing and opening rates of the channel.

kinetic parameters of vesicle fusion were set to the original values except that k_{on} was reduced four times in order to reproduce reasonable m and ΔC_m values. Vesicle replenishment was treated as a single step process with a fixed rate $k_{rep} = 0.13\text{ms}^{-1}$. Other relevant details of the simulation procedure are reported in (2).

Using the aforementioned model to calculate $\Delta_{rel.,\Sigma}$ and its dependence on $\langle [\text{Ca}^{2+}] \rangle$, we estimated the coupling distance R_c in the same way which was discussed in the last paragraph of section 8.4. The corresponding values of R_c for scenarios M1, M2, and M3 were 37 nm, 27 nm, and 14 nm, respectively. This is in a very good agreement with the estimates of R_c that were achieved by ignoring the fluctuations of $[\text{Ca}^{2+}]$ due to the $[\text{Ca}^{2+}]$ channels closing and opening. This result lets us conclude that, for active zone topographies and the kinetic parameters considered in this work, the channel gating noise does not considerably affect the estimation of R_c.

References

1. P. Heil, H. Neubauer, D.R.F. Irvine, and M. Brown. **Spontaneous activity of auditory-nerve fibers: insights into stochastic processes at ribbon synapses.** *J. Neurosci.* 2007, **27**: 8457 – 8474.

2. A.B. Wong, M.A. Rutherford, M. Gabrielaitis, T. Pangršič, F. Göttfert, T. Frank, S. Michanski, S. Hell, F. Wolf, C. Wichmann, and T. Moser. **Developmental refinement of hair cell synapses tightens the coupling of Ca^{2+} influx to exocytosis.** *EMBO J.* 2014, **33**: 247 – 264.

3. M. Naraghi and E. Neher. **Linearized buffered Ca^{2+} diffusion in microdomains and its implications for calculation of [Ca^{2+}] at the mouth of a calcium channel.** *J. Neurosci.* 1997, **17**: 6961 – 6973.

4. U.V. Nägerl, D. Novo, I. Mody, and J.L. Vergara. **Binding kinetics of calbindin-D28k determined by flash photolysis of caged Ca^{2+}.** *Biophys. J.* 2000, **79**: 3009 – 3018.

5. J.H. Bollmann and B. Sakmann. **Control of synaptic strength and timing by the release-site Ca^{2+} signal.** *Nat. Neurosci.* 2005, **8**: 426 – 434.

6. S.H. Lee, B. Schwaller, and E. Neher. **Kinetics of Ca^{2+} binding to parvalbumin in bovine chromaffin cells: implications for [Ca^{2+}] transients of neuronal dendrites.** *J Physiol.* 2000, **525**: 419 – 432.

7. G.C. Faas, S. Raghavachari, J.E. Lisman, and I. Mody. **Calmodulin as a direct detector of Ca^{2+} signals**. *Nat. Neurosci.* 2011, **14**: 301 – 304.

8. G.C. Faas, B. Schwaller, J.L. Vergara, and I. Mody. **Resolving the fast kinetics of cooperative binding: Ca^{2+} buffering by calretinin**. *Plos Biol.* 2007, **5**: e311.

9. H. Schmidt, E.B. Brown, B. Schwaller, and J. Eilers. **Diffusional mobility of parvalbumin in spiny dendrites of cerebellar Purkinje beurons quantified by fluorescence recovery after photobleaching.** *Biophys. J.* 2003, **84**: 2599 – 2608.

10. H. Schmidt, B. Schwaller, and J. Eilers. **Calbindin D28k targets myo-inositol monophosphatase in spines and dendrites of cerebellar Purkinje neurons** *PNAS* 2005, **102**: 5850 – 5855.

11. D. Beutner, T. Moser. **The presynaptic function of mouse cochlear inner hair cells during development of hearing.** *J. Neurosci.* 2001, **21**: 4593 – 4599.

12. A.C. Meyer, T. Frank, D. Khimich, G. Hoch, D. Riedel, N.M. Chapochnikov, Y.M. Yarin, B. Harke, S.W. Hell, A. Egner, and T. Moser. **Tuning of synapse number, structure and function in the cochlea.** *Nat. Neurosci.* 2009, **12**: 444 – 453.

13. D. Lenzi, J.W. Runyeon, J. Crum, M.H. Ellisman, and W.M. Roberts. **Synaptic vesicle populations in saccular hair cells reconstructed by electron tomography.** *J. Neurosci.* 1999, **19**: 119 – 132.

14. E. Neher. **Usefulness and limitations of linear approximations to the understanding of Ca^{2+} signals.** *Cell Calcium* 1998, **24**: 345 – 357.

15. J.D. Goutman and E. Glowatzki. **Time course and calcium dependence of transmitter release at a single ribbon synapse.** *PNAS* 2007, **104**: 16341 – 16346.

16. I. Bucurenciu, A. Kulik, B. Schwaller, M. Frotscher, and P. Jonas. **Nanodomain coupling between Ca^{2+} channels and Ca^{2+} sensors promotes fast and efficient transmitter release at a cortical GABAergic synapse.** *Neuron* 2008, **57**: 536 – 545.

17. N.P. Vyleta and P. Jonas. **Loose coupling btween Ca^{2+} channels and release sensors at a plastic hippocampal synapse.** *Science* 2014, **343**: 665 – 670.

18. J. Neef, A. Gehrt, A.V. Bulankina, A.C. Meyer, D. Riedel, R.G. Gregg, N. Strenzke, and T. Moser. **The Ca^{2+} channel subunit β2 regulates Ca^{2+} channel abundance and function in inner hair cells and is required for hearing.** *J. Neurosci.* 2009, **29**: 10730 – 10740.

19. D. Beutner, T. Voets, E. Neher, and T. Moser. **Calcium dependence of exocytosis and endocytosis at the cochlear inner hair cell afferent synapse.** *Neuron* 2001, **29**: 681 – 690.